Repository Istituzionale dei Prodotti della Ricerca del Politecnico di Bari

Adhesion and friction in steady and unsteady viscoelastic contacts

This is a PhD Thesis

Original Citation:
Adhesion and friction in steady and unsteady viscoelastic contacts / Mandriota, Cosimo. - ELETTRONICO. - (2025). [10.60576/poliba/iris/mandriota-cosimo_phd2025]

Availability:
This version is available at http://hdl.handle.net/11589/281700 since: 2025-01-09

Published version
DOI:10.60576/poliba/iris/mandriota-cosimo_phd2025

Publisher: Politecnico di Bari

Terms of use:

(Article begins on next page)

02 May 2026

Politecnico di Bari

LIBERATORIA PER L'ARCHIVIAZIONE DELLA TESI DI DOTTORATO

Al Magnifico Rettore
del Politecnico di Bari

Il/la sottoscritto/a Cosimo Mandriota nato/a a Monopoli (BA) il 22/09/1995

residente a Monopoli (BA) in via Luigi Finamore Pepe, 35 e-mail cosimo.mandriota@poliba.it

iscritto al 3° anno di Corso di Dottorato di Ricerca in Ingegneria Meccanica e Gestionale ciclo 37

ed essendo stato ammesso a sostenere l'esame finale con la prevista discussione della tesi dal titolo:

Adhesion and friction in steady and unsteady viscoelastic contacts

DICHIARA

1) di essere consapevole che, ai sensi del D.P.R. n. 445 del 28.12.2000, le dichiarazioni mendaci, la falsità negli atti e l'uso di atti falsi sono puniti ai sensi del codice penale e delle Leggi speciali in materia, e che nel caso ricorressero dette ipotesi, decade fin dall'inizio e senza necessità di nessuna formalità dai benefici conseguenti al provvedimento emanato sulla base di tali dichiarazioni;
2) di essere iscritto al Corso di Dottorato di ricerca Ingegneria Meccanica e Gestionale ciclo 37, corso attivato ai sensi del "*Regolamento dei Corsi di Dottorato di ricerca del Politecnico di Bari"*, emanato con D.R. n.286 del 01.07.2013;
3) di essere pienamente a conoscenza delle disposizioni contenute nel predetto Regolamento in merito alla procedura di deposito, pubblicazione e autoarchiviazione della tesi di dottorato nell'Archivio Istituzionale ad accesso aperto alla letteratura scientifica;
4) di essere consapevole che attraverso l'autoarchiviazione delle tesi nell'Archivio Istituzionale ad accesso aperto alla letteratura scientifica del Politecnico di Bari (IRIS-POLIBA), l'Ateneo archivierà e renderà consultabile in rete (nel rispetto della Policy di Ateneo di cui al D.R. 642 del 13.11.2015) il testo completo della tesi di dottorato, fatta salva la possibilità di sottoscrizione di apposite licenze per le relative condizioni di utilizzo (di cui al sito http://www.creativecommons.it/Licenze), e fatte salve, altresì, le eventuali esigenze di "embargo", legate a strette considerazioni sulla tutelabilità e sfruttamento industriale/commerciale dei contenuti della tesi, da rappresentarsi mediante compilazione e sottoscrizione del modulo in calce (Richiesta di embargo);
5) che la tesi da depositare in IRIS-POLIBA, in formato digitale (PDF/A) sarà del tutto identica a quelle **consegnate**/inviate/da inviarsi ai componenti della commissione per l'esame finale e a qualsiasi altra copia depositata presso gli Uffici del Politecnico di Bari in forma cartacea o digitale, ovvero a quella da discutere in sede di esame finale, a quella da depositare, a cura dell'Ateneo, presso le Biblioteche Nazionali Centrali di Roma e Firenze e presso tutti gli Uffici competenti per legge al momento del deposito stesso, e che di conseguenza va esclusa qualsiasi responsabilità del Politecnico di Bari per quanto riguarda eventuali errori, imprecisioni o omissioni nei contenuti della tesi;
6) che il contenuto e l'organizzazione della tesi è opera originale realizzata dal sottoscritto e non compromette in alcun modo i diritti di terzi, ivi compresi quelli relativi alla sicurezza dei dati personali; che pertanto il Politecnico di Bari ed i suoi funzionari sono in ogni caso esenti da responsabilità di qualsivoglia natura: civile, amministrativa e penale e saranno dal sottoscritto tenuti indenni da qualsiasi richiesta o rivendicazione da parte di terzi;
7) che il contenuto della tesi non infrange in alcun modo il diritto d'Autore né gli obblighi connessi alla salvaguardia di diritti morali od economici di altri autori o di altri aventi diritto, sia per testi, immagini, foto, tabelle, o altre parti di cui la tesi è composta.

Luogo e data Bari, 4/12/2024 Firma 

Il/La sottoscritto, con l'autoarchiviazione della propria tesi di dottorato nell'Archivio Istituzionale ad accesso aperto del Politecnico di Bari (POLIBA-IRIS), pur mantenendo su di essa tutti i diritti d'autore, morali ed economici, ai sensi della normativa vigente (Legge 633/1941 e ss.mm.ii.),

CONCEDE

- al Politecnico di Bari il permesso di trasferire l'opera su qualsiasi supporto e di convertirla in qualsiasi formato al fine di una corretta conservazione nel tempo. Il Politecnico di Bari garantisce che non verrà effettuata alcuna modifica al contenuto e alla struttura dell'opera.
- al Politecnico di Bari la possibilità di riprodurre l'opera in più di una copia per fini di sicurezza, back-up e conservazione.

Luogo e data Bari, 4/12/2024 Firma 

Politecnico di Bari

Department of Mechanics, Mathematics and Management

Mechanical and Management Engineering
Ph.D. Program

SSD: ING-IND/13 - Applied Mechanics

Final dissertation

Adhesion and friction in steady and unsteady viscoelastic contacts

Cosimo Mandriota

Supervisors:

Prof. Giuseppe Carbone

Prof. Nicola Menga

Coordinator of the PhD Program:
Prof. Giuseppe Casalino

Course XXXVII, 01/11/2021 - 01/11/2024

Politecnico di Bari

Department of Mechanics, Mathematics and Management

Mechanical and Management Engineering
Ph.D. Program
SSD: ING-IND/13 - Applied Mechanics

Final dissertation

Adhesion and friction in steady and unsteady viscoelastic contacts

Cosimo Mandriota

Referees:

Prof.ssa Elena Pierro

Prof. Michele Scaraggi

Supervisors:

Prof. Giuseppe Carbone

Prof. Nicola Menga

Coordinator of the PhD Program:
Prof. Giuseppe Casalino

Course XXXVII, 01/11/2021 - 01/11/2024

Abstract

This thesis presents a novel general energy approach for adhesive contact mechanics of viscoelastic materials. The proposed formulation relies on the virtual work formalism: virtual variations of the contact domain must imply the precise balance between the work of the (external) adhesive forces and the work of internal stresses. Importantly, the latter cannot be simply derived as the variation of a potential energy: the intrinsic non-conservative behavior of viscoelastic materials must be properly considered. For this reason, the mathematical and physical aspects of the energy formulation significantly deviate from equivalent elastic cases. Moving from the assumption of infinitely short range adhesive forces, the proposed approach, in fact, generalizes the Griffith's fracture criterion to hysteretic materials. The closure equation of the steady or unsteady contact problem is derived by enforcing the energy balance at the boundary of the contact area and exploiting boundary formulations based on the Green's function approach. This allows to correctly model the viscoelastic dissipation involving the entire volume of the material, thus overcoming limitations of many previous studies that approached viscoelastic adhesive contacts by assuming that viscoelastic losses are localized at the contact edges and vanish in the bulk of the material. The proposed theory provides results in solid agreement with experimental evidence and insights into the underlying physical mechanisms responsible for the experimentally observed phenomena.

The first part of the thesis focuses on steady-state sliding contacts between rough surfaces. Depending on the sliding velocity, the effective adhesive strength of the system in terms of pull-off force, toughness, and contact area size is found highly enhanced compared to corresponding purely elastic cases, in agreement with experimental evidence. This is ascribable to viscoelastic losses localized at the contact trailing edge, where the energy release rate is increased. This phenomenon also highly affects the frictional response: the velocity-dependent friction coefficient is found significantly increased compared to corresponding adhesiveless conditions. At low velocity values, this behavior depends on local small-scale viscoelastic losses. At intermediate velocity, it reflects a complex interplay between bulk viscoelasticity, small-scale viscoelasticity, and adhesion. Importantly, summing up independent estimations of small-scale and large-scale viscoelastic losses does not provide a correct estimation of the friction coefficient. This is a key result, confirmed by existing experimental studies.

The proposed energy formulation is then extended to general unsteady conditions and applied to analyze the dynamic approach-retraction motion of a rigid sphere

in adhesive contact with a viscoelastic half-space. In this case, besides correctly predicting the effects of local viscoelastic losses, the proposed theory identifies a different fundamental mechanism, also experimentally observed, responsible for adhesion enhancement. Specifically, when the retraction of the indenter begins from a fully relaxed state, the enhancement of the pull-off force depends on a sort of "frozen" state, triggered by the material's glassy response, during which the contact area is almost constant. The different physical mechanisms responsible for the increase of adhesion strength in unsteady conditions are investigated in detail for different loading time-histories and by exploiting a novel approach to correctly calculate the energy release rate for viscoelastic materials under general unsteady conditions. Results clearly indicate that neglecting the viscoelastic response of the bulk material while modeling adhesive contacts might lead to significative errors.
In the last part of the thesis, the proposed theory is applied to investigate crack propagation and healing in viscoelastic solids. When steady-state conditions are assumed, the approach provides results in perfect agreement with previous studies. If this assumption is relaxed, the theory is able to correctly tackle complex unsteady phenomena, as the so called delayed-fracture: under a given applied load, the fracture of a viscoelastic solid may occur after a certain delay-time, whose order of magnitude corresponds to that of the material's relaxation time.
Overall, the proposed energy formulation might be of interest in several engineering application, in which the effects of the interplay between viscoelasticity and adhesion on the contact behavior must be properly controlled and designed, such as, for instance, structural adhesives, pressure-sensitive adhesives, protective coatings, bio-inspired adhesives, orthopedic applications, micro-electro-mechanical systems, micro-manipulations and micro-assembly.

Contents

List of Figures

Introduction

0.1 Research context and background

Understanding the effect of adhesion in contact mechanics of rubbery-like materials is a long standing problem. Scientific interest in the field is driven by the relevance of the topic in several physical phenomena and engineering applications, e.g., in structural adhesives used in aerospace [1] and automotive industries [22], medical applications [2–5], pressure sensitive adhesives [6, 7], biological and bio-inspired systems [8–13], touchscreens [14]. Controlling and tuning adhesion is a fundamental engineering task. Often, the adhesive effect is desirable, e.g. it might enhance the sliding friction in the tire–road contact thus improving the braking and the handling performances [15]. In other cases, it might be detrimental or require precise control, as in micro- and nano- scales electro-mechanical [16–20] or photonic [21] systems. Indeed, as the size of these systems continues to decrease, their mechanical behavior is increasingly governed by adhesive forces due to high surface-to-volume ratios. Therefore, avoiding permanent adhesion between moving components is a crucial issue [22] and pick and place procedures must be designed ad hoc to achieve the adhesion control required for grabbing and releasing objects [18, 23, 24].
Over the last decades, countless theoretical, numerical and experimental studies have been devoted to investigating the effect of adhesion on the macroscopic contact quantities. Overall, the adhesive contact behavior of rubbery like materials undergoing relative motion is highly affected by their intrinsic viscoelastic response. E.g., in sliding contacts between rough surfaces the hysteretic losses occurring during cyclic deformations eventually result into a lateral force opposing the relative motion, commonly referred to as viscoelastic friction [25, 26]. Importantly, experimental evidences indicate that the overall frictional response depends on a complex interplay between adhesion and viscoealsticity [27]. This eventually results into a significative increase of the friction coefficient compared to adhesiveless conditions, which has never been fully understood. Similar phenomena are observed in rolling contacts. In this case, besides affecting the torque required to sustain the rolling motion [28–31], viscoelasticity might cause a significative increase of the effective adhesive strength under tensile loads, compared to static conditions, which is found to depend on the rolling speed [32]. The viscoelastic-induced adhesion enhancement has been widely experimentally observed and investigated in the presence of purely normal motion. Indentation-retraction tests

performed with adhesive rubber substrates, the so called JKR-dynamics tests, are often devoted to investigating how the pull-off force enhancement depends on the retraction speed [33–36]. Importantly, the enforced loading time-history plays a major role in determining the overall adhesive behavior.
However, a comprehensive theory of viscoelastic adhesion is currently lacking, and many of the observed phenomena are not fully understood yet.
The pioneering theoretical study on adhesion between elastic solids dates back to 1971, when Johnson, Kendall, and Roberts (JKR) presented their seminal paper [38] on adhesive elastic spheres. Exploiting the Griffith's energy balance under the assumption of infinitely short-range adhesive forces, the JKR model provided results in perfect agreement with experiments and is nowadays still considered a cornerstone in the field. Indeed, the same energy balance approach has since been shown to be highly versatile and effective, and has been applied in a wide class of smooth [37,39] and rough [40–42] elastic contacts. Many of these studies included variables that were not addressed in the original JKR model, such as the effect of tangential stresses in sliding contacts [43,44], thickness of layered coatings [45,46], and different geometries and boundary conditions [47–50]. In 1977 Tabor [51] suggested that the assumption of infinitely short range adhesive forces is correct for soft materials in the presence of high surface energy, as indeed confirmed by many subsequent studies [52–54]. Among the several different approaches that have been proposed over the decades to include adhesive interactions in contact mechanics, many of them based on local force equilibrium [52–54], the energy balance approach has fundamental advantages. Indeed, it can correctly model adhesive contacts only requiring a few quantities as inputs: the Young modulus and Poisson ratio of the isotropic elastic material, and the adhesion energy per unit area $\Delta\gamma$. The latter, in particular, has a very simple definition in terms of macroscopic quantities and can be easily measured through reliable experimental procedures, regardless of the detailed interfacial gap dependence of the molecular interactions. Hence, once the experimental data are acquired using, for instance, micro-scale optical microscopy [55], scratch tests [56], peeling processes [57], or macro-scale spherical indentation-retraction tests [58,59], $\Delta\gamma$ can be easily derived by fitting them with the corresponding elastic contact model.
Nevertheless, the JKR contact theory falls short in tackling adhesive contact problems when quasi-static conditions are not ensured, as clearly indicated by experimental evidences. Indeed, the non-conservative nature of viscoelastic materials makes the Griffith energetic balance no longer valid. As a consequence, the most common approach adopted to model adhesive contacts is to assume that viscoelastic losses occur very locally at the boundary of the contact area, while in the bulk the material response is governed by the soft elastic modulus. This assumption, known as "small-scale viscoelasticity" hypothesis, is often exploited both in sliding [37], rolling [60–62] and JKR-like dynamic [33,63–67] contacts. Within this framework, the proper elastic contact model is exploited to relate the contact quantities, with the adhesion energy $\Delta\gamma$ replaced by a velocity-dependent term [68–72] accounting for local viscoelastic losses. However, neglecting viscoelasticity within the bulk of the material might lead to significative errors, unless the characteristic

size a of the system is $a \gg V\tau$, where V is a characteristic velocity and τ the relaxation time of the material. Indeed, in order to overcome this limitation, most of the existing studies on adhesive viscoelastic contacts exploit local force equilibrium where the contacting surface are discretized in particles or elements which interact with the corresponding particles/elements of the counter surface through local forces, derived by gap-dependent potentials, e.g. $m-n$ potentials [73], as the Lennard-Jones (LJ) law [65,66,74–77,135], exponentially short-range laws [78,79], and cohesive-zone models specifically designed for contact [80–83] and fracture mechanics [68, 84] problems. However, as clearly observed by Persson [85] and Greenwood [86], the contact behavior is weakly affected by the specific law implemented to describe the interfacial adhesive interaction, provided that the range of microscopic gap dependent law is much shorter than any other length scale involved in the problem. This suggests that most of the phenomena in viscoelastic contacts can be captured by general energy equilibrium.

0.2 The outline of the thesis

Aiming a filling this gap in the literature, this thesis presents a novel general energy formulation to study steady and unsteady adhesive contact and fracture mechanics of viscoelastic materials. The proposed approach, moving from the assumption of infinitely short-range adhesive forces, generalizes the Griffith's fracture criterion to viscoelastic materials. The closure equation of the visoelastic-adhesive problem is formulated by exploiting the virtual work formalism, both for steady and unsteady conditions. This requires that the variation of adhesive energy caused by a virtual variation of contact area is precisely balanced by the work of internal stresses. The non-conservative nature of viscoelastic materials is properly considered. The thesis is outlined as follows. Chapter 1 presents an overview of the energy approach in fracture mechanics and adhesive contact mechanics of elastic materials, with specific focus on the Griffith's fracture criterion and the JKR theory. In the same chapter, pivotal arguments needed to extend the energy formulation to non-conservative systems are introduced. Chapter 2 consists of a general overview of the linear viscoelastic rheological behavior, with specific focus on the viscoelastic Green's functions for steady and unsteady conditions. These concepts and mathematical frameworks are widely invoked and applied in the subsequent chapters. Chapter 3 focuses on steady-state sliding adhesive contacts between rough surfaces: the frictional and adhesive behavior is investigated over a wide range of sliding velocity, spanning the entire viscoelastic spectrum of the material. Importantly, the proposed theory confirms aforementioned experimental evidences, as the adhesion-induced enhancement of the viscoelastic friction coefficient, and the viscoelastic-induced increase of adhesive strength, confirming that the interplay between adhesion and viscelasticity plays a major role in determining the overall contact behavior. In Chapter 4 the theoretical formulation presented in Chapter 3 is generalized to unsteady conditions, with specific focus on dynamic JKR-like contacts. The enhancement of the effective adhesion is investigated for different

time-histories loading, and results are in solid agreement with several experimental evidences. Notably, the theory provides deep insights on the physical mechanisms responsible for the overall contact behavior. In Chapter 5 the same approach is applied to steady-state and unsteady crack propagation in viscoelastic solids. In the steady-state case, the theory is compared with previous studies. The unsteady case study focuses specifically on the so-called delayed fracture of viscoelastic materials.

Chapter 1

Energy approach in fracture and contact mechanics

This chapter introduces the theoretical background of this thesis. In Secs. (1.1, 1.2) the main aspects of the Griffith's fracture criterion are discussed. Based on the energy formulation, the Griffith's criterion establishes a versatile and effective mathematical framework in the field of fracture and contact mechanics of elastic solids. In Sec. 1.3, the JKR theory of adhesive elastic contacts is reviewed: the mathematical formulation of the model is presented, alongside a brief discussion on the so called DMT-JKR transition that defines the physical framework in which the assumption of infinitely short range adhesive forces is valid. Sec. 1.4 clarifies that the Griffith's energy balance is, in fact, a specific case of the general principle of virtual work applied to fracture mechanics of conservative materials. Indeed, the equilibrium condition of minimum energy can be alternatively derived by balancing the work at the crack tip between internal stresses and adhesive forces. This means that, for elastic materials, the work of internal stresses corresponds to the change in elastic energy. On the other hand, for non-conservative materials, as for viscoelastic materials, the work of internal stresses can be split into a conservative (i.e., path independent) term plus a non-conservative (i.e., path-dependent) contribution. The latter is directly related to the asymmetric part of the response matrix or, similarly, in continuum mechanics, to the asymmetric part of the response function of the system. These concepts lay the mathematical and theoretical foundation for the theory object of this dissertation: the closure equation for the viscoelastic contact or crack problem can be rigorously formulated by exploiting the work balance at the contact edges (see Chapter 3 for steady state conditions and Chapter 4 for unsteady contacts) or, similarly, at the tip of a crack (see Chapter 5) in virtue of the virtual work principle. Importantly, the non-conservative nature of the problem makes the physical and mathematical aspects of the equilibrium formulation significantly different compared to the corresponding elastic contact or crack cases.

1.1 The Griffith's fracture criterion

The empirical evidence that the rupture of solids occurs under applied stresses significantly lower than the theoretical one required to break atomic bonds has prompted scientific and engineering interest in crack propagation. Indeed, fracture typically initiates from pre-existing cracks or nucleation of flaws, which cause a significant amplification of local stress [87], leading to a continuous unzipping of molecular bonds at the crack's tip. Similar phenomena occur when two bodies in contact are pulled apart or pressed together. In this case, molecular interactions at the contact interface (e.g., Van der Waals forces) are involved in the continuous breaking or creation of adhesive bonds as the contact area's boundary recedes or advances. The concept of surface energy was introduced in fracture mechanics by Griffith [88] in 1921. In his seminal paper, Griffith observed that the crack propagation can occur as long as the energy required to break molecular bonds can be supplied, namely, when:

$$G \geq \Delta\gamma \tag{1.1}$$

where $\Delta\gamma$ is the surface energy per unit area and

$$G = -\frac{d\Pi}{da} \tag{1.2}$$

is the energy release rate, quantifying the change of the system's mechanical potential energy Π per unit variation of the crack area a. In particular, Π depends on two energy contributions: the elastic energy stored within the solid resulting from the internal strain field, and the potential energy of external forces. Notably, the same energy balance extends to contact mechanics, in which variations of contact area locally resemble the propagation of a crack in the normal direction to the contact boundary. Referring to the simple general schematic representation shown in

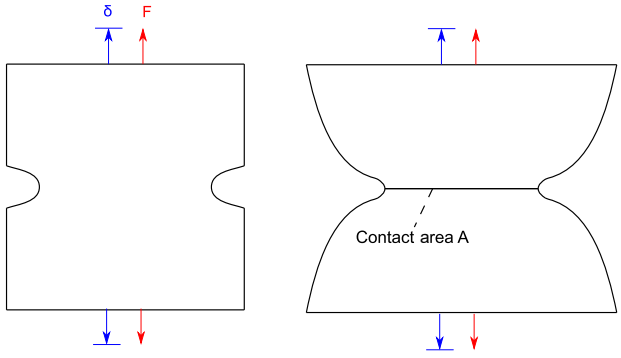

Figure 1.1: A simple schematic of the general crack or adhesive contact problem

Fig.1.1, the Griffith's energy balance criterion can be exploited by relating the total energy of the system, in particular its elastic energy, to its macroscopic mechanical parameters, i.e., the remotely applied force F, the remote displacement δ and the contact area A (or, analogously, the undamaged area of the cracked specimen). However, according to the Gibbs phase rule, only two of the three quantities are independent, i.e., one can find a state equation in the form $f(F, \delta, A) = 0$. Therefore

the elastic energy stored in the system can be differentiated as:

$$dU_{el} = \left.\frac{\partial U_{el}}{\partial A}\right|_{\delta} dA + \left.\frac{\partial U_{el}}{\partial \delta}\right|_{A} d\delta \tag{1.3}$$

Then, in writing the energy equilibrium, the controlled parameter must be specified. Assuming that imposed displacement is held constant, the work of the applied force $Fd\delta$ vanishes, and the only energy contribution driving the creation of free surfaces is the elastic energy stored in the body. In this case, the variation of the system's total internal energy $\mathcal{U} = \Pi - \Delta\gamma A$ resulting from virtual variations dA of the contact area is :

$$d\mathcal{U} = \left.\frac{\partial U_{el}}{\partial A}\right|_{\delta} dA - \Delta\gamma dA = (G - \Delta\gamma)\, dA \tag{1.4}$$

where the energy release rate $G = G(A, \delta)$. On the other hand, when the applied force is held constant, since δ changes, the associated potential energy $-F\delta$ is involved in the energy balance. In this case, according to Eq. (1.3), the variation of the total energy is

$$\begin{aligned} d\mathcal{U} &= d(U_{el} - F\delta - \Delta\gamma A) = && (1.5)\\ &= \left.\frac{\partial U_{el}}{\partial A}\right|_{\delta} dA + \left.\frac{\partial U_{el}}{\partial \delta}\right|_{A} \left.\frac{\partial \delta}{\partial A}\right|_{F} dA + && (1.6)\\ &- F \left.\frac{\partial \delta}{\partial A}\right|_{F} dA - \Delta\gamma dA && (1.7) \end{aligned}$$

However, observing that $\partial U_{el}/\partial\delta|_A = F$, we recover again Eq. (1.4). Thus both for fixed displacement and force, the equilibrium condition is:

$$G = \left.\frac{\partial U_{el}}{\partial A}\right|_{\delta} = \Delta\gamma \tag{1.8}$$

Supposing that the initial contact area A and the imposed displacement or force are such that $G > \Delta\gamma$, the crack propagates, and the quantity $G - \Delta\gamma$ is the generalized force driving the crack's acceleration. On the contrary, if $G < \Delta\gamma$ the adhesive interactions overcome the elastic response of the material and the contact area increases. Thus, the contact area changes over non-equilibrium states as long as the total energy $\mathcal{U}(A)$ decreases, i.e., until a minimum point of $\mathcal{U}(A)$ is reached. Hence, the energy release rate is a fundamental quantity in fracture and contact mechanics. For elastic materials, in order to solve the crack or contact problem one must derive the dependence of the energy release rate from macroscopic quantities (e.g., the remotely applied displacement and the crack's length or the dimensions of a notch). This has been done for different geometries by directly calculating the strain elastic energy stored in the material volume (see [89–91] and Sec. 1.4), i.e.,

$$U_{el} = \frac{1}{2}\int \sigma_{ij}\epsilon_{ij} dV \tag{1.9}$$

where σ_{ij} and ϵ_{ij} are the internal stress and strain tensors and we used the Einstein notation of repeated index. However, in 1957, Irwin [91] demonstrated that the general expression of the energy release rate for mode-I cracks is

$$G = \frac{K_I^2}{2E^*} \tag{1.10}$$

(see Sec. (1.4) for a demonstration). In Eq. (1.10), K_I is the stress intensity factor of the square-root stress singularity at the crack tip [91], $E^* = E/(1-\nu^2)$ in plane strain and $E^* = E$ in plane stress, being E the elastic material's Young modulus. Therefore, the crack problem can be solved by relating the stress intensity factor to the remotely applied loading condition depending on the specific problem's geometry [89–91].

1.2 Thermodynamical point of view

As shown in the previous section, a different potential is stationary at the equilibrium depending on the specific physical ensemble of the problem. The proper thermodynamic potential can be identified by exploiting the Legendre transform formalism [90, 93]. Let us consider the so called fundamental equation of a thermodynamical system:

$$U = U(X_1, X_2, ...X_N) \tag{1.11}$$

where $X_1, ..., X_N$ are the extensive parameters and U is the internal energy. The partial derivatives of the internal energy $Y_i = \partial U/\partial X_i$ are the intensive parameters. E.g., the temperature T is the partial derivative with respect to the entropy and the pressure is the partial derivative with respect to the volume.
A Legendre transform Φ of U is defined on a subset of $n < N$ variables as

$$\Phi = U - \sum_{i=1}^{n} Y_i X_i \tag{1.12}$$

Now, according to Eq. (1.11), we can write

$$dU = Y_1 dX_1 + Y_2 dX_2 + ... + Y_N dX_N \tag{1.13}$$

Therefore, using Eqs. (1.11, 1.13) we get

$$d\Phi = -X_1 dY_1 - ... - X_n dY_n + Y_{n+1} dX_{n+1} + ... + Y_N dX \tag{1.14}$$

Hence, the potential Φ can be written as

$$\Phi = \Phi(Y_1, ...Y_n, X_{n+1}, ...X_N) \tag{1.15}$$

Assuming that our thermodynamic system is a body containing a pre-existing crack, or similarly two bodies in adhesive contact, as in Fig.1, the fundamental equation is:

$$U = U\left(S, \delta, A\right) \tag{1.16}$$

where S is the entropy. The differential form of Eq. (1.16) introduces the intensive thermodynamical parameters:

$$dU = TdS + (G - \Delta\gamma)\, dA + Fd\delta \tag{1.17}$$

The meaning of Eq. (1.17) is that the variation of internal energy between two states equates the work $\delta L = (G - \Delta\gamma)\, dA + Fd\delta$ plus the heat $\delta Q = TdS$ that are supplied in reversible transformations. Of course the entropy cannot be controlled in practical terms, and lab tests are usually carried out by keeping the force or the displacement constant, and temperature variations are often negligible. Therefore, it is convenient to move from the internal energy to the Helmholtz free energy or to the Gibbs free energy by taking the Legendre transforms of U. The Helmholtz free energy is the Legendre transform of the internal energy on the entropy, which is replaced by the temperature $T = \partial U/\partial S$:

$$\mathcal{F} = U - TS = \mathcal{F}(T, \delta, A) \tag{1.18}$$

Instead, the Gibbs free energy $\mathcal{G}$ is the Legendre transform of the internal energy on the entropy and the displacement, which are replaced by the temperature and the force $F = \partial U/\partial\delta$:

$$\mathcal{G} = U - TS - F\delta = \mathcal{G}(T, F, A) \tag{1.19}$$

These definitions imply that $\mathcal{F}$ and $\mathcal{G}$ are stationary at equilibrium under fixed displacement and fixed force, respectively, and constant temperature. Indeed, using Eqs. (1.17, 1.18, 1.19) and recalling $dT = 0$ we get:

$$d\mathcal{F} = dU - TdS = (G - \Delta\gamma)\, dA \tag{1.20}$$

for constant T and constant δ and

$$d\mathcal{G} = dU - TdS - Fd\delta = (G - \Delta\gamma)\, dA \tag{1.21}$$

for constant T and constant F. Moreover, the Second Law of Thermodynamics entails that the equilibrium point is a minimum of the total energy. Indeed, under fixed grips, when the contact area changes spontaneously (i.e., through non-equilibrium configurations), the variation of internal energy in the irreversible process is $dU = \delta Q \leq TdS$ where δQ is the heat supplied to the system to ensure that the temperature is held constant. Substituting into Eq. (1.20) leads to

$$d\mathcal{F} \leq 0 \tag{1.22}$$

Similarly, when the force is held constant it provides the amount of work $Fd\delta$, thus we get $dU = \delta Q + Fd\delta$, where $\delta Q \leq TdS$. Thus, using Eq. (1.21) yields

$$d\mathcal{G} \leq 0 \tag{1.23}$$

Eqs. (1.22, 1.23) show that the contact area can change spontaneously as long as the potential energy decreases, until its minimum is reached. This represents a stability criterion of the equilibrium point that reads as

$$\left.\frac{\partial G}{\partial A}\right|_{\delta} = \left.\frac{\partial^2 \mathcal{F}}{\partial A^2}\right|_{\delta,T} > 0 \tag{1.24}$$

$$\left.\frac{\partial G}{\partial A}\right|_{F} = \left.\frac{\partial^2 \mathcal{G}}{\partial A^2}\right|_{F,T} > 0 \tag{1.25}$$

1.3 The JKR theory of adhesive contacts of elastic solids

The first attempt to generalize the Griffith fracture criterion to the adhesive contact mechanics of elastic solids was made by Johnson, Kendall, and Roberts (JKR). Their seminal paper [38], published in 1971, is a milestone in the field. In this section, we briefly review the general formulation of the JKR adhesive contact model. We consider a rigid sphere of radius R in adhesive contact with a linear elastic

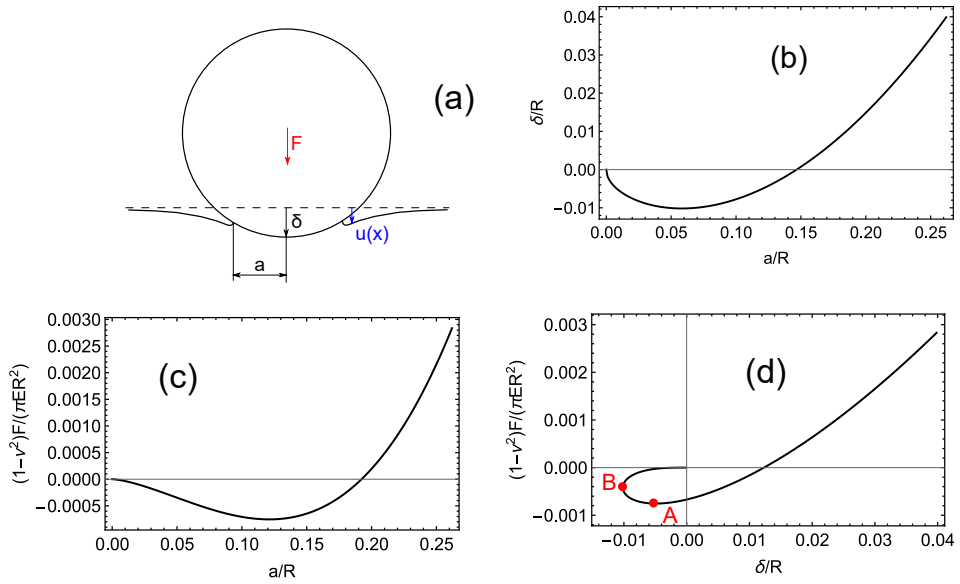

Figure 1.2: The JKR theory's results [38]. (a) the schematic of the contact problem between a rigid sphere and an elastic half-space. (b) The dimensionless contact penetration vs. the dimensionless contact radius. (c) The dimensionless applied force vs. the dimensionless contact radius. (d) The dimensionless force vs. the dimensionless contact penetration. Results are shown for dimensionless adhesion energy $\left(1-\nu^2\right)\Delta\gamma/\left(\pi E_0 R\right) = 0.00016$.

half-space, as shown in Fig. 1.2 (a). The JKR model relies on the assumption of infinitely short range adhesive forces: the (local) normal tractive stress among two interacting surface can be sustained as long as their normal separation approaches zero. Within this framework, the contact area can be precisely identified

as the region in which a pressure distribution is developed and the gap between the bodies in contact is assumed exactly equal to zero within the whole contact region. In order to calculate the elastic energy stored in the system, the pressure distribution within the contact area must be calculated as function of the contact radius a and of the contact penetration δ, and the value of a that satisfies the global energy equilibrium has to be determined as a part of the solution. With this regard, we observe that in the problem at hand, invoking linearity and translational invariance, the normal interfacial displacement field and the normal pressure distribution are related each other as:

$$u(\mathbf{x}) = \int d^2x_1 \mathcal{G}(\mathbf{x} - \mathbf{x}_1) p(\mathbf{x}_1) \tag{1.26}$$

Where $\mathbf{x}$ is the in-plane vector position and $\mathcal{G}(\mathbf{x})$ is the Green's function:

$$\mathcal{G}(\mathbf{x}) = \frac{1-\nu^2}{\pi E} \frac{1}{|\mathbf{x}|}$$

where E and ν are the Young modulus and the Poisson ratio of the isotropic elastic material. $\mathcal{G}(\mathbf{x})$ represents the surface displacement resulting from a Dirac Delta pressure distribution, and was determined by Boussinesq in 1885 [94]. We notice that, for a given value of the indentation of the sphere δ and a given contact radius a, the displacement field is known within the contact area, where it must precisely match the indenter's shape, i.e., $u(\mathbf{x}) = \delta - |\mathbf{x}|^2/(2R)$, where $\mathbf{x}$ is the in-plane vector position and the assumption that $a \ll R$ has been made. Then, since $p(\mathbf{x})$ vanishes outside the contact domain Ω, writing Eq. (1.26) for $\mathbf{x} \in \Omega$ allows to solve it for the pressure distribution $p(\mathbf{x})$. The general solution is:

$$p(\mathbf{x}) = p_0 \left(1 - |\mathbf{x}|/a\right)^{-1/2} + p_1 (1 - |\mathbf{x}|/a)^{1/2} \tag{1.27}$$

where

$$p_0 = \frac{1}{\pi} \frac{E}{1-\nu^2} \left(\frac{\delta}{a} - \frac{a}{R} \right) \tag{1.28}$$

$$p_1 = \frac{1}{\pi} \frac{E}{1-\nu^2} \frac{2a}{R} \tag{1.29}$$

The term p_1 is associated with a component of the pressure field that vanishes at the boundary of the contact area whereas the term p_0 reflects the presence of the standard square-root singularity at the contact boundary, where the internal stresses and deformations resemble those recovered at the tip of a crack. Moreover, positive values of p_0 would entail the interpenetration between solids and must be discarded. In absence of adhesive forces only repulsive stresses are allowed, hence p_0 must vanish. Eqs. (1.27, 1.28) show that, in this case, the contact radius must take the value $\sqrt{\delta R}$, i.e., the solution obtained by Hertz in 1882 for adhesiveless elastic contacts [95]. In the presence of adhesion, the energy equilibrium must be enforced to determine the equilibrium value of the contact radius. With this regard, the elastic energy

$$U_{el} = \frac{1}{2} \int d^2x p(\mathbf{x}) u(\mathbf{x}) \tag{1.30}$$

depends the contact quantities as:

$$U_{el}(\delta, a) = \frac{E}{1-\nu^2}\delta^2\left(a - \frac{2}{3}\frac{a^3}{\delta R} + \frac{1}{5}\frac{a^5}{R^2\delta^2}\right) \tag{1.31}$$

Eq. (1.31) is obtained by substituting Eq. (1.27) into Eq. (1.30). Hence, the total energy $\mathcal{U}(\delta, a) = U_{el}(\delta, a) + U_a(a)$ of the system is the elastic energy plus the adhesion energy $U_a(a) = -\Delta\gamma\pi a^2$. The equilibrium value of a is then determined by enforcing that $\mathcal{U}$ is stationary under fixed grips, i.e., by enforcing that $\partial\mathcal{U}/\partial a|_\delta = 0$. This allows to derive the relation between the contact radius and the penetration:

$$\frac{\delta}{R} = \left(\frac{a}{R}\right)^2 - \left(\frac{a}{R}\right)^{1/2}\sqrt{\frac{2\pi(1-\nu^2)\Delta\gamma}{ER}}$$

and, in turn, between the total compressive force $F = \int d^2x p(\mathbf{x})$ and the contact radius:

$$\frac{1-\nu^2}{ER^2}F = \frac{4}{3}\left(\frac{a}{R}\right)^3 - 2\left(\frac{a}{R}\right)^{3/2}\sqrt{\frac{2\pi(1-\nu^2)\Delta\gamma}{ER}}$$

These relations are plotted in Fig. 1.2 (b) and (c) in terms of dimensionless parameters. Fig. (d) shows the equilibrium curve of the dimensionless force vs. the normalized displacement. In the figure, points A and B identify the pull-off points for force-controlled and displacement-controlled conditions, respectively. Importantly, the maximum tensile force (i.e., the pull-off force)

$$F_{\text{JKR}} = 1.5\pi R\Delta\gamma \tag{1.32}$$

is independent on the Young modulus.

1.3.1 The DMT-JKR transition

Over the last decades, several approaches have been proposed to include the interfacial adhesion in contact mechanics of elastic solids. A common approach is to exploit the detailed description of the adhesive interaction among the gap between interacting surfaces and enforce the local force equilibrium. The gap-dependent stress is usually derived from $m-n$ potentials, as the Lennard-Jones one [65, 66, 74–77, 135], which leads to the following stress vs. gap expression:

$$\sigma(g) = \frac{8\Delta\gamma}{3\varepsilon}\left[\left(\frac{\varepsilon}{g}\right)^3 - \left(\frac{\varepsilon}{g}\right)^9\right]$$

including a repulsive branch for $g < \varepsilon$ and an adhesive (tensile) branch for $g > \varepsilon$, where ε is the inter-molecular equilibrium distance and g the normal gap. Bradley (1932) [96] and Derjaguin (1934) [97] computed the total force between a sphere and an half-space by neglecting deformations of the bodies and exploiting L-J like surface potentials, and obtained a pull-off force equal to $2\pi R\Delta\gamma$. This value is in apparent contradiction with the JKR theory [see Eq. (1.32)]. Indeed, since in the

JKR model the pull-off force is independent on the Young modulus, one would expect the same result to apply also for rigid bodies. Later, Derjaguin, Muller and Toporov (DMT) proposed different approaches to take elastic deformations into account, see [98] (1975) and [99] (1983). The DMT model assumes that in the presence of adhesion the shape of deformed profiles is exactly the same predicted by the Hertz theory and that adhesive forces act outside of the hertzian contact area according to the gap-stress adhesive law. Under these assumptions, the pull-off force is again equal to $2\pi R\Delta\gamma$ and again differs from the JKR prediction. This contradiction was finally explained by Tabor [51] in 1976, who recognized that the JKR and the DMT theories represent two limit physical conditions corresponding to limits of a dimensionless parameter, usually referred to as Tabor parameter:

$$\mu = \left(\frac{\Delta\gamma^2 R}{E^2\varepsilon^3}\right)^{1/3}$$

The JKR theory is valid for $\mu \gg 1$. Under these conditions, the effect of short-range adhesive stresses acting outside the contact area is not significant on the overall contact behavior and the assumption of infinitely short range adhesive forces is reasonable. On the other hand, the DMT theory applies when the effect of deformations induced by long-range adhesive interactions outside the contact area is negligible, i.e., when $\mu \ll 1$. Overall, the adhesive contact behavior undergoes a gradual transition among the two limit theories when μ spans its entire spectrum. Tabor's predictions were widely confirmed by subsequent studies and accurate numerical simulations based on local force equilibrium [52–54]. Greenwood [54] suggested that the JKR theory becomes exact for $\mu \gg 3$. Hence, the JKR approach can be correctly applied to model the adhesive contact behavior of a wide class of soft materials. In this thesis we focus on soft rubbery-like materials for which the assumption of infinitely short range adhesive force is reasonable.

1.4 Work and energy in non-conservative systems

The Griffith's fracture criterion and the JKR model are limited to purely elastic materials. On the other hand, in non-conservative systems, e.g., for solids exhibiting a viscoelastic response, the work of internal stresses cannot be expressed as the variation of potential energy. Therefore, the general theoretical framework that allows to include non-conservative responses is the virtual work principle. In order to define the theoretical framework of this thesis, in the first part of this section we briefly review the virtual work principle according to the classical D'Alembert's formulation, highlighting concept that are pivotal in the energy formulations presented in Chapters (3, 4, 5) for viscoelastic adhesive contacts and crack propagation. In the second part, we elucidate how the non-conservative nature of a mechanical system depends on the asymmetric nature of its response function and how the work of internal stresses can be split in conservative and

non-conservative contributions. These concept will be widely referenced in all of the subsequent chapters.

1.4.1 Principle of Virtual Work

The D'Alembert's Principle of Virtual Work [100, 101] states that the total work of active forces plus inertial forces over virtual displacements is zero. The active forces include all the internal and external forces, except for the reaction forces associated with constraints that are postulated to not perform work under any virtual displacement. By writing the principle of virtual work for a system composed of N particles, the Euler-Lagrange equations of motion are immediately derived. In general, the position vectors of the particles $\mathbf{P}_i = \mathbf{P}_i(q_1, q_2, ..., q_m, t)$ explicitly depend on the Lagrangian coordinates $q_1, q_2, ..., q_m$ and on time, and a virtual displacement $\delta\mathbf{P}_i$ is defined as:

$$\delta\mathbf{P}_i = \sum_{k=1}^{m} \frac{\partial \mathbf{P}_i}{\partial q_k} \delta q_k \tag{1.33}$$

where δq_k are arbitrary virtual variations of the Lagrangian parameters. Eq. (1.33) shows that a virtual displacement is a displacement admitted by constraints at "frozen" time. This differs from the actual displacement, which instead is associated with the point velocity

$$\dot{\mathbf{P}}_i = \sum_{k=1}^{m} \frac{\partial \mathbf{P}_i}{\partial q_k} \dot{q}_k + \frac{\partial \mathbf{P}_i}{\partial t} \tag{1.34}$$

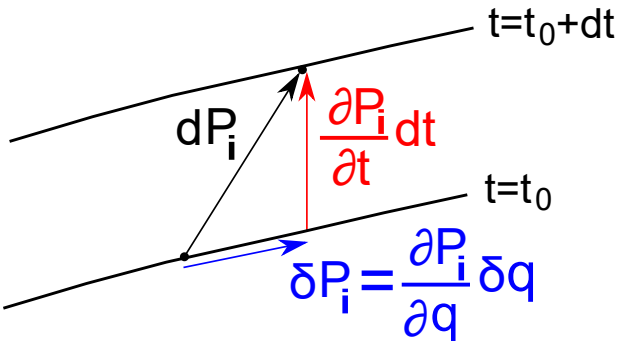

Figure 1.3: A point constrained on a moving line: the virtual displacement (blue) and the actual displacement (black).

Note that the component $\partial \mathbf{P}_i/\partial t$ might depend, for instance, on the presence of a time-dependent moving constraint, as shown in Fig. 1.3 , and is not included in the virtual displacement $\delta \mathbf{P}_i$. This concept will be recalled in Chapter 4 during the derivation of the energy formulation of unsteady viscoelastic contacts. Then, the total work of active forces $\mathbf{F}_i$ plus inertial forces $-m_i \mathbf{a}_i$ (being $\mathbf{a}_i$ the acceleration and m_i the mass of the particles) reads as:

$$\sum_{i=1}^{N} \left(\mathbf{F}_i - m_i \mathbf{a}_i \right) \cdot \delta \mathbf{P}_i = \sum_{k=1}^{m} \left(Q_k - \tau_k \right) \delta q_k = 0 \tag{1.35}$$

where $Q_k = \sum_{i=1}^{N} \mathbf{F}_i \cdot \partial \mathbf{P}_i/\partial q_k$ and $\tau_k = \sum_{i=1}^{N} \left(m_i \mathbf{a}_i \right) \cdot \partial \mathbf{P}_i/\partial q_k$ are usually called generalized forces. Since Eq. (1.35) must hold for any virtual displacement δq_k, we obtain:

$$Q_k - \tau_k = 0, \; k = 1, ..., m \tag{1.36}$$

i.e, the m equations of motions, valid both for conservative and non-conservative systems. In the presence of only conservative forces, the generalized force can be written as $Q_k = -\partial U/\partial q_k$, where $U(q_1, q_1, ..., q_k)$ is the total potential energy. The same arguments are immediately extendable to continuum mechanics. Let us consider a deformable solid subjected to generic time dependent internal stress tensor $\sigma_{ij}(\mathbf{x}, t)$, surface stress vector $\sigma(\mathbf{x}, t)$ and volume forces $\mathbf{f}(x, t)$. Let $\mathbf{u}^*(\mathbf{x})$ and $\varepsilon^*_{ij}(\mathbf{x})$ be an admitted virtual displacement vectorial field and its associated compatible virtual deformation field. This means that they are related each other through the compatibility equations:

$$\varepsilon^*_{ij}(\mathbf{x}) = \frac{1}{2} \left(\frac{\partial u^*_i}{\partial x_j} + \frac{\partial u^*_j}{\partial x_i} \right) \tag{1.37}$$

Notably, a virtual displacement field is a regular field admitted by constraints and is not (at least, not necessarily) related to the stress field by a constitutive equation. Moreover, the stress state is equilibrated. Then, generalizing Eq. (1.35) to continuum mechanics is equivalent at expressing that at a generic time instant t, the work of the internal stress tensor over the internal deformations $[L_{int}(t)]$ is balanced by the work of all the external forces $[L_{ext}(t)]$:

$$L_{int}(t) = \int_V \sigma_{ij}(\mathbf{x},t) \varepsilon^*_{ij}(\mathbf{x}) dV = \int_S \sigma(\mathbf{x}, t) \cdot \mathbf{u}^*(\mathbf{x}) dA + \int_V \mathbf{f}(\mathbf{x}, t) \cdot \mathbf{u}^*(\mathbf{x}) dV = L_{ext}(t) \tag{1.38}$$

where no assumptions have been made about the rheological behavior of the material and inertial forces have been neglected. Eq. (1.38) follows straightforward from the consideration that the sum of the works done by the internal stresses acting on each side of the infinitesimal element of volume dV plus the work of volume forces is

$$\delta L = \sigma_{ij}(x, t) \varepsilon^*_{ij}(x) dV$$

as long as the equilibrium equation $\mathrm{div}[\sigma_{ij}] + \mathbf{f} = \mathbf{0}$ and Eq. (1.37) hold. Then, summing up all the elementary works over all the elements implies that, since the

displacement field is regular, all the work terms resulting from stresses acting over adjacent sides elide each other and Eq. (1.38) is recovered.
Moving back to fracture mechanics of elastic solids, the Griffith's energy balance equation [i.e., Eq. (1.8)] is equivalent at enforcing the virtual work balance expressed by Eq. (1.38) at the tip of a crack. This can be exploited if we consider

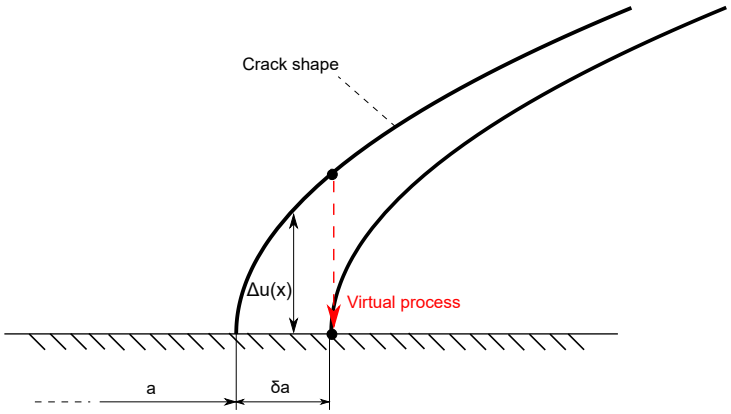

Figure 1.4: The local virtual process describing the variation of the crack's length.

that the crack's tip position (i.e., the Lagrangian parameter) is "virtually" increased of the arbitrarily small amount δa as shown in figure 1.4, while the remote displacement δ is kept fixed. In this process, the work of the external adhesive forces in Eq. (1.38) is due to the change of adhesive energy resulting from the variation of contact area, i.e., $\delta L_{ext} = -dU_a = \delta a \Delta\gamma$. In order to calculate the work of internal stresses we observe that the virtual process corresponds to a change of the the asymptotic displacement at the crack tip. This can be described as $\delta u\left(x,\eta\right) = \Delta u\left(x\right)\delta\eta$ where η is a process parameter increasing from 0 to 1 during the change of crack length and $\Delta u\left(x\right)$ is the displacement gap shown in the figure. Linearity between stresses and displacements then implies that the interfacial stress during the η-governed process is $\sigma\left(x,\eta\right) = \eta\ \sigma_+\left(x\right)$ for $x \in [a, a+\delta a]$ where $\sigma_+\left(x\right)$ is the stress field recovered at the end of the process. The work δL_{int} done by the internal stresses per unit thickness can then be calculated as:

$$\begin{aligned}\delta L_{int} &= \int_a^{a+\delta a} dx \int_0^1 \sigma\left(x,\eta\right)\Delta u\left(x\right)\delta\eta \\ &= \frac{1}{2}\int_a^{a+\delta a} dx \sigma_+\left(x\right)\Delta u\left(x\right)\end{aligned} \tag{1.39}$$

Note that, under the assumption of infinitely short range adhesive forces, for a linear elastic isotropic material the asymptotic stress and displacement fields for $x \in [a, a+\delta a]$ are

$$\begin{aligned}\sigma_+(x) &= \frac{K_I}{\sqrt{2\pi\left(x-a-\delta a\right)}} \\ \Delta u\left(x\right) &= K_I/E^*\sqrt{8/\pi(x-a)}\end{aligned} \tag{1.40}$$

where $E^* = E/(1-\nu^2)$ in plane strain and $E^* = E$ in plane stress. In Eq. (1.39), the local process that describes the change of the asymptotic displacement field has been specified by enforcing its specific η-dependence. However, since the behavior of a purely elastic material is conservative, choosing any other path [i.e., any other form of $\delta u\,(x,\eta)$] would lead to the same result. Indeed, in this case the internal work is simply the variation of elastic energy between the two configurations, i.e., $\delta L_{int} = U_{el}(a+\delta a) - U_{el}(a)$. Therefore, substituting Eq. (1.40) into Eq. (1.39) leads to:

$$\left.\frac{\delta L_{int}}{\delta a}\right|_{\delta} = \left.\frac{\partial U_{el}}{\partial a}\right|_{\delta} = \frac{K_I^2}{2E^*} \tag{1.41}$$

which represents the standard expression of the energy release rate, derived for the first time by Irwin [91] and often exploited in contact mechanics [37,90]. Notably, in writing Eq. (1.39) the only assumption made on the material's rheological behavior is linearity. Indeed, importantly, this expression is formally identical to the one that we derive for viscoelastic materials in steady-state sliding contacts (Chapter 3), unsteady contacts (Chapter 4) and crack propagation (Chapter 5). Similarly to the present discussion, in each of the following chapters, the expression of the (virtual) work of internal stresses is derived by applying the virtual work formalism within the proper physical and mathematical framework of each crack or contact problem. However, Eq. (1.41) is valid only for purely elastic materials. Indeed, in order to express the internal work as variation of elastic energy, the response matrix of the system must be symmetric, otherwise, path-dependent work contributions must be considered. The next section delves deeper into this concept.

1.4.2 The elastic energy and the non-integrable part of the work

In order to provide a physical framework to elucidate how the conservative or non-conservative nature of a system is releated to its rheological behavior, we consider the simple example shown in Fig. 1.5 where the free boundary of a constrained deformable linear solid, is loaded with two forces F_1 and F_2. The resulting displacement u_1 and u_2 are given by $F_i = K_{ij}u_j$ (we use the Einstein notation for the repeated index), where K_{ij} is the generic response matrix, which we assume to be asymmetric. Notably, $K_{ij} = K_{ij}^{\mathrm{E}} + K_{ij}^{\mathrm{O}}$ with $K_{ij}^{\mathrm{E}} = \frac{1}{2}(K_{ij} + K_{ij}^T)$ and $K_{ij}^{\mathrm{O}} = \frac{1}{2}(K_{ij} - K_{ij}^T)$ being the symmetric and anti-symmetric parts of K_{ij} respectively. In this case, the work done by F_1 and F_2 can be written as $\delta L = F_i\delta u_i = K_{ij}^{\mathrm{E}}u_j\delta u_i + K_{ij}^{\mathrm{O}}u_j\delta u_i$, with δu_i being the point displacements infinitesimal changes. With this regard, we observe that the symmetry of K_{ij}^{E} implies that $K_{ij}^{\mathrm{E}}u_j\delta u_i = K_{ij}^{\mathrm{E}}u_i\delta u_j$, and $K_{ij}^{\mathrm{E}}u_j\delta u_i = \delta\left(\frac{1}{2}K_{ij}^{\mathrm{E}}u_iu_j\right)$. Thus, $K_{ij}^{\mathrm{E}}u_j\delta u_i = \delta U$ is a conservative term, i.e. the change of the elastic energy $U = \frac{1}{2}K_{ij}^{\mathrm{E}}u_iu_j$. Similarly, since K_{ij}^{O} is anti-symmetric, we have that $K_{ij}^{\mathrm{O}}u_j\delta u_i = -K_{ij}^{\mathrm{O}}u_i\delta u_j$, and $K_{ij}^{\mathrm{O}}u_j\delta u_i = \frac{1}{2}K_{ij}^{\mathrm{O}}\left(u_j\delta u_i - u_i\delta u_j\right)$ which cannot be derived by a potential energy. Therefore, the quantity

$$\delta L_{\mathrm{P}} = K_{ij}^{\mathrm{O}}u_j\delta u_i \tag{1.42}$$

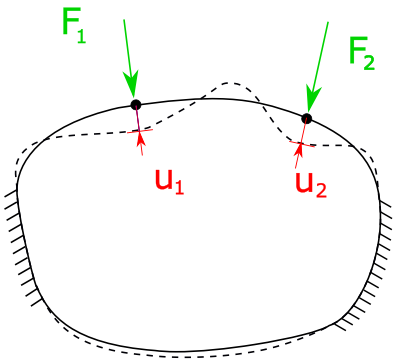

Figure 1.5: A constrained deformable solid, whose response matrix is non-symmetric, loaded with two surface forces. Red arrows refer to displacements (u_1 and u_2), green arrows refer to forces (F_1 and F_2).

is a non-conservative path-dependent contribution to δL. Moreover, since $K^{\mathrm{O}}_{ij}u_j u_i = -K^{\mathrm{O}}_{ij}u_i u_j = 0$, the potential energy U can also be rewritten as

$$U = \frac{1}{2}\left(K^{\mathrm{E}}_{ij} + K^{\mathrm{O}}_{ij}\right) u_j u_i = \frac{1}{2} F_i u_i \tag{1.43}$$

and

$$\delta L = \delta U + \delta L_{\mathrm{P}} \tag{1.44}$$

Now we consider the application of the two forces at the points 1 and 2, as shown in Fig.1.6. Within path I, the force applied at the point 1 is first slowly increased (i.e., through a quasi-static transformation) from zero to a final value F_1, whereas the force at the point 2 remains equal to zero. According to linearity, the work done by the force moving from the configuration (a) to (b) is $L_{\mathrm{ab}} = \frac{1}{2}u_{11}F_1$, being u_{11} the displacement of the point 1 in the direction of F_1 in the state (b). Then, moving from (b) to (d), the force applied at the point 2 is slowly increased from zero to a final value F_2, while the force F_1 is held constant. At the state (d) the value of the displacements of the points 1 and 2, in the direction of F_1 and F_2, are respectively u_1 and u_2. Within the latter process, the work done by F_2 can be calculated by relying on linearity, whereas the work done by the constant force F_1 is simply obtained by multiplying F_1 by the relative displacement of point 1 during the process, so that the overall work from (b) to (d) is $L_{\mathrm{bd}} = \frac{1}{2}(u_2 - u_{21})F_2 + (u_1 - u_{11})F_1$, being u_{21} the displacement of the point 2 in the configuration (b). Regarding the path II, the forces are applied with reverse order. At the intermediate state (c), in which only F_2 is applied, the displacement of the point 1 is u_{12}, whereas the displacement of the point 2 is u_{22}. Observing that linearity entails $u_1 = u_{11} + u_{12}$ and $u_2 = u_{21} + u_{22}$ we can compare the overall work within the two paths:

$$\begin{aligned} L_{\mathrm{I}} &= L_{\mathrm{ab}} + L_{\mathrm{bd}} = \frac{1}{2}u_{11}F_1 + \frac{1}{2}u_{22}F_2 + u_{12}F_1 \\ L_{\mathrm{II}} &= L_{\mathrm{ac}} + L_{\mathrm{cd}} = \frac{1}{2}u_{22}F_2 + \frac{1}{2}u_{11}F_1 + u_{21}F_2 \end{aligned} \tag{1.45}$$

The system is conservative only if $L_{\mathrm{I}} = L_{\mathrm{II}}$, i.e. $u_{12}F_1 = u_{21}F_2$. This only occurs if the system's response matrix is symmetrical and can be easily shown expressing F_1 and F_2 in terms of the displacements in configurations (b) and (c) respectively and in terms of K_{ij}:

$$\begin{aligned} u_{12}F_1 &= K_{11}u_{12}u_{11} + K_{12}u_{12}u_{21} \\ u_{21}F_2 &= K_{21}u_{21}u_{12} + K_{22}u_{21}u_{22} \end{aligned} \tag{1.46}$$

Moreover, observing the configuration (c), we have $F_1 = K_{11}u_{12} + K_{12}u_{22} = 0$ and similarly in configuration (b) $F_2 = K_{22}u_{21} + K_{21}u_{11} = 0$. Solving for the quantities $K_{11}u_{12} = -K_{12}u_{22}$ and $K_{22}u_{21} = -K_{21}u_{11}$ and replacing in Eq. (1.46) we conclude that the system behaves conservatively if and only if $K_{12} = K_{21}$.

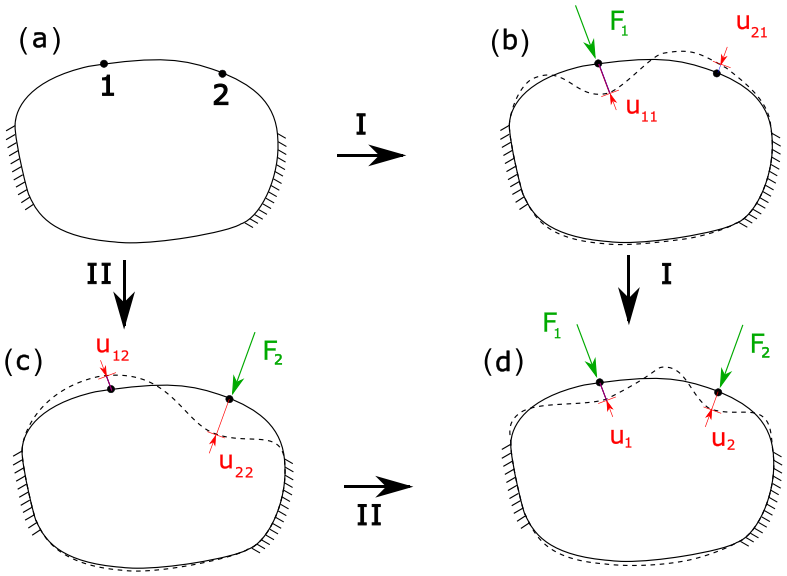

Figure 1.6: Application of two forces at the free boundary of a constrained linear solid with reverse order. Green arrows and red arrows refer, respectively, to forces and displacements. The work done by the forces is path-independent only when the system response matrix is symmetrical.

We consider now a quasi static change of the two displacements over a generic path $\mathcal{L}$ between two states, 0 and 1 in the (u_1, u_2) plane [Fig. 1.7 (a)]. We aim at finding a geometrical interpretation for the non-conservative work L_{P}. Let us use polar coordinates: $u_1 = r(\theta)\cos\theta$ and $u_2 = r(\theta)\sin\theta$. Observe that, according to Eq. (1.42) and using $K^{\mathrm{O}}_{12} = -K^{\mathrm{O}}_{21}$, the elementary non-conservative work is $\delta L_{\mathrm{P}} = K^{\mathrm{O}}_{21}(u_1\delta u_2 - u_2\delta u_1)$. Recalling that $u_1\delta u_2 - u_2\delta u_1 = r^2\delta\theta$, the non-conservative work over the over the whole path is:

$$L_{\mathrm{P}} = \int_{\mathcal{L}} \delta L_{\mathrm{P}} = K^{\mathrm{O}}_{21}\int_{\theta_0}^{\theta_1} r^2\delta\theta = 2K^{\mathrm{O}}_{21}A_{\mathcal{L}} \tag{1.47}$$

Where $A_{\mathcal{L}}$ is the area of the sector limited by the curve $\mathcal{L}$ and the two straight lines $\theta = \theta_0$ and $\theta = \theta_1$ [Fig. 1.7 (a)]. If we now consider the inverse process over the

same path, the work L_{P} inverts its sign. Also note that when $\mathcal{L}$ lies on a straight line through the origin of the plane the non-conservative term is zero. Moreover, considering cyclic processes, if K_{ij} is non-symmetrical the work done by the two forces over the cycle equates the non-conservative work and is thus proportional to the area $A_{\mathcal{L}_{\mathrm{C}}}$ of the cycle [Fig. 1.7 (b)] comprised by the closed curve $\mathcal{L}_{\mathrm{C}}$. If the the cycle is inverted, the work changes sign, leading to the conclusion that the non-conservative system might also represent a source of energy for the observer that applies the forces.

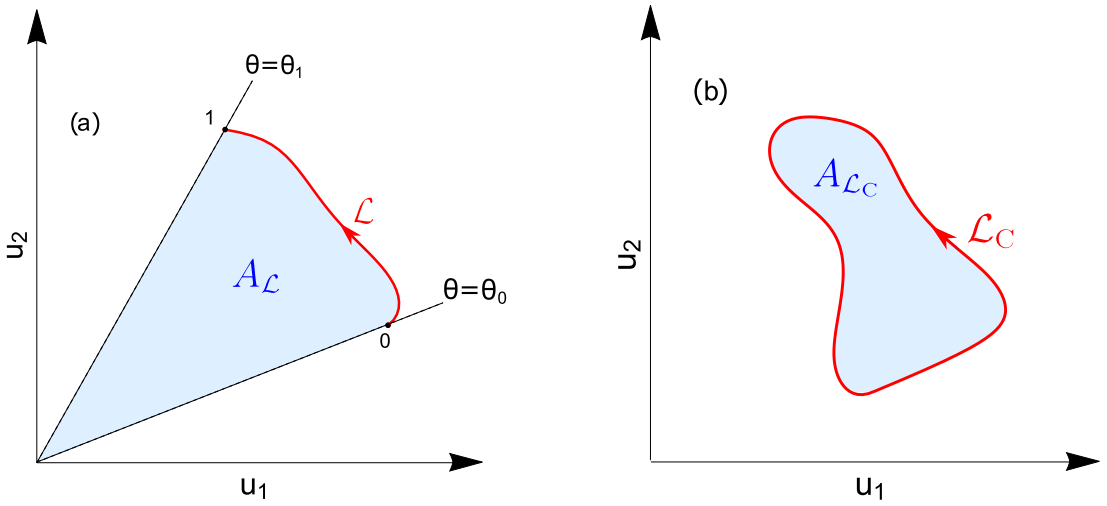

Figure 1.7: (a) In the (u_1, u_2) plane the non-conservative contribution to the work is proportional to the area of the blue sector $A_{\mathcal{L}}$. (b) In cyclic processes the overall work is proportional to the area $A_{\mathcal{L}_{\mathrm{C}}}$ comprised by the closed curve and might be both positive or negative, depending on the direction the cycle is followed.

This mathematical framework can be extended to continuum mechanics: in this case, the conservative or non-conservative nature of the system depends on the symmetry properties of the Green's function. We consider the general case in which, under the assumptions of linearity and translational invariance, the relation between the normal stress and displacement fields on the surface of a solid can be expressed as:

$$u(\mathbf{x}) = \int d^2\mathbf{x}_1 \mathcal{G}(\mathbf{x} - \mathbf{x}_1)\sigma(\mathbf{x}_1) \tag{1.48}$$

Where we assume that the Green's function $\mathcal{G}(\mathbf{x})$ is a non-symmetric function and therefore can be decomposed into its even (symmetric) and its odd (anti-symmetric) parts:

$$\mathcal{G}(\mathbf{x}) = \mathcal{G}^{\mathrm{E}}(\mathbf{x}) + \mathcal{G}^{\mathrm{O}}(\mathbf{x}) \tag{1.49}$$

being $\mathcal{G}^{E}(\mathbf{x}) = \frac{1}{2}\left(\mathcal{G}(\mathbf{x}) + \mathcal{G}(-\mathbf{x})\right)$ and $\mathcal{G}_V^{O}(\mathbf{x}) = \frac{1}{2}\left(\mathcal{G}(\mathbf{x}) - \mathcal{G}(-\mathbf{x})\right)$. Notably, this framework describes the steady-state sliding contact between a viscoelastic fundation and a rigid indenter: assuming a reference frame co-moving with the indenter the time-dependecy of the moving fields is masked and the viscoelastic Green's

function in Eq. (1.48) is a non-symmetric function, parametrically depending on the sliding velocity. The reader is referred to Chapter 2 for a detailed discussion on the viscoelastic Green's functions.
Let us calculate the work δL done by the stress field $\sigma(\mathbf{x})$ over a quasi-static variation $\delta u(\mathbf{x})$ of the displacements field. Since Eq. (1.48) implies that $\delta u(\mathbf{x}) = \int d^2\mathbf{x}_1 \mathcal{G}(\mathbf{x}-\mathbf{x}_1)\delta\sigma(\mathbf{x}_1)$, we obtain

$$\delta L = \int d^2x\sigma(\mathbf{x})\delta u(\mathbf{x}) \tag{1.50}$$

$$= \int d^2\mathbf{x}d^2\mathbf{x}_1\mathcal{G}(\mathbf{x}-\mathbf{x}_1)\sigma(\mathbf{x})\delta\sigma(\mathbf{x}_1) \tag{1.51}$$

and substituting (1.49) into (1.50) yields:

$$\delta L = \int d^2\mathbf{x}d^2\mathbf{x}_1\mathcal{G}^{\mathrm{E}}(\mathbf{x}-\mathbf{x}_1)\sigma(\mathbf{x})\delta\sigma(\mathbf{x}_1) + \int d^2\mathbf{x}d^2\mathbf{x}_1\mathcal{G}^{\mathrm{O}}(\mathbf{x}-\mathbf{x}_1)\sigma(\mathbf{x})\delta\sigma(\mathbf{x}_1)$$

Moreover, we notice that, similarly to the discrete case, we can write

$$\int d^2\mathbf{x}d^2\mathbf{x}_1\mathcal{G}^{\mathrm{E}}(\mathbf{x}-\mathbf{x}_1)\sigma(\mathbf{x})\delta\sigma(\mathbf{x}_1) = \int d^2\mathbf{x}d^2\mathbf{x}_1\mathcal{G}^{\mathrm{E}}(\mathbf{x}-\mathbf{x}_1)\sigma(\mathbf{x}_1)\delta\sigma(\mathbf{x})$$

And therefore we get:

$$\int d^2\mathbf{x}d^2\mathbf{x}_1\mathcal{G}^{\mathrm{E}}(\mathbf{x}-\mathbf{x}_1)\sigma(\mathbf{x})\delta\sigma(\mathbf{x}_1) = \delta\left(\frac{1}{2}\int d^2xd^2x_1\mathcal{G}^{\mathrm{E}}(\mathbf{x}-\mathbf{x}_1)\sigma(\mathbf{x})\sigma(\mathbf{x}_1)\right)$$

We conclude that the latter is a conservative contribution, hence the overall work can be expressed as

$$\delta L = \delta U + \delta L_{\mathrm{P}} \tag{1.52}$$

where the elastic energy is

$$U = \frac{1}{2}\int d^2xd^2x_1\mathcal{G}^{\mathrm{E}}(\mathbf{x}-\mathbf{x}_1)\sigma(\mathbf{x})\sigma(\mathbf{x}_1) \tag{1.53}$$

$$= \frac{1}{2}\int d^2x\sigma\left(\mathbf{x}\right)u\left(\mathbf{x}\right)$$

and the non conservative contribution is

$$\delta L_{\mathrm{P}} = \int d^2xd^2x_1\mathcal{G}^{\mathrm{O}}(\mathbf{x}-\mathbf{x}_1)\sigma(\mathbf{x})\delta\sigma(\mathbf{x}_1) \tag{1.54}$$

$$= \frac{1}{2}\int d^2xd^2x_1\mathcal{G}^{\mathrm{O}}(\mathbf{x}-\mathbf{x}_1)\left[\sigma\left(\mathbf{x}\right)\delta\sigma\left(\mathbf{x}_1\right)-\delta\sigma\left(\mathbf{x}\right)\sigma\left(\mathbf{x}_1\right)\right]$$

For purely elastic materials the Green's function is symmetric (see, for instance, [47]), so that $\delta L_{\mathrm{P}} = 0$. Not let us identify some other particular cases yielding

$\delta L_{\mathrm{P}} = 0$. Consider a perturbation of the displacements fields $u(\mathbf{x})$, which keeps its shape unchanged, i.e. $u(\mathbf{x}) = u_0(\mathbf{x})\eta$ and $\delta u(\mathbf{x}) = u_0(\mathbf{x})\delta\eta$, where η is a dimensionless parameter governing the process. In this case, linearity yields $\sigma(\mathbf{x}) = \sigma_0(\mathbf{x})\eta$ and $\delta\sigma(\mathbf{x}) = \sigma_0(\mathbf{x})\delta\eta$, where $u_0(\mathbf{x})$ and $\sigma_0(\mathbf{x})$ are related through Eq. (1.48). Thus, refferring to Eq. (1.54), we have $\sigma(\mathbf{x})\,\delta\sigma(\mathbf{x}_1) = \sigma_0(\mathbf{x})\,\sigma_0(\mathbf{x}_1)\,\eta\delta\eta = \delta\sigma(\mathbf{x})\,\sigma(\mathbf{x}_1)$ leading to $\delta L_{\mathrm{P}} = 0$. This arguments applies of course to the case of a concentrated load $\sigma(\mathbf{x}) = \eta\delta_D(\mathbf{x} - \mathbf{x}_0)$, being $\delta_D(\mathbf{x})$ the Dirac delta function. Indeed, we get $\sigma(\mathbf{x})\,\delta\sigma(\mathbf{x}_1) = \delta_D(\mathbf{x}-\mathbf{x}_0)\delta_D(\mathbf{x}_1-\mathbf{x}_0)\eta\delta\eta = \delta\sigma(\mathbf{x})\,\sigma(\mathbf{x}_1)$ leading again to $\delta L_{\mathrm{P}} = 0$. Analogously to the discrete case, δL_{P} might be either positive or negative, hence an external observer could extract work by deforming the surface of the system through cyclic processes. This is simply explained by noting that the observer that applies the forces only has information about the mechanical response on the system's surface, while additional energy exchanges might occur elsewhere. For instance, if Eq. (1.48) describes the response of the surface of a viscoelastic foundation sliding under steady-state conditions, an additional energy source is required to sustain the sliding motion. Therefore, although the observer modifying the surface displacement field might cyclically extract work, a larger amount of work must be supplied through a lateral force to ensure that the sliding velocity is held constant, compensating for the internal viscoelastic losses. This means that, in this type of systems, the quantity δL_{P} does not quantify the viscoelastic dissipation of energy. This is a fundamental observation for the subsequent chapters.

Chapter 2

Concepts of linear viscoelasticity

Over the last two decades, rubbery-like materials have been increasingly utilized in a wide range of engineering applications. In addition to classical applications such as tires, dampers, seals, and belts, they are nowadays widely employed in innovative contexts, such as micro-electromechanical systems, protective films, thin gloves and suits, and bio-inspired mimicking skins. Their excellent mechanical and chemical properties, including resilience, durability, and elasticity, have significantly boosted scientific interest in this class of materials. However, the smart design of these systems requires a detailed understanding of the intrinsic viscoelastic response of rubbery-like materials.

The mechanical behavior of viscoelastic materials is intermediate between an elastic solid and a Newtonian fluid. In the theory of linear elasticity, a deformation field is uniquely determined by the instantaneous value of the stress field; in other words, the material has no memory of the loading history, and its response is not influenced by the rate at which the stress or the deformation is applied. On the other hand, for a Newtonian fluid, the shear stresses is proportional to the time derivative of the deformation. A viscoelastic material, when subjected to a certain constant stress, initially responds like a elastic material with an instantaneous deformation. Over time, the deformation gradually increases (i.e., similarly to the Newtonian fluid response) until a plateau is reached. Overall, the mechanical behavior is largely hysteretic due to the internal friction among polymeric chains: the energy provided to deform the material is partially stored in the elastic deformations of the polymeric chains and partially dissipated. This is a pivotal aspect from the engineering perspective, as the amount of internal dissipation should be properly designed, e.g., in applications like dampers or tire-road friction.

In this chapter, we present a brief overview of the rheological behavior of viscoelastic materials. In the first section, we describe commonly employed general rheological models. In the second section, we present the Green's function approach. This can be exploited to formulate the stress-displacement problem on the surface of a viscoelastic half-space or layer, and will be widely employed in the subsequent chapters.

2.1 General aspects

The linear viscoelasticity is the rheological behavior of a solid whose linear response depends on the entire time-history of applied stresses or strains and presents an intermediate behavior between a Newtonian viscous fluid and a purely elastic solid. In general, the constitutive relation between the time-dependent stress and the time-dependent deformation for a viscoelastic material is expressed by a linear operator:

$$\sigma(t) = \mathcal{L}[\varepsilon(t)] \tag{2.1}$$

Of course, the linearity of $\mathcal{L}$ reads as:

$$\mathcal{L}[c_1\varepsilon(t)_1 + c_2\varepsilon(t)_2] = c_1\mathcal{L}\left[\varepsilon(t)_1\right] + c_2\mathcal{L}\left[\varepsilon(t)_2\right]$$

where c_1, c_2 are real constants and $\varepsilon(t)_1, \varepsilon(t)_2$ are two different arbitrary input time-histories. The constitutive relation also possesses the causality and time-invariance properties. In a causal system the output depends on past events and is not affected by the future. The time invariance property instead expresses that a time-shifting of the input entails the same time-shifting of the output. Eq. (2.1) represents the stress as "output" generated by a certain deformation as "input" but the inverse relation has the same properties. A linear system that obeys the causality and time-invariance requirements is completely characterized by its response to the Heaviside unit-step input. Indeed, Eq. (2.1) is usually written as:

$$\sigma(t) = \int_{-\infty}^{t} dt_1 R(t - t_1)\dot{\varepsilon}(t_1) \tag{2.2}$$

or in the equivalent form obtained by applying the by part integration:

$$\sigma(t) = R(0^+)\varepsilon(t) + \int_{-\infty}^{t} dt_1 \dot{R}(t - t_1)\varepsilon(t_1)$$

In these expressions, $R(t)$ is called the viscoelastic relaxation function and is the time-dependent stress obtained in response to $\varepsilon(t) = \mathcal{H}(t)$, being $\mathcal{H}(t)$ the unit-step function. Analogue expressions are

$$\varepsilon(t) = \int_{-\infty}^{t} dt_1 J(t - t_1)\dot{\sigma}(t_1) \tag{2.3}$$

$$\varepsilon(t) = J(0^+)\sigma(t) + \int_{-\infty}^{t} dt_1 \dot{J}(t - t_1)\sigma(t_1)$$

where $J(t)$ is called viscoelastic creep's function and is the deformation recovered when $\sigma(t) = \mathcal{H}(t)$. Observe that the system's causality implies that $R(t < 0) = 0$ and $J(t < 0) = 0$. $R(t)$ and $J(t)$ are usually derived from schematic representations consisting of springs and dampers, as those shown in Fig. 2.1. In Fig. 2.1 (a), each of the elements consisting of a spring and a damper connected in series is called Maxwell element. In this case, the relation between stress and deformation can be

derived more simply when stress is expressed as a function of strain. Indeed, the total stress is the sum of the stresses acting on each element, and all the elements are subjected to the same deformation. Note that the relaxation function $R_i(t)$ of the i-th maxwell element, i.e., its response to a step-function deformation, is obtained as the solution of the differential equation

$$\frac{R_i(t)}{\tau_i E_i} + \frac{\dot{R}_i(t)}{E_i} = \dot{\mathcal{H}}(t) = \delta(t) \tag{2.4}$$

where $\delta(t)$ is the Dirac Delta and τ_i is the ratio between the damping coefficient and the stiffness of each element and is called relaxation time of the element. The solution of Eq. (2.4) is

$$R_i(t) = E_i \exp(-t/\tau)\mathcal{H}(t)$$

and, in turn, the overall relaxation function is:

$$R(t) = \left[E_0 + \sum_{i=1}^{N} E_i \exp(-t/\tau)\right] \mathcal{H}(t) \tag{2.5}$$

where also the contribution of the spring element of stiffness E_0 has been considered. Notably, for $t \to 0^+$, the material response resembles that of an elastic stiff material whose modulus is $R(0^+) = E_0 + \sum_i E_i = E_\infty$. Then, after a long time, the effective stiffness $E(t) = \sigma(t)/\varepsilon(t)$ decreases to the value E_0. Note that introducing the spring E_0 is necessary to correctly model a viscoelastic material, otherwise a constant stress would lead to a monotonically increasing deformation, i.e., the material would (almost) behave like a Newtonian fluid.
On the other hand, the general model shown in Fig. 2.1 (b), allows a simpler analysis when the strain is expressed as function of the stress. The overall strain is indeed the sum of the strains of all the i-th Voigt models, each composed of a damper and a spring connected in parallel. The creep function $J_i(t)$ of each element is the solution of the differential equation:

$$\dot{J}_i(t)\tau E_i + J_i(t)E_i = \mathcal{H}(t)$$

Therefore:

$$J_i(t) = \frac{1}{E_i}\left[1 - \exp(-t/\tau)\right]\mathcal{H}(t)$$

and the overall creep function is

$$J(t) = \left\{\frac{1}{E_\infty} + \sum_{i=1}^{N} \frac{1}{E_i}\left[1 - \exp[-t/\tau]\right]\right\} \mathcal{H}(t) \tag{2.6}$$

Observe that introducing the spring of stiffness E_∞ is necessary, otherwise, one would obtain $J(0^+) = 0$, which does not represent the real behavior of a viscoelastic material. Up to this point we have considered a single component of stress and deformation, i.e., we analyzed an uniaxial loading case. In the general case, the internal stress tensor and the deformation tensor are related each other as

$$\sigma_{ij}(t) = \int dt_1 R_{ijkl}(t - t_1)\dot{\varepsilon}_{kl}(t_1)$$

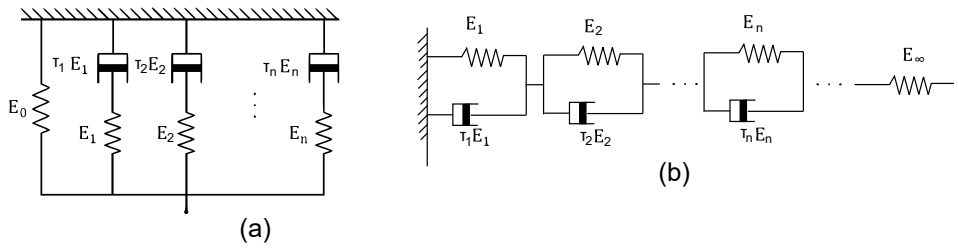

Figure 2.1: General models for linear viscoelasticity. (a) The generalized Maxwell model. (b) The generalized Voigt model

in which the previous arguments apply to the single components of R_{ijkl} (see [104]). Observe now that, since we are considering a linear system, its mechanical behavior can be fully characterized by its response to a sinusoidal input. Hence, we take the Fourier transform of Eqs. (2.3,2.2) and proceed with our analysis in the frequency domain

$$\begin{aligned} \sigma(\omega) &= i\omega R(\omega)\varepsilon(\omega) \\ \varepsilon(\omega) &= i\omega J(\omega)\sigma(\omega) \end{aligned} \tag{2.7}$$

Eqs. (2.7) show that the creep function and the relaxation function in the Fourier domain must satisfy

$$-\omega^2 J(\omega)R(\omega) = 1 \tag{2.8}$$

This means that, since $R(t)$ and $J(t)$ describe the same material, the rheological constants appearing in Eq. (2.5) are not independent on those appearing in Eq. (2.6). E.g., in the case in which the material's behavior is described by a single relaxation time, $R(t)$ and $J(t)$ satisfy Eq. (2.8) as long as the relaxation times of the two functions scale of a factor E_∞/E_0. Now, we define the complex modulus as $E(\omega) = [i\omega J(\omega)]^{-1}$. Observe that taking the Fourier transform of Eq. (2.6) leads to

$$\frac{1}{E(\omega)} = \frac{1}{E_\infty} + \sum_{i=1}^{N} \frac{1}{E_i} \frac{1}{1 + i\omega\tau_i} \tag{2.9}$$

The complex modulus, and in particular the so-called loss tangent $\mathrm{Im}[E(\omega)]/\,\mathrm{Re}[E(\omega)]$, play a fundamental role in determining the frictional behavior of viscoelastic materials in sliding and rolling contacts (see Chapter 3). Typical forms of these functions are plotted in Fig. 2.2. Observe that, according to Eq.2.9, we have $E(\omega \to 0) = E_0$ and $E(\omega \to +\infty) = E_\infty$, which are usually referred to as low- and high- frequency modulus, respectively. This means that, when excited at very low frequency, the material behaves as a soft elastic solid with modulus E_0. This regime of excitation is usually referred to as rubbery region. Instead, at very high frequency of excitation, the material behaves again elastically, but with a way much stiffer response described by the modulus E_∞. This regime is usually referred to as glassy regime. The most peculiar behavior of a viscoelastic material is recovered at intermediate frequencies of excitation, in which the material's response is highly hysteretic and the loss tangent takes its maximum. Note that Eqs.

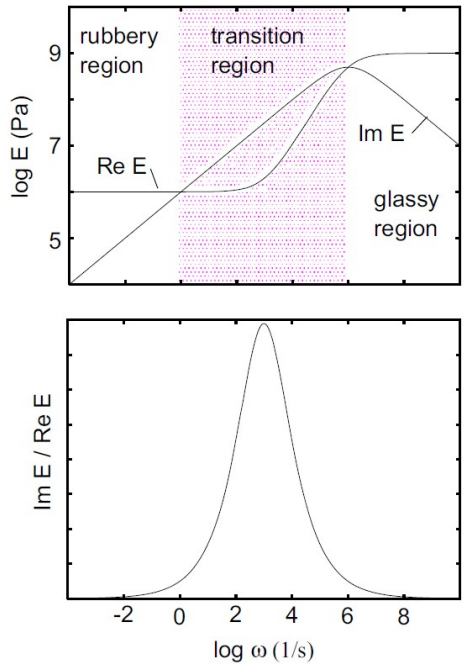

Figure 2.2: (a) The real and imaginary parts of the complex modulus $E(\omega)$ as function of the exciting frequency. (b) The loss tangent $Im[E(\omega)]/Re[E(\omega)]$ as function of the exciting frequency

(2.7, 2.9) imply that when the material is subjected to an oscillating sinusoidal loading, a phase between stress and deformation occurs. Therefore, the work of internal stresses $L = \int_T \sigma(t)\dot{\varepsilon}(t)dt$ doesn't vanish over the period T. This means that when a viscoelastic material is subjected to cyclic deformations whose main frequency contributions correspond to the transition region shown in the figure, a certain amount of work must be spent. Indeed, in sliding contacts between rough surfaces and in rolling contacts, this eventually leads to a lateral force opposing the relative motion, usually referred to as viscoelastic friction [25]. Importantly, the maximum amount of dissipation occurs when the loss tangent is maximized for a given frequency of excitation (see [103]).

2.2 The viscoelastic Green's functions

2.2.1 General unsteady case

We consider the surface of a linear viscoelastic half-space. Under the condition of translational invariance (i.e., the system is homogeneous) and linearity, the relation between the interfacial normal stresses $\sigma(\mathbf{x}, t)$ and the surface normal

displacements $u(\mathbf{x},t)$ can be written as a convolution product, i.e.

$$u(\mathbf{x},t) = \int d^2x_1 dt_1 G(\mathbf{x}-\mathbf{x}_1, t-t_1)\,\sigma(\mathbf{x}_1,t_1) \tag{2.10}$$

where $\mathbf{x}$ is the in-plane position vector. Taking the time and space Fourier transform of Eq. (2.10) one obtains

$$u(\mathbf{q},\omega) = G(\mathbf{q},\omega)\,\sigma(\mathbf{q},\omega) \tag{2.11}$$

where the wave vector is $\mathbf{q}$ and ω is the angular frequency, and $G(\mathbf{q},\omega)$ is the response function. The specific form of the response function $G(\mathbf{q},\omega)$ depends on the system geometry, on the material properties, and on how the system is constrained. Dimensional arguments (see Ref. [102]) show that $G(\mathbf{q},\omega)$ must have the following general form

$$G(\mathbf{q},\omega) = -\frac{2(1-\nu^2)}{E(\omega)}\frac{1}{|\mathbf{q}|}S(|\mathbf{q}|,\omega) \tag{2.12}$$

where the term $S(\mathbf{q},\omega)$ is a corrective factor that in the case of homogeneous half space is equal to 1 and $E(\omega)$ is the viscoelastic complex modulus. The corrective factor $S(\mathbf{q},\omega)$ has been found for different geometries and different boundary conditions as well as for and also for layered materials (Ref. [30, 47, 102, 103]). Notably, Eq. (2.12) is a general result that follows from the so called elastic-viscoelastic correspondence principle. The latter arises from the observation that the equations of the linear viscoelastic boundary value problem once expressed in the Fourier domain take the same form of the equations of the corresponding linear elastic problem, as long as the region in which boundary conditions are specified do not change over time. Therefore, the viscoelastic solutions in the ω-Fourier domain have the same form of the corresponding elastic ones, provided that the elastic moduli are replaced by the Fourier-transformed viscoelastic ones. Of course when we consider the application of a concentrated load (i.e., when we analyze the Green's function of the system), the region in which boundary conditions are specified do not change over time and the correspondence applies. The reader is referred to [104] for additional details on the correspondence principle. Now we can notice that, the meaning of Eq. (2.12) is that, when $S(|\mathbf{q}|,\omega)$ is ω-independent (as for a confined or free layer, see the next section) the viscoelastic Green's function $G(\mathbf{x},t)$ in the time and space domain is factorized as

$$G(\mathbf{x},t) = \dot{J}(t)\mathcal{G}(\mathbf{x}) \tag{2.13}$$

where

$$\mathcal{G}(\mathbf{x}) = -\frac{2(1-\nu^2)}{(2\pi)^2}\int dq^2 \frac{S(qd)}{|q|}e^{i\mathbf{q}\cdot\mathbf{x}}$$

and $J(t)$ is the viscoelastic creep's function. Note that, in agreement with the correspondence principle, $\mathcal{G}(\mathbf{x})$ is the Green's function of the corresponding elastic case for a material of unitary modulus. E.g., for the half-space case we get $\mathcal{G}(\mathbf{x}) =$

$2\left(1-\nu^2\right)/\left|\mathbf{x}\right|$, in agreement with the Bussinesq solution. Now observe that, using Eq. (2.13), Eq. (2.10) can be rewritten as

$$u\left(\mathbf{x},t\right)=\int_{-\infty}^{t}dt_1 J(t-t_1)\int d^2x_1\mathcal{G}(\mathbf{x}-\mathbf{x}_1)\dot{\sigma}\left(\mathbf{x}_1,t_1\right) \tag{2.14}$$

or in the equivalent form:

$$u\left(\mathbf{x},t\right)=J(0^+)\int d^2x_1\mathcal{G}(\mathbf{x}-\mathbf{x}_1)\sigma\left(\mathbf{x}_1,t\right)+\int_{-\infty}^{t}dt_1\dot{J}(t-t_1)\int d^2x_1\mathcal{G}(\mathbf{x}-\mathbf{x}_1)\sigma\left(\mathbf{x}_1,t_1\right)$$

2.2.2 1D+1D periodic steady case

A case of interest for the present thesis is the 1D+1D periodic contact in steady-state sliding conditions. In order to apply the elastic-viscoelastic correspondence principle and derive the viscoelastic Green's function for this problem, we start our discussion from the equivalent elastic problem. We consider the two configurations shown in Fig. 2.3: a thick slab of thickness d sandwiched between a flat rigid plate (upper part) and a rough substrate (bottom part), as shown in Fig. 2.3(a), and a thick slab is subjected to a uniform applied pressure (Fig. 2.3(b)). We focus on periodic problems of wavelength λ. Following [47], we define the interfacial displacement field $v(x)=u(x)-u_{\mathrm{m}}$ (note that u_{m} is the mean displacement of the deformed surface), related to the stress distribution $\sigma(x)$ as

$$v(x)=\int_{-\lambda/2}^{\lambda/2}dx_1\frac{\mathcal{G}_E(x-x_1)}{E}\sigma(x_1) \tag{2.15}$$

where E is the Young modulus and $\mathcal{G}_E(x)/E$ is the elastic Green's function of this specific case, where:

$$\mathcal{G}_E(x)=\frac{2\left(1-\nu^2\right)}{\pi}\left(\sqrt{\log[2-2\cos(kx)]}+\sum_{m=1}^{\infty}A_m(kd)\frac{\cos(mkx)}{m}\right)$$

where $k=2\pi/\lambda$ and

$$A_m(kd)=\frac{2mkd-(3-4\nu)\sinh(2dmk)}{5+2\left(mkd\right)^2-4\nu\left(3-2\nu\right)+(3-4\nu)\cosh\left(2mkd\right)}+1$$

for the confined layer, and

$$A_m(kd)=\frac{2mkd+\sinh(2dmk)}{1+2\left(mkd\right)^2-\cosh\left(2mkd\right)}+1$$

for the free layer. Notably, the quantity $\sum_{m=1}^{\infty}A_m(kd)\cos(mkx)/m$ is a fast-converging series that vanishes in the half-plane case, i.e., for $d\to\infty$. Moreover, the mean displacement u_{m} can be expressed as:

$$u_{\mathrm{m}}=-\frac{1+\nu}{1-\nu}\frac{1-2\nu}{E}\sigma_m d \tag{2.16}$$

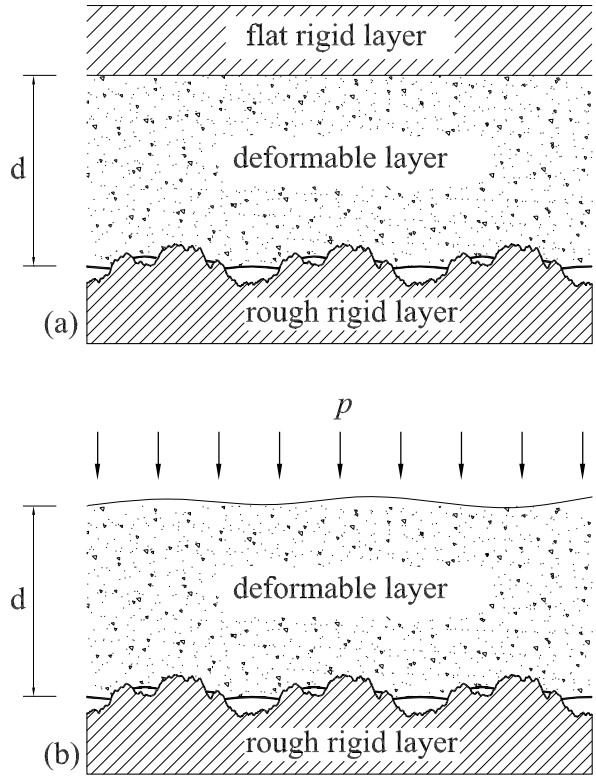

Figure 2.3: A deformable layer of thickness d in contact with a rough substrate. The layer is assumed to be glued to the upper plate (a), or subjected to a uniform pressure p (b).

where $\sigma_m = 1/\lambda \int_{-\lambda/2}^{\lambda/2} \sigma(x)dx$ is the mean stress (equal to σ_∞ in the case of free layer). Observe that in the half-plane case both u_m and $u(x)$ diverge, unless $\nu = 0.5$. Therefore, formulating the problem on the interfacial displacement $v = u - u_m$ avoids dealing with infinite quantities. Now, let us move to the viscoelastic case. Applying linearity and translational invariance and invoking the elastic-viscoelastic correspondence principle, we can write

$$v\,(x,t) = \int_{-\infty}^{t} dt_1 J(t-t_1) \int_{-\lambda/2}^{\lambda/2} dx_1 \mathcal{G}_E(x-x_1)\dot{\sigma}\,(x_1,t_1) \tag{2.17}$$

Now, assuming steady state sliding motion at velocity v, the moving steady fields can be expressed as $u(x,t) = u(x-vt)$ and $\sigma(x,t) = \sigma(x-vt)$. Then, using the replacement $x \to x + vt$, i.e. changing the reference frame so that the observer moves with velocity v, Eq. (2.17) can be rewritten as

$$v\,(x) = \int_{-\lambda/2}^{\lambda/2} d^2x \mathcal{G}_L^{1D}(x-x_1,v)\sigma\,(x_1)$$

where

$$\mathcal{G}_L^{1D}(x,v) = J(0^+)\mathcal{G}_E(x) + \int_{0^+}^{+\infty} dt \mathcal{G}_E(x+vt)\dot{J}(t)$$

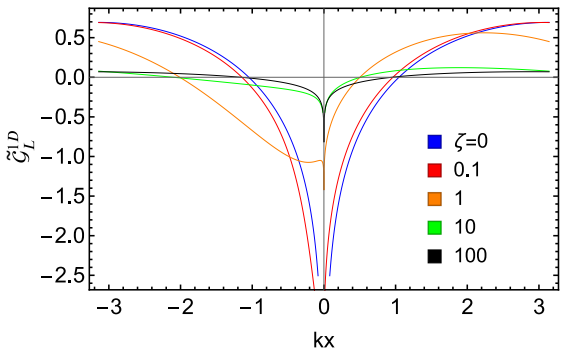

Figure 2.4: The dimensionless periodic Green's function $\tilde{\mathcal{G}}_L^{1D}(x) = \mathcal{G}_L^{1D}(x)\frac{\pi E_0}{2(1-\nu^2)}$ under steady-state sliding conditions shown as function of the dimensionless coordinate kx for different values of the dimensionless sliding velocity $\zeta = kv\tau$. Results are shown for $E_\infty/E_0 = 10$.

is the viscoelastic Green's function for steady-state sliding periodic contacts, parametrically depending on the sliding velocity. In Fig. (2.4) $\mathcal{G}_L^{1D}(x,v)$ is plotted assuming the single relaxation time creep's function

$$J(t) = \left\{ \frac{1}{E_\infty} + \left[\frac{1}{E_0} - \frac{1}{E_\infty} \right] [1 - \exp(-t/\tau)] \right\} \mathcal{H}(t)$$

and different values of the dimensionless velocity $\zeta = kv\tau$. Notably, at very low velocity values viscoelastic effects vanish and the material is fully relaxed, hence $\mathcal{G}_L^{1D}(x,v) = \mathcal{G}_E(x)/E_0$. At intermediate velocity, $\mathcal{G}_L^{1D}(x,v)$ is a non-symmetric function that reflects the viscoelastic relaxation. At very high velocity, the response of the material is in the glassy region and therefore $\mathcal{G}_L^{1D}(x,v) = \mathcal{G}_E(x)/E_\infty$.

2.2.3 Alternative derivation

In what follows we propose an alternative derivation of the Green's function for steady sliding contacts at velocity $\mathbf{v}$. Let us move back to Eq.(2.10) and observe that, under these steady sliding conditions, assuming a reference frame moving with velocity $\mathbf{v}$, it can be rephrased as

$$u(\mathbf{x}) = \int d^2x \mathcal{G}_S(\mathbf{x} - \mathbf{x}', \mathbf{v}) \sigma(\mathbf{x}') \tag{2.18}$$

where the new Green function $\mathcal{G}_S(\mathbf{x}, \mathbf{v})$ parametrically depends on the velocity $\mathbf{v}$. Also observe that in steady sliding any physical quantities f depends on space and time through the relation $f(\mathbf{x}, t) = f(\mathbf{x} - \mathbf{v}t)$. Hence, taking the Fourier transform yields

$$f(\mathbf{q}, \omega) = \int dt d^2x \; f(\mathbf{x} - \mathbf{v}t) \, e^{-i(\mathbf{q}\cdot\mathbf{x} - \omega t)} = 2\pi\delta(\omega - \mathbf{q}\cdot\mathbf{v}) f(\mathbf{q}) \tag{2.19}$$

Then, using Eq. (2.11), and integrating over the frequency real axis gives

$$u\left(\mathbf{q}\right) = G\left(\mathbf{q}, \mathbf{q}\cdot\mathbf{v}\right)\sigma\left(\mathbf{q}\right) \tag{2.20}$$

Taking the inverse Fourier transform, Eq. (2.20) shows that

$$\mathcal{G}_{\mathrm{S}}(\mathbf{x}, \mathbf{v}) = \frac{1}{\left(2\pi\right)^2}\int d^2q G\left(\mathbf{q}, \mathbf{q}\cdot\mathbf{v}\right)e^{i\mathbf{q}\cdot\mathbf{x}} \tag{2.21}$$

We will show now how it is possible, moving from $\mathcal{G}_{\mathrm{S}}(\mathbf{q}, \mathbf{v}) = G\left(\mathbf{q}, \mathbf{q}\cdot\mathbf{v}\right)$ to calculate the Green function for the case of periodic steady sliding contacts, where the relation between the stress and displacement fields at the interface can be written as

$$u\left(\mathbf{x}, t\right) = \int_D d^2x' \mathcal{G}_D\left(\mathbf{x}-\mathbf{x}', \mathbf{v}\right)\sigma\left(\mathbf{x}', t'\right) \tag{2.22}$$

where $\mathcal{G}_D\left(\mathbf{x}, \mathbf{v}\right)$ is the periodic Green function with periodic square cell D of lateral size L. Of course $\mathcal{G}_D\left(\mathbf{x}, \mathbf{v}\right)$ is the interfacial displacement field resulting from a stress distribution of concentrated unit loads distributed on a regular square lattice of elementary cell D. This distribution of forces can be represented by the surface stress field

$$\delta_D\left(\mathbf{x}\right) = \sum_{k,h=-\infty}^{+\infty}\delta\left(\mathbf{x}-\frac{2\pi}{q_0}\mathbf{k}\right) \tag{2.23}$$

where $\delta\left(\mathbf{x}\right)$ is the two-dimensional Dirac delta function and $\mathbf{k} = (k, h)$ is the vectorial wave number. The fundamental frequency is $q_0 = 2\pi/L$. Therefore we get

$$\mathcal{G}_D\left(\mathbf{x}, \mathbf{v}\right) = \int d^2x' \mathcal{G}\left(\mathbf{x}-\mathbf{x}', \mathbf{v}\right)\delta_D\left(\mathbf{x}'\right) = \sum_{k,h=-\infty}^{+\infty}\mathcal{G}\left(\mathbf{x}-\frac{2\pi}{q_0}\mathbf{k}, \mathbf{v}\right) \tag{2.24}$$

Taking the Fourier transform of Eq. (2.24) gives

$$\mathcal{G}_D\left(\mathbf{q}, \mathbf{v}\right) = \sum_{k,h=-\infty}^{+\infty}\int d^2x e^{-i\mathbf{q}\cdot\mathbf{x}}\mathcal{G}\left(\mathbf{x}-\frac{2\pi}{q_0}\mathbf{k}, \mathbf{v}\right) = \sum_{r,s=-\infty}^{+\infty}\mathcal{G}\left(\mathbf{q}, \mathbf{v}\right)\delta\left(\frac{\mathbf{q}}{q_0}-\mathbf{r}\right) \tag{2.25}$$

with $\mathbf{r} = (r, s)$. Moving back to the space domain we have

$$\mathcal{G}_D\left(\mathbf{x}, \mathbf{v}\right) = \frac{1}{\left(2\pi\right)^2}\int d^2q \mathcal{G}_D\left(\mathbf{q}, \mathbf{v}\right)e^{i\mathbf{q}\cdot\mathbf{x}} = \left(\frac{q_0}{2\pi}\right)^2\sum_{r,s=-\infty}^{+\infty}\mathcal{G}\left(q_0\mathbf{r}, \mathbf{v}\right)e^{iq_0\mathbf{r}\cdot\mathbf{x}} \tag{2.26}$$

The procedure just presented so far can easily exploited also for 1D+1D contact problems with spatial periodicity L and fundamental spatial frequency $q_0 = 2\pi/L$. In this case the displacement and stress fields takes the form $u\left(\mathbf{x}\right) = u\left(x\right)$ and $\sigma\left(\mathbf{x}\right) = \sigma\left(x\right)$. The corresponding 2D Fourier transform is

$$u\left(\mathbf{q}\right) = \int dx^2 u\left(x\right)e^{-i\mathbf{q}\cdot\mathbf{x}} = 2\pi\delta\left(q_y\right)u\left(q_x\right) \tag{2.27}$$

and

$$\sigma(\mathbf{q}) = \int dx^2 \sigma(x) e^{-i\mathbf{q}\cdot\mathbf{x}} = 2\pi\delta(q_y)\sigma(q_x) \tag{2.28}$$

Therefore, after integrating over q_y, Eq. (2.20) gives

$$u(q_x) = \mathcal{G}^{1D}(q_x, v)\sigma(q_x) \tag{2.29}$$

where $\mathcal{G}^{1D}(q_x, v) = G(q_x, q_y = 0, q_x v)$, where $v = v_x$. Then, following the same approach leads to

$$\mathcal{G}_L^{1D}(x, v) = \sum_{k=-\infty}^{+\infty} \frac{q_0}{2\pi} \mathcal{G}^{1D}(kq_0, v) e^{ikq_0 x} \tag{2.30}$$

Chapter 3

Adhesion and friction in steady viscoelastic contacts

Experimental evidences clearly indicate that friction in sliding and rolling contacts of rubber-like materials is highly affected by the presence of adhesive interactions at the interface. Nonetheless, most of existing analytical and numerical approaches [25,30,31,43,103,105–109] are only able to describe the adhesiveless viscoelastic contact behavior. In this class of contacts, viscoelastic relaxation strongly affects the key contact quantities, such as the contact size, which are found to depend on the relative velocity. Importantly, the frictional response is ascribable to dissipative phenomena occurring in the bulk of the material, where viscoelasticity entails a certain ratio of energy dissipation under the effect of cyclic deformations. The resulting friction force is usually referred to as viscoelastic friction. On the other hand, several experimental results [28,29,32] clearly indicate that interfacial adhesion and viscoelasticity may interact in controlling the properties of mating interfaces in many tribological systems. However, the concurrent effect of adhesion and viscoelasticity on friction is still poorly understood. Indeed, in the presence of adhesion, besides the usual large-scale energy dissipation occurring in the bulk viscoelastic material, local dissipation also takes place very close to the contact edges (i.e., at the opening or closing crack tips). This latter phenomenon, also known as small-scale viscoelasticity, is usually regarded as a primary cause of adhesive hysteresis, as observed in [110, 111]. However, since the Griffith's energy balance equation $G = \Delta\gamma$ no longer holds for viscoelastic materials, the real value of the energy release rate G at the contact edges is unknown, and a very few studies exist focusing on such case. Most of them rely on scale separation [37, 60–62], thus assuming purely elastic conditions in the bulk material, and local crack propagation criterion at the contact edges. In this class of models, a velocity-dependent energy release rate is introduced as input parameter, often estimated via power-laws according to theories of crack propagation in viscoelastic media [68–72, 84, 112, 113] (see also Chapter 5). However, although very pioneering, these studies are limited to the local viscoelastic regime and fall short in tackling real contact conditions due to the neglected bulk visocelasticity. Indeed, Grosch's experimental investigations [27] clearly show that the interplay between viscoelasticity and adhesion

leads to a friction increase which cannot be explained by simply summing-up the single contributions of adhesion hysteresis and bulk viscoelastic losses [114, 115]. Such an experimental evidence is not fully understood. A possible explanation is that, in the presence of adhesion, the contact area is enlarged, therefore the volume of bulk material undergoing cyclic deformation is increased compared to adhesiveless conditions.
Additionally, several experimental investigations have reported strongly enhanced adhesive properties in rolling contacts against rubber (i.e., viscoelastic) substrates [28,29,32]. Larger pull-off force and contact size are reported in rolling conditions, compared to the static case, thus confirming that the effective adhesive behavior depends on the interaction between small-scale viscoelasticity, interfacial adhesion, and bulk viscoelasticity [116].
In this chapter, we introduce a novel theory to study the adhesive contact of viscoelastic materials in steady-sate sliding or rolling contact with a rigid substrate. The theory provides the closure equations needed to determine the unknown contact domain, which is expressed in terms of a local energy balance, thus generalizing the Griffith's criterion to the case of viscoelastic media. The theory covers a very wide range of sliding velocities, thus providing insights and enlightening most of the available experimental observations in the field.

3.1 Formulation

Let us consider a linear homogeneous viscoelastic slab sliding against a rough surface in the presence of interfacial adhesion. We assume steady state motion at constant velocity $\mathbf{v}$ under displacement controlled conditions assigning the contact penetration Δ. Note that the contact penetration is $\Delta = u_{tot} - u_m$, being u_{tot} the indenter's displacement and u_m the mean displacement of the deformed profile (see Fig. 3.1). We neglect the presence of tangential tractions at the interface. As shown in Chapter 2, using a reference frame co-moving with the indenter, the contact normal stress $\sigma(\mathbf{x})$ and the normal interfacial displacement $v(\mathbf{x})$ (see Sec. 2.2.2 for the definition of the interfacial displacement) are related each other through the convolution product

$$v(\mathbf{x}) = \int d^2x_1 \mathcal{G}(\mathbf{x} - \mathbf{x}_1, \mathbf{v})\sigma(\mathbf{x}_1) \tag{3.1}$$

where $\mathbf{x}$ and $\mathbf{x}_1$ are the in-plane position vectors. Under the assumption of extremely short range adhesive interaction, out of the yet unknown contact domain Ω of size $|\Omega| = A$ the normal stresses vanish, so that the integration domain of the integral in Eq. (3.1) can be set equal to Ω . The kernel $\mathcal{G}(\mathbf{x}, \mathbf{v})$ is the viscoelastic Green function parametrically dependent on the sliding velocity $\mathbf{v}$. As shown in Chapter 2, $\mathcal{G}(\mathbf{x}, \mathbf{v})$ has been determined for several geometric configurations (i.e., displacement or stress boundary conditions) both for periodic and non-periodic contacts, as a function of the slab thickness. Now we recall that for a viscoelastic material $\mathcal{G}(\mathbf{x}, \mathbf{v})$ is an asymmetric function of $\mathbf{x}$ and can be decomposed into an

even (symmetric) $\mathcal{G}^{\mathrm{E}}(\mathbf{x},\mathbf{v})$ part and odd (anti-symmetric) $\mathcal{G}^{\mathrm{O}}(\mathbf{x},\mathbf{v})$ one

$$\mathcal{G}(\mathbf{x},\mathbf{v}) = \mathcal{G}^{\mathrm{E}}(\mathbf{x},\mathbf{v}) + \mathcal{G}^{\mathrm{O}}(\mathbf{x},\mathbf{v}) \tag{3.2}$$

with $\mathcal{G}^{\mathrm{E}}(\mathbf{x},\mathbf{v}) = \frac{1}{2}\left[\mathcal{G}(\mathbf{x},\mathbf{v}) + \mathcal{G}(-\mathbf{x},\mathbf{v})\right]$ and $\mathcal{G}^{\mathrm{O}}(\mathbf{x},\mathbf{v}) = \frac{1}{2}\left[\mathcal{G}(\mathbf{x},\mathbf{v}) - \mathcal{G}(-\mathbf{x},\mathbf{v})\right]$. Notably, the problem at hand belongs to the class of mixed value problems. Indeed, for a given penetration Δ of the indenter, the interfacial displacement field $v(\mathbf{x})$ is prescribed within the contact domain Ω where the deformed slab shape must match the rigid profile's shape. Therefore, since $\sigma(\mathbf{x}) = 0$ out of the contact, Eq. (3.1) can be inverted to calculate the stress field $\sigma(\mathbf{x})$ in the contact domain Ω. On the other hand, out of the contact area the unknown is no longer the normal stress distribution but the displacement field which can be simply calculated from Eq. (3.1) for $\mathbf{x} \notin \Omega$ once that the stress distribution has been determined. However, the contact area $A = |\Omega|$ is not yet known, so that an additional equation (the closure condition) needs to be found to completely solve the problem. In the case of adhesiveless contacts, since the local contact pressure can only takes positive values or vanish, it is enough to enforce the condition that the stress $\sigma(\mathbf{x}) = 0$ at the boundary $\partial\Omega$ of the contact domain. In presence of adhesion instead, the local pressure can also take negative values, i.e. the stress $\sigma(\mathbf{x})$ may change sign over the contact area, therefore an energy closure equation must be enforced. In this case, following the virtual work principle, we need to write a local energy balance which consists in requiring that, at fixed penetration Δ, the work δL_I done by internal viscoelastic stresses equates the work δL_E done by external adhesion forces when the contact area is subjected to a small quasi-static perturbation δA:

$$\delta L_I = \delta L_E \tag{3.3}$$

Let us consider the case of a generic contact area increase from A to $A+\delta A$ (note, δA is a positive quantity). Under the assumption of infinitely short range adhesive forces, no interactions occur out of the contact area. Under these conditions, the contact area variation represents a mode I crack closure, and the work of internal stresses only results from the interfacial stress acting in the small region δA. Then, within δA, the $v(\mathbf{x})$ undergoes a quasi-static change $\Delta v(\mathbf{x})$ from the initial shape (out of contact) $v_-(\mathbf{x}) = v(\mathbf{x},A)$, to final one (in contact) $v_+(\mathbf{x}) = v(\mathbf{x},A+\delta A)$. This zipping process can be described by introducing a dimensionless parameter η that slowly increases from zero to one; therefore, within δA, we have $v(\mathbf{x},\eta) = \eta\Delta v(\mathbf{x}) + v_-(\mathbf{x})$, where $\Delta v(\mathbf{x}) = v_+(\mathbf{x}) - v_-(\mathbf{x})$, and $\eta \in [0,1]$. Linearity entails a similar trend for the stress in δA, thus $\sigma(\mathbf{x},\eta) = \eta\sigma_+(\mathbf{x})$, where $\sigma_+(\mathbf{x}) = \sigma(\mathbf{x},A+\delta A)$. Observing that $\delta v(\mathbf{x},\eta) = \Delta v(\mathbf{x})\delta\eta$, and that the elementary internal work is $\delta L_I = \int d^2x\sigma(\mathbf{x})\delta v(\mathbf{x})$, the total work of internal stresses over the η-governed process can be calculated as

$$(\delta L_I)_T = \int_{\delta A} d^2x \int_0^1 \frac{\partial v}{\partial \eta}(\mathbf{x},\eta)\sigma(\mathbf{x},\eta)\delta\eta = \frac{1}{2}\int_{\delta A} d^2x \Delta v(\mathbf{x})\sigma_+(\mathbf{x}) \tag{3.4}$$

Since $\sigma_-(\mathbf{x}) = \sigma(\mathbf{x},A) = 0$ for $\mathbf{x} \in \delta A$, $\sigma_+(\mathbf{x}) = \sigma_-(\mathbf{x}) = 0$ for $\mathbf{x} \notin A+\delta A$, and $\Delta v(\mathbf{x}) = 0$ for $\mathbf{x} \in A$, the integral in Eq. (3.4) can be extended to the entire

nominal contact area, thus yielding

$$(\delta L_I)_T = \frac{1}{2}\int d^2x[v_+(\mathbf{x}) - v_-(\mathbf{x})][\sigma_+(\mathbf{x}) + \sigma_-(\mathbf{x})] \tag{3.5}$$

Moreover, according to the discussion presented in Chapter 1 (Sec. 1.4.2), in this case the work of internal stresses can be expressed as

$$(\delta L_I)_T = \delta U + \delta L_{\mathrm{P}} \tag{3.6}$$

where elastic energy is given by

$$U = \frac{1}{2}\int d^2x\sigma\left(\mathbf{x}\right) v\left(\mathbf{x}\right)$$

Therefore, the increase of contact area corresponds to the following variation of elastic energy

$$\delta U = \frac{1}{2}\int d^2x[v_+(\mathbf{x})\sigma_+(\mathbf{x}) - v_-(\mathbf{x})\sigma_-(\mathbf{x})] \tag{3.7}$$

which only depends on the symmetric part $\mathcal{G}^{\mathrm{E}}(\mathbf{x},\mathbf{v})$ of the Green's function. Using Eqs. (3.7) and (3.5) in Eq. (3.6), the non-conservative term δL_{P} in the entire $\eta-$governed process describing the increase of contact area can be then calculated as

$$\delta L_{\mathrm{P}} = \frac{1}{2}\int d^2x[v_+(\mathbf{x})\sigma_-(\mathbf{x}) - v_-(\mathbf{x})\sigma_+(\mathbf{x})] \tag{3.8}$$

and using Eqs. (3.1, 3.2) it can be also expressed as

$$\delta L_{\mathrm{P}} = \int d^2x d^2x_1 \mathcal{G}^D_{\mathbf{v}}\left(\mathbf{x}-\mathbf{x}_1\right)\sigma^-\left(\mathbf{x}\right)\sigma^+\left(\mathbf{x}_1\right) \tag{3.9}$$

Eqs. (3.9, 3.8) show that δL_{P} is a non-conservative term, which vanishes in the case of purely elastic material, i.e., when the Green's function is a symmetric function ($\mathcal{G}^{\mathrm{O}}(\mathbf{x},\mathbf{v}) = 0$) [47, 48].
The virtual work of external adhesive forces during the entire displacement process is instead

$$(\delta L_E)_{\mathrm{T}} = \Delta\gamma\delta A \tag{3.10}$$

Thus, exploiting Eq. (3.3) at each single step of the displacement process, the energy balance gives

$$(\delta L_I)_{\mathrm{T}} = (\delta L_E)_{\mathrm{T}} \tag{3.11}$$

Combining Eq. (3.11) with Eq. (3.6), the final expression for the energy balance (i.e., the closure equation of the problem) reads as

$$\left.\frac{\partial U\left(\mathbf{v}\right)}{\partial A}\right|_{\Delta} + \left.\frac{\delta L_{\mathrm{P}}(\mathbf{v})}{\delta A}\right|_{\Delta} = \Delta\gamma \tag{3.12}$$

which can be numerically computed based on contact stress and displacement fields using Eqs. (3.7, 3.8). Also, recalling the usual definition of the energy release rate $G = (\partial U/\partial A)_{\Delta}$ at fixed displacement of the indenter, we get

$$G(\mathbf{v}) = \Delta\gamma - \left.\frac{\delta L_{\mathrm{P}}(\mathbf{v})}{\delta A}\right|_{\Delta} \tag{3.13}$$

Notably, we recall that the term δL_{P} might be both positive or negative (as shown in Chapter 1), therefore the energy release rate can be either larger or smaller than $\Delta\gamma$, and can even vanish or become negative. When this happens adhesion is switched off, being totally masked by viscoelasticity. Also note that in this treatment we do not take into account the influence of the highly non linear phenomena occurring very close to the tip of the contact edges (in the so called process zone), which may modify the effective energy of adhesion [117, 121–125]. These effects can be included in the present theory by replacing $\Delta\gamma$ with an apparent energy of adhesion G_0 measured at very low sliding velocity. Moreover, in the present theory, the quantity δA is a characteristic size of the problem, whose order of magnitude should be the same of the process zone's size. However, the specific value of δA set in calculations doesn't change the qualitative contact behavior, as shown in Sec. 3.8 and in Chapter 5. Notably, in adhesiveless contacts, i.e. for $\Delta\gamma = 0$, the stress intensity factor at the edge of the contact vanishes so that the displacement field does not present any discontinuous jump as the contact area changes of the infinitesimally quantity δA, leading to $\delta L = \delta U = \delta L_P = 0$ in Eq. (3.13).

3.2 The case of a sinusoidal rigid indenter

In this section we discuss the 1D+1D adhesive periodic contact of a viscoelastic half-plane sliding at constant velocity v against a sinusoidal rigid indenter of wavelength λ, amplitude Λ and wave vector $k = 2\pi/\lambda$. All the geometrical parameters needed to define the problem are shown in Fig. 3.1. The contact domain is defined by the positive quantities l_1 and l_2, which represent the distance of the two contact edges (respectively trailing edge and leading edge) from summit of the sinusoidal indenter. The semi-width of the contact length is $a = (l_1 + l_2)/2$ and the eccentricity is $e = (l_2 - l_1)/2$. In this 1D+1D case [107] the viscoelastic Green's function (see Sec 2.2.2) is

$$\mathcal{G}(x, v) = J(0)\frac{2(1-\nu^2)}{\pi}\log\left|2\sin\frac{kx}{2}\right| + \frac{2(1-\nu^2)}{\pi}\int_{0^+}^{+\infty} dt \log\left|2\sin\frac{k(x+vt)}{2}\right| \dot{J}(t) \tag{3.14}$$

The linear viscoelastic solid is modelled with one relaxation time τ, and the creep function is

$$J(t) = \mathcal{H}(t)\left[\frac{1}{E_0} - \left(\frac{1}{E_0} - \frac{1}{E_\infty}\right)\exp\left(-\frac{t}{\tau}\right)\right] \tag{3.15}$$

where E_∞ and E_0 are, respectively, the high and low frequency viscoelastic modulus, and $\mathcal{H}(t)$ is the Heaviside unit-step function. Although real viscoelastic

materials are undoubtedly characterized by multiple relaxation times, qualitative physical insights can still be obtained using a single relaxation time
Within the contact area, the interfacial displacement must match the indenter shape; therefore, $v(x) = \Lambda\cos(kx) - \Lambda + \Delta$ and the contact stress distribution can be found, at given Δ, by solving the equation

$$\int_{-l_1}^{l_2} dx_1 \mathcal{G}(x - x_1, v)\,\sigma(x_1) = \Lambda\cos(kx) - \Lambda + \Delta \tag{3.16}$$

In order to calculated the unknown contact parameters l_1 and l_2 we need to enforce the energy balance Eq. (3.12) at each edge of the contact, i.e.

$$\left.\frac{\partial U(v)}{\partial l_1}\right|_{\Delta,l_2} + \left.\frac{\delta L_{\mathrm{P}_1}(v)}{\delta l_1}\right|_{\Delta,l_2} = \Delta\gamma \tag{3.17}$$

$$\left.\frac{\partial U(v)}{\partial l_2}\right|_{\Delta,l_1} + \left.\frac{\delta L_{\mathrm{P}_2}(v)}{\delta l_2}\right|_{\Delta,l_1} = \Delta\gamma \tag{3.18}$$

with δl_1 and δl_2 being, respectively, the infinitesimal independent variations of the contact area at the trailing and leading edges. The displacement field and the contact stresses are numerically calculated by relying on the numerical procedure addressed in [47].

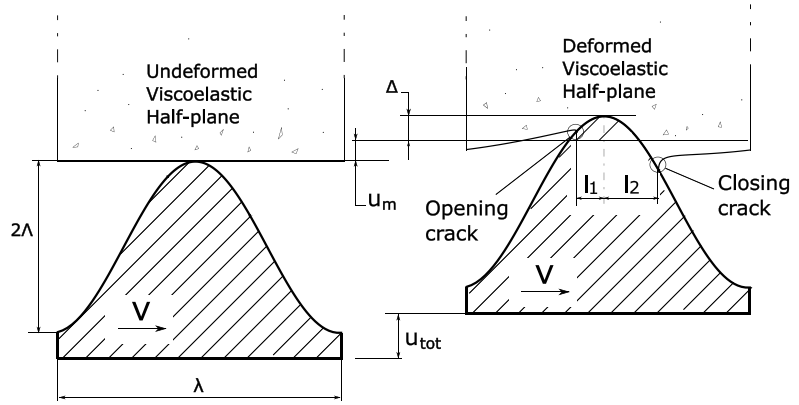

Figure 3.1: The schematic of the sliding contact between a viscoelastic solid and a rigid wavy indenter. Geometric parameters are also shown.

Once the contact problem is solved [notably, the contact pressure is $p(x) = -\sigma(x)$], we can calculate the remote average pressure

$$p_\infty = \frac{1}{\lambda}\int_{-l_1}^{l_2} p(x)dx, \tag{3.19}$$

as well as the friction coefficient

$$\mu = -\frac{1}{\lambda p_\infty}\int_{-l_1}^{l_2} dx p(x)u'(x), \tag{3.20}$$

and the strain energy release rates at the opening and closing cracks (trailing and leading edges) respectively

$$G_1(v) = \Delta\gamma - \left.\frac{\delta L_{\mathrm{P}_1}(v)}{\delta l_1}\right|_{\Delta, l_2} \tag{3.21}$$

$$G_2(v) = \Delta\gamma - \left.\frac{\delta L_{\mathrm{P}_2}(v)}{\delta l_2}\right|_{\Delta, l_1} \tag{3.22}$$

3.2.1 Dimensionless parameters

The problem can be formulated in term of the following dimensionless parameters: $\tilde{x} = kx$; $\tilde{a} = ka$; $\tilde{e} = ke$; $\tilde{p} = 2(1-\nu^2)p/(E_0 k\Lambda)$; $\tilde{\gamma} = (1-\nu^2)k\Delta\gamma/(\pi E_0)$; $\zeta = kv\tau$; $\tilde{u} = u/\Lambda$; $\tilde{\Lambda} = k\Lambda$; $\tilde{v} = v/\Lambda$; $\tilde{\Delta} = \Delta/\Lambda$; $\beta = E_\infty/E_0$. Also we define the dimensionless elastic energy as $\tilde{U} = 2(1-\nu^2)U/(E_0\Lambda^2)$ and the dimensionless non-conservative work of internal stresses as $\delta\tilde{L}_{\mathrm{P}} = 2(1-\nu^2)\delta L_{\mathrm{P}}/(E_0\Lambda^2)$. Moreover, regarding the assumption of JKR-like infinitely short-range adhesive interactions, we observe that the Tabor parameter in the stiffer case of $E = E_\infty$ can be rewritten according to our dimensionless quantities as $\mu_{\mathrm{T}} = [(\pi\Gamma/\beta)^2\tilde{\Lambda}^3/(kZ_0)^3]^{1/3}$ and still gives $\mu_{\mathrm{T}} \gg 1$ even for low values of the reduced adhesion energy Γ (≈ 0.001) and high values of β ($\gg 10$) provided that the periodic profile's wavelength $\lambda \gtrsim 10\mu m$, which is a reasonable value for our case of interest (also, we set $\tilde{\Lambda} \approx 1$ to enforce linear elasticity and $Z_0 \approx 1nm$). Now observe that Eq. (3.16) can be rewritten as:

$$\int_{-\tilde{l}_1}^{\tilde{l}_2} d\tilde{x}_1 \tilde{\mathcal{G}}(\tilde{x} - \tilde{x}_1, \zeta)\,\tilde{\sigma}(x_1) = \tilde{v}(\tilde{x}) = \cos(\tilde{x}) - 1 + \tilde{\Delta} \tag{3.23}$$

where

$$\tilde{\mathcal{G}}(\tilde{x}, \zeta) = \frac{1}{\beta}\frac{1}{\pi}\log\left|2\sin\frac{\tilde{x}}{2}\right| + \frac{1}{\pi}\left(1 - \frac{1}{\beta}\right)\int_{0^+}^{+\infty} dz \log\left|2\sin\frac{(\tilde{x} + \zeta z)}{2}\right|\exp(-z) \tag{3.24}$$

And the closure equations written in dimensionless form read as

$$\begin{aligned} \left.\frac{\partial\tilde{U}(\zeta)}{\partial\tilde{l}_1}\right|_{\tilde{\Delta}, \tilde{l}_2} + \left.\frac{\delta\tilde{L}_{\mathrm{P}}(\zeta)}{\delta\tilde{l}_1}\right|_{\tilde{\Delta}, \tilde{l}_2} &= \tilde{\gamma}\frac{2\pi}{\tilde{\Lambda}^2} \\ \left.\frac{\partial\tilde{U}(\zeta)}{\partial\tilde{l}_2}\right|_{\tilde{\Delta}, \tilde{l}_1} + \left.\frac{\delta\tilde{L}_{\mathrm{P}}(\zeta)}{\delta\tilde{l}_2}\right|_{\tilde{\Delta}, \tilde{l}_1} &= \tilde{\gamma}\frac{2\pi}{\tilde{\Lambda}^2} \end{aligned} \tag{3.25}$$

Equations (3.23, 3.24, 3.25) show that adhesion is governed by the parameter $\Gamma = \tilde{\gamma}/\tilde{\Lambda}^2$. More specifically, the contact solution is uniquely determined by the parameters Γ, ζ, $\tilde{\Delta}$ or, analogously, by Γ, ζ, $\tilde{p}_\infty$. In our calculations, unless differently specified, we set $\delta\tilde{l}_1 = \delta\tilde{l}_2 = 0.001$ in Eqs. (3.25).

3.3 Numerical implementation

Now, in order to solve numerically Eq. (3.23) we need to discretize the contact domain. We rely on the numerical procedure addressed in [47] based on a non-uniform adaptive mesh. A different grid of points has to be generated for every single contact area. Thus, let us consider the generic contact area identified by the interval $[\tilde{a}_i, \tilde{b}_i]$, define the quantities $\mu_i = \left(\tilde{a}_i + \tilde{b}_i\right)/2$ and $\alpha_i = \left(\tilde{b}_i - \tilde{a}_i\right)/2 > 0$, and let us apply the following transformation rule $\eta = \tilde{x} - \mu_i$, so that the interval $[\tilde{a}_i, \tilde{b}_i]$ is mapped onto the interval $[-\alpha_i, \alpha_i]$. Now, let $\mathcal{U}$ be a uniform mesh of $N+1$ points ζ_l which contains the extreme points $-\alpha_i$ and α_i of the contact region. We have

$$\zeta_l = -\alpha_i + 2\alpha_i \frac{l}{N}; \qquad l = 0, ..., N \tag{3.26}$$

Also, let us define the non uniform mesh $\mathcal{P}$ obtained by the above grid $\mathcal{U}$ by means of the following transformation rule

$$z_l = \mathcal{M}(\zeta_l); \qquad l = 0, ..., N \tag{3.27}$$

where the function $\mathcal{M}(\zeta)$ will be defined below. We only require that $-\alpha_i = \mathcal{M}(-\alpha_i)$ and $\alpha_i = \mathcal{M}(\alpha_i)$. The solution of the integral equation will be sought on a different mesh $\mathcal{C}$, the points of which are defined as

$$\xi_l = \frac{z_l + z_{l-1}}{2}; \qquad l = 1, ..., N \tag{3.28}$$

Observe that the $\mathcal{C}$-mesh does not contain the stress singular points $-\alpha_i$ and α_i. Also define the mesh $\mathcal{H}$ constituted of N elements h_l

$$h_l = z_l - z_{l-1}; \qquad l = 1, ..., N \tag{3.29}$$

In order to find an accurate numerical solution, and in particular to accurately describe the singular behavior of the interfacial stress, the non uniform mesh $\mathcal{P}$ has to be chosen in such a way that the point density diverges at the edges of the contact areas. Therefore, the problem is to define a function $\mathcal{M}(\zeta)$ [see Eq. (3.27)] which fulfills these requirements. The point density ρ is defined as

$$\rho(\zeta) = \frac{1}{\mathcal{M}'(\zeta)}. \tag{3.30}$$

with

$$\int_{-\alpha_i}^{\alpha_i} \mathcal{M}'(\zeta)\, d\zeta = \mathcal{M}(\alpha_i) - \mathcal{M}(-\alpha_i) = 2\alpha_i \tag{3.31}$$

Since the stress σ_{yy} has a square root singularity at the edge of the contact we may choose

$$\rho(s) = C \frac{1}{[\cos(s) - \cos(\alpha_i)]^n} \tag{3.32}$$

with $n \geq 1/2$, where the constant quantity C can be calculated from Eq. (3.31)

$$C = \frac{1}{2\alpha_i} \int_{-\alpha_i}^{\alpha_i} [\cos(\xi) - \cos(\alpha_i)]^n \, d\xi \tag{3.33}$$

Thus, the function $\mathcal{M}(\zeta)$ becomes

$$\mathcal{M}(\zeta) = \int_0^{\zeta} \mathcal{M}'(\xi)\, d\xi = \frac{1}{C} \int_0^{\zeta} \left[\cos(\xi) - \cos(\alpha_i)\right]^n d\xi \tag{3.34}$$

Now, we can convert Eq. (3.23) into a system of linear equations by simply using a numerical quadrature rule

$$\sum_{q=1}^{N} \int_{\xi_q - h_q/2}^{\xi_q + h_q/2} d\eta \tilde{\mathcal{G}}(\xi_l - \eta, \zeta)\, \tilde{\sigma}_q = \tilde{v}(\xi_l)$$

where $\tilde{\sigma}_q$ is the uniform stress acting within the $q-th$ element. Therefore, we need to solve the following system of N unknowns and N equations

$$\sum_{q=1}^{N} B_{lq} \tilde{\sigma}_q = \tilde{v}(\xi_l); \qquad l = 1, ..., N \tag{3.35}$$

Thus, we can write

$$B_{lq} = \int_{\xi_q - h_q/2}^{\xi_q + h_q/2} d\eta \tilde{\mathcal{G}}(\xi_l - \eta, \zeta) = \int_{\xi_l - \xi_q - h_q/2}^{\xi_l - \xi_q + h_q/2} d\varepsilon \tilde{\mathcal{G}}(\varepsilon, \zeta) \tag{3.36}$$

Now note that the quantity

$$-\int_0^{\theta} d\varepsilon \log\left[2\left|\sin\left(\frac{\varepsilon}{2}\right)\right|\right] = \mathrm{Cl}_2(\theta)$$

is the Clausen integral, related to the dilogarithm function $\mathrm{L}_2(\theta) = \sum_{m=1}^{+\infty} (\theta^m / m^2)$ by means of the formula $\mathrm{Cl}_2(\theta) = \mathrm{Im}[\mathrm{L}_2(e^{i\theta})]$. Therefore, following Eq. (3.24), we can define

$$\mathcal{K}(\theta, \zeta) = \int_0^{\theta} d\varepsilon \tilde{\mathcal{G}}(\varepsilon, \zeta) = -\frac{1}{\beta\pi}\left[\mathrm{Cl}_2(\theta) + (\beta - 1)\int_{0^+}^{+\infty} dz \exp(-z)\left[\mathrm{Cl}_2(\theta + \zeta z) - \mathrm{Cl}_2(\zeta z)\right]\right]$$

and according to Eq. 3.36 we obtain

$$B_{lq} = \mathcal{K}(\xi_l - \xi_q + h_q/2, \zeta) - \mathcal{K}(\xi_l - \xi_q - h_q/2, \zeta)$$

Note that the integral

$$I(x) = \int_{0^+}^{+\infty} dz \exp(-z)\left[\mathrm{Cl}_2(x + \zeta z)\right]$$

can be easily numerically computed, since $\mathrm{Cl}_2(x)$ is a regular periodic function. Moreover, also its analytical expression can be derived:

$$I(x) = \mathrm{Im}[-\zeta^2 {}_2F_1\left(1, \frac{i}{\zeta}, \frac{1+\zeta}{\zeta}, e^{ix}\right) + \zeta\left(\zeta - i\log\left[1 - e^{ix}\right]\right) + \mathrm{L}_2(e^{ix})]$$

where ${}_2F_1(a, b, c, d)$ is the Gaussian Hypergeometric Function (see [126, 127] for details on these types of functions).

3.4 Contact solutions

Fig. 3.2 shows the dimensionless semi-width of the contact $\tilde{a}$ [see Figs. 3.2(a) and (b)] and the dimensionless eccentricity $\tilde{e}$ [see Figs. 3.2(c) and (d)] as a function of the dimensionless sliding velocity $\zeta = kv\tau$, under fixed penetration $\tilde{\Delta}$ or load $\tilde{p}_\infty$. The adhesiveless case [43, 103, 107] is also reported for reference (dashed lines). Note that at very low or very high sliding velocity the system recovers the elastic limit (wih vanishing eccentricity) and the contact solution corresponds to that derived in [37] for elastic moduli E_0 and E_∞ respectively. Notably, the high velocity solution exhibits a smaller contact area because of the larger stiffness of the material. Noteworthy, as the sliding velocity ζ grows from zero, a very significant increase of the contact area is observed [Figs. 3.2(a) and (b)] which presents a maximum at a certain intermediate speed. This behavior is not observed for adhesiveless viscoelastic contacts, and is very peculiar of viscoelastic adhesion. Similar results have been fund by several experimentalists as in the case of rolling contacts between rigid cylinders and rubbery-like substrates ([28, 32]). This behavior is ascribable to the local viscoelastic losses occurring very close to the trailing (crack opening) edge of the contact, where the material is excited at a frequency v/ρ, being ρ the radius of curvature at the tip of the crack. Therefore, at sliding speed $v \approx \rho/\tau << \lambda/\tau$ most of the energy dissipation occurs at the opening crack whereas the bulk of material, being excited at frequency $v/\lambda \ll 1/\tau$, behaves as an almost perfectly elastic material with low frequency elastic modulus E_0. This regime is know as the small-scale viscoelasticity regime and leads to what is known as adhesive friction (see Sec. 3.6). In Figs. 3.2(c) and (d) we observe that at dimensionless speed at which the contact size $\tilde{a}$ takes its maximum value, the eccentricity $\tilde{e}$ is negative so that the whole contact is shifted backward. Since in the adhesiveless case the opposite behavior occurs [43, 103, 107], we conclude that in the range of velocity governed by the small-scale viscoelasticity the contact area is strongly enlarged at the trailing edge. Indeed, the small-scale viscoelastic losses are triggered by adhesion, i.e., they vanish in adhesiveless contacts. This is confirmed by the deformed contact configurations reported in Fig. 3.4 (a), which refers to $v \approx \rho/\tau << \lambda/\tau$ in agreement with experimental observations [28, 32]. However, as the sliding velocity increases (i.e. for $\rho/\tau < v < \lambda/\tau$ as in Fig. 3.4(b)), a large amount of energy is dissipated in the bulk of the material and large-scale (bulk) viscoelastic losses take place in addition to local hysteresis at the trailing and closing edges. In this case, the contact area and the eccentricity gradually invert their trend (see Figs. 3.2). At higher velocity $v \approx \lambda/\tau \gg \rho/\tau$ [see Fig. 3.4 (c)], the sliding speed is so high that the material at the edges of the contact is in the glassy state and behaves as an elastic material with elastic modulus E_∞. Under this conditions the bulk viscoelasticity almost entirely governs the behavior of the system, and therefore the qualitative contact behavior resembles that of the viscoelastic adhesiveless case.

Fig. 3.3 investigates the asymmetric contact pressure distribution for a positive (a) and a negative (b) value of the contact penetration and different values of the sliding speed. Notably, a positive pressure peak is observed at the contact leading

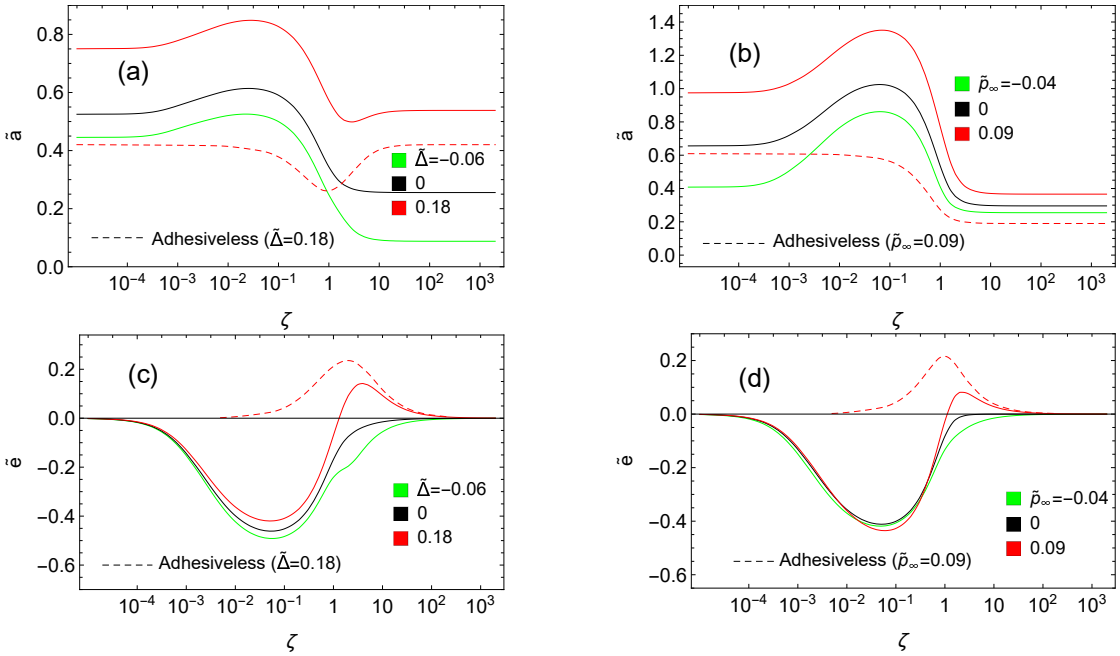

Figure 3.2: The dimensionless semi-width of the contact $\tilde{a}$, and the dimensionless eccentricity $\tilde{e}$ as functions of the dimensionless sliding velocity ζ, for different values of the dimensionless remote pressure $\tilde{p}_\infty$, and the dimensionless penetration $\tilde{\Delta}$. Results are shown for $\beta = 10$ and $\Gamma = 0.008$.

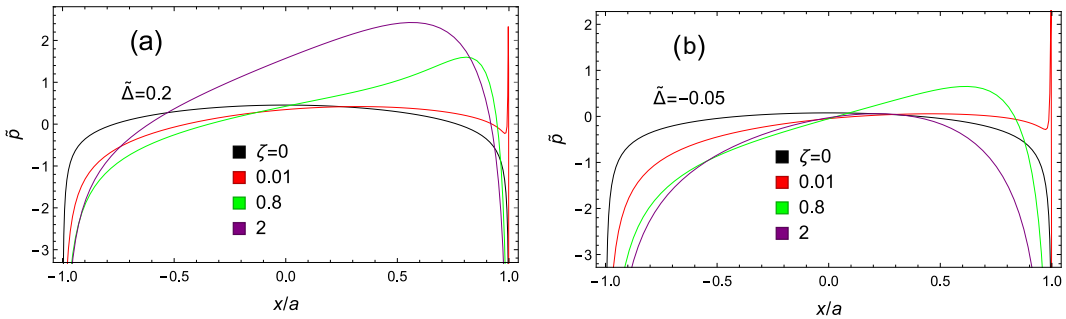

Figure 3.3: The dimensionless contact pressure $\tilde{p}$ as function of the normalized contact coordinate x/a for a positive (a) and a negative (b) value of the contact penetration $\tilde{\Delta}$ and different values of the dimensionless sliding velocity ζ. Results are shown for $\beta = 10$ and $\Gamma = 0.008$.

edge, in agreement with previous studies [30, 103, 107, 128]. Interestingly, at low velocity, the peak is found highly pronounced and localized at small distances from the contact edge (see $\zeta = 0.01$). This behavior originates from the small-scale viscoelastic response of the material, in agreement with the discussion presented in Chapter 5 (see Fig. 5.4). Fig. 3.5 more deeply investigates the shape of contact for negative and positive penetrations. Notably, within the small-scale viscoelastic regime, a magnification of the contact trailing edge at distance from the crack tip of order $v\tau$ reveals the typical trumpet shape of opening cracks, as predicted by De Gennes [129] and in agreement with the discussion presented in Chapter 5 (see Fig. 5.2).

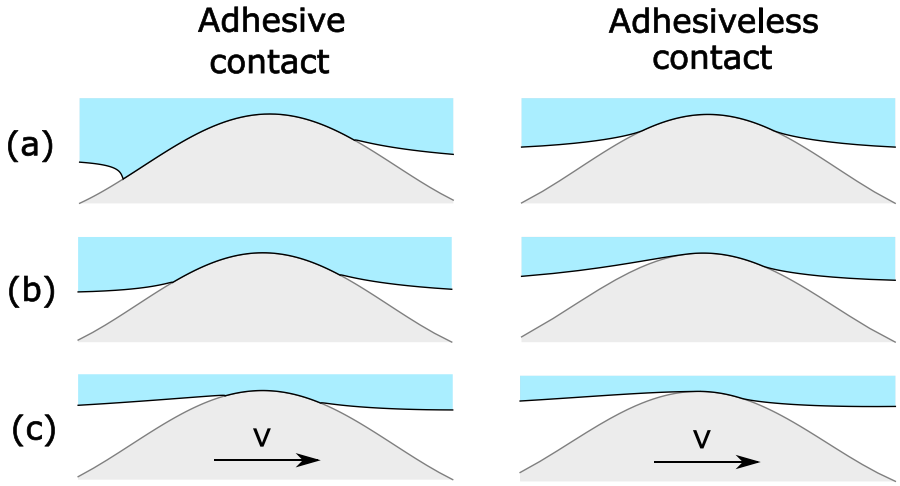

Figure 3.4: The comparison between the deformed contact configurations predicted for adhesive and adhesiveless conditions at different sliding velocity values. (a) small-scale viscoelastic regime, $\zeta = 0.01$. (b) coupled large and small scale viscoelastic regime , $\zeta = 0.8$. (c) bulk viscoelastic regime , $\zeta = 2$. Results are shown for $\widetilde{p}_\infty = 0.15$, $\Gamma = 0.008$, $\beta = 10$.

Figure 3.6 shows the effect of the dimensionless parameter $\Gamma = \tilde{\gamma}/\tilde{\Lambda}^2$ on the semi-width of the contact $\tilde{a}$ and eccentricity $\tilde{e}$. As expected increasing Γ from zero exacerbates the effect of adhesion hysteresis (i.e. the small scale viscoelasticity) in determining the contact area size and eccentricity, thus larger value of ζ are required for the system to resemble the behavior of a purely viscoelastic adhesiveless contact.

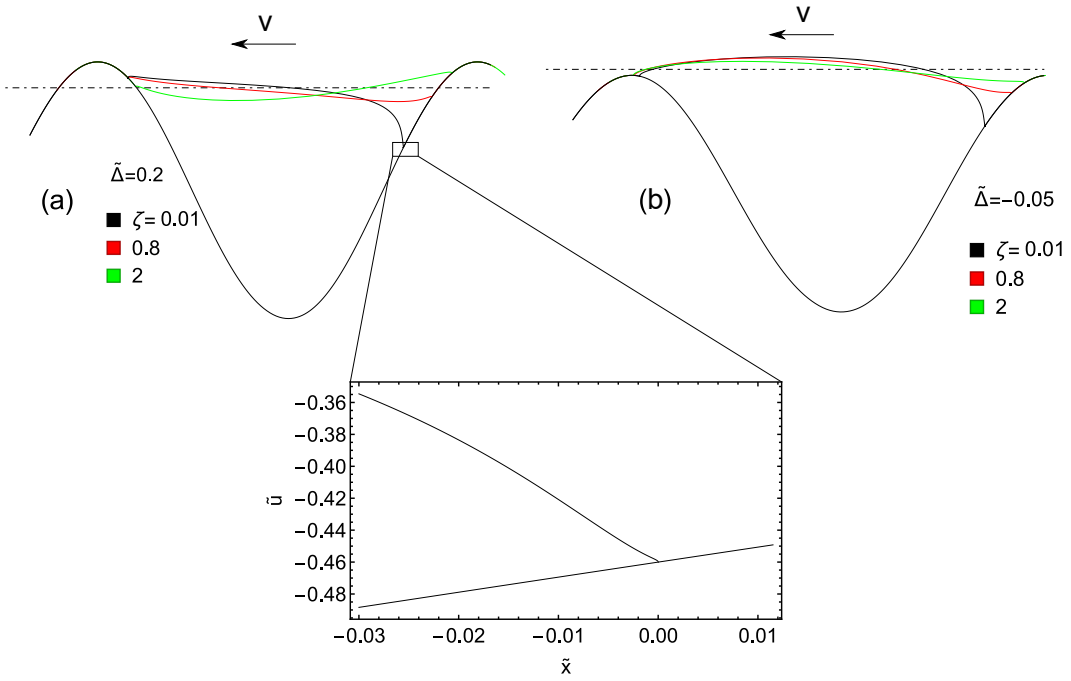

Figure 3.5: The deformed shape of contact for a positive (a) and a negative (b) value of the contact penetration $\tilde{\Delta}$ and different values of the dimensionless sliding velocity ζ. The inset shows a magnification of the contact trailing edge for the small-scale viscoelastic regime. Results are shown for $\beta = 10$ and $\Gamma = 0.008$.

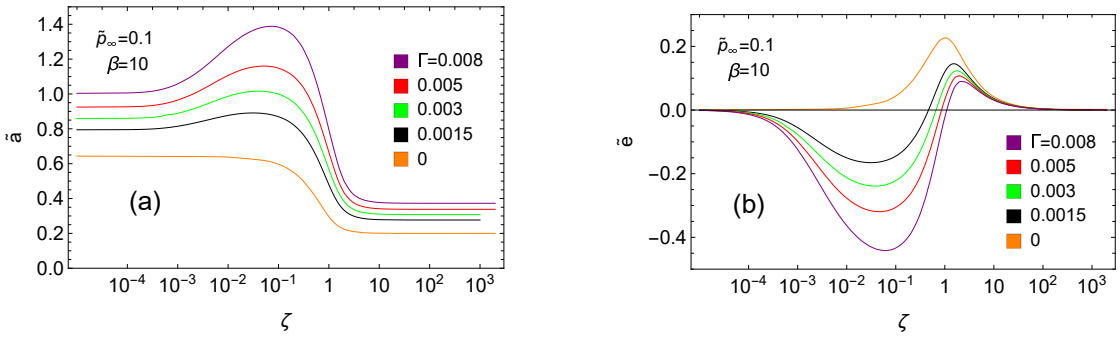

Figure 3.6: The effect of the reduced energy of adhesion $\Gamma = \tilde{\gamma}/\tilde{\Lambda}^2$ on the dimensionless semi-width $\tilde{a}$ (a) and the dimensionless eccentricity $\tilde{e}$ (b) shown as functions of the dimensionless sliding velocity ζ. Results are shown for $\beta = 10$, $\tilde{p}_\infty = 0.1$.

3.5 The energy release rate

Fig. 3.7 reports the equilibrium values of the reduced strain energy release rates $G_1/\Delta\gamma$ (at the opening crack) and $G_2/\Delta\gamma$ (at the closing crack) as a function of the dimensionless sliding velocity ζ, for different values of the dimensionless remote pressure. The effect of the dimensionless parameter $\beta = E_\infty/E_0$ on the curves is also shown in Fig. 3.8 . It is worth noticing that in some previous studies (see for instance [37, 60–62]), the value of G at the contact trailing and leading edges represents an input parameter, usually quantified depending on the relative velocity according to theories of viscoelastic crack opening [69–72, 84, 112] or closing [68, 70, 113], or fitted from experimental data. In this class of models, the contact parameters (e.g., the contact length and the eccentricity as in the present case) can be therefore calculated by enforcing the value of G at the contact edges [37]. On the contrary, in the present study, the equilibrium values of G_1 and G_2 are calculated as part of the solution. As expected, at very low or very high velocities, the ratios $G_1/\Delta\gamma$ and $G_2/\Delta\gamma$ approach the unit value as the material behaves elastically, in agreement with Eqs. (3.21, 3.22). In such conditions, the non-conservative contribution to the work of internal stresses vanishes. Increasing ζ from zero, we observe an increase of the reduced strain energy release rate $G_1/\Delta\gamma$ at the opening crack edge, and a decreases of the ratio $G_2/\Delta\gamma$ the closing crack edge. As the velocity is increased $G_1/\Delta\gamma$ approaches a maximum value $G_{1\,\max}/\Delta\gamma$ not so far from $\beta = E_\infty/E_0$, whereas $G_2/\Delta\gamma$ reaches a minimum $G_{2\,\min}/\Delta\gamma$ relatively close to $\beta^{-1} = E_0/E_\infty$. Therefore increasing β leads to an increment of $G_{1\,\max}/\Delta\gamma$ and to a decrement of $G_{2\,\min}/\Delta\gamma$ as observed in Fig. 3.8. Importantly, within the small-scale viscoelastic regime, results are in perfect agreement with the fact that in such conditions the local behavior at the contact edges is analogue to that of a crack propagating within an infinitely extended solid (see also Chapter 5). However, the overall non monotonic trend is a consequence of the finite system size, the finite contact length, which causes the viscoelastic stiffening of the bulk of the material, thus recovering the fully elastic solution at high speed. A similar behavior has been predicted by Persson [85, 130]. For infinite systems, instead, this cannot be observed as the very majority of the material is totally relaxed and behaves as an elastic soft solids with modulus E_0. Therefore, energy is dissipated only close to the crack tip hence the system is always in the small-scale viscoelasticity regime. For infinite systems, at sufficiently high crack propagation velocity, the material will behave as very stiff elastic solids at the tip of the crack and as a very soft elastic solids into the bulk thus leading to values of $G_1/\Delta\gamma = \beta = E_\infty/E_0$ and $G_2/\Delta\gamma = \beta^{-1} = E_0/E_\infty$, as shown in Chapter 5 and in [68–71, 112, 113].

Note that for negative value of the remote pressure $\tilde{p}_\infty$ the trend of $G_1/\Delta\gamma$ and $G_2/\Delta\gamma$ is described by bell-shaped curves, with G_1 being always greater than $\Delta\gamma$ and G_2 always smaller. However, when the remote pressure $\tilde{p}_\infty$ is positive, the shape of the reduced energy release rates changes. In this case G_1 may reach a minimum value less than $\Delta\gamma$ and might also become negative, whereas G_2 reaches a maximum value greater than $\Delta\gamma$. This happens because the viscoelastic stiff-

ening of the bulk material tends to move the contact forward: a larger amount of elastic energy is stored at the closing edge compared to the opening edge, thus making G_2 greater than G_1 at sufficiently large velocity. When this happens adhesion is switched off, being totally masked by viscoelasticity. Importantly, these results reflect the fact that, in Eqs. (3.21, 3.22), the non-conservative work contribution might take both positive or negative values depending on specific contact conditions. Note that negative values of G would be physically unreasonable only within the small-scale viscoelastic regime. Indeed the energy balance of a single crack propagating in an infinite system reads as $G = \Delta\gamma + P_d/v$ where this time P_d is a positive term representing the amount of energy dissipated per unit time and unit thickness of the system and v is the crack velocity. This implies that $G > \Delta\gamma$ for the opening crack ($v > 0$) and $G < \Delta\gamma$ for the closing crack ($v < 0$) (see also Chapter 4 and [68–71, 112, 113]). Instead, in the present sliding contact case, the energy balance of the system reads as

$$F_L v = P_d \tag{3.37}$$

where F_L is the lateral force per unit system's thickness acting over each periodic cell (i.e., the frictional stress) and P_d is the amount of internal viscoelastic dissipation occurring within the whole volume of the periodic cell per unit time, i.e., it includes both the local and bulk contributions. Notably, within the small-scale viscoelastic regime, the quantity P_d only includes local losses and therefore can be precisely split as $P_d = P_{d,1} + P_{d,2}$ where $P_{d,1}$ and $P_{d,2}$ are the amounts of dissipation localized at the trailing and leading edges respectively. Therefore, at relatively low velocity, since the two edges behave as two independent cracks, we can write that $G_1 = \Delta\gamma + P_{d,1}/v$ and $G_2 = \Delta\gamma - P_{d,2}/v$ and thus substituting these expressions into Eq. (3.37) while using that $P_d = P_{d,1} + P_{d,2}$ we obtain

$$F_L = G_1 - G_2 \tag{3.38}$$

Eq. (3.38) shows that the adhesion hysteresis is importantly associated with the frictional behavior of the contact (see the section 3.6). In fact, G_1 and G_2 can be regarded as effective energies of adhesion, therefore Eq. (3.38) simply shows that within the small-scale vsicoelastic regime the overall lateral force is ascribable to the difference between the energy spent to separate the surfaces at the trailing edge and the energy recovered when they come back into contact at the leading edge. On the other hand, at higher velocity, there is no possibility to separate the small-scale and the large-scale viscoelastic losses, therefore Eq. (3.37) cannot be directly related to G_1 and G_2. Indeed, the overall contact behavior in general conditions is described by the closure equations Eqs. (3.21, 3.22), which represents a virtual work balance, in which this time the quantity δL_p is not a direct quantification of the internal dissipation and might also be negative (as demonstrated in Chapter 1).

Importantly, in Figure 3.9 we show that, by increasing the size of our system (i.e. the wavelength λ), the response asymptotically approaches the one predicted for the infinite case, and as expected $G_{1\,\max}/\Delta\gamma$ and $G_{2\,\min}/\Delta\gamma$ approach the values of β and β^{-1}, respectively.

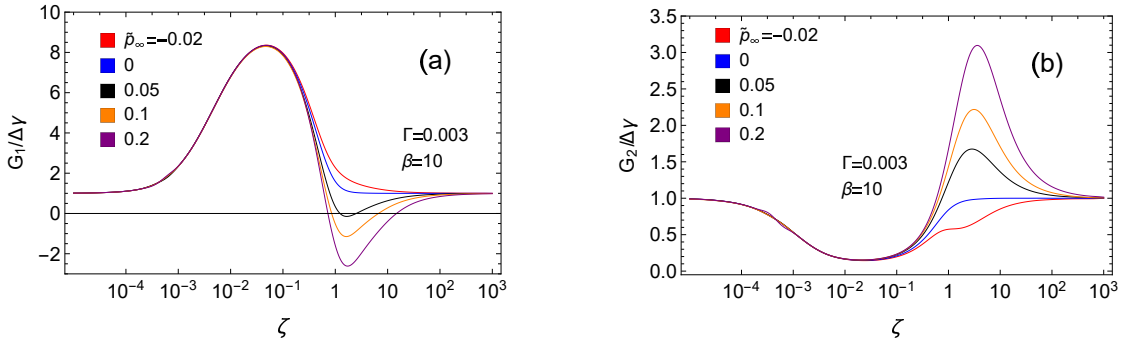

Figure 3.7: The reduced energy realase rates $G/\Delta\gamma$ as functions of the dimensionless sliding velocity ζ, for different values of the dimensionless remote pressure $\tilde{p}_\infty$. (a) $G_1/\Delta\gamma$ refers to the traling edge of the contact (opening crack), (b) $G_2/\Delta\gamma$ refers to the leading edge (closing crack). Results are shown for $\Gamma = 0.003$, $\beta = 10$.

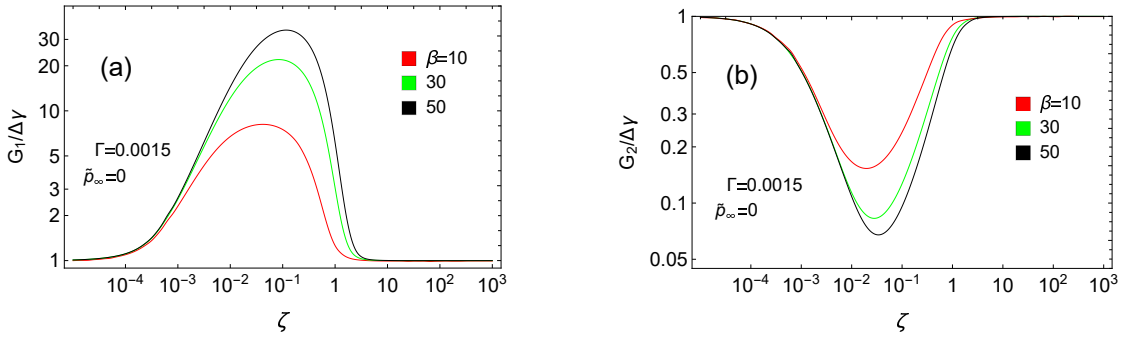

Figure 3.8: The effect of the parameter $\beta = E_\infty/E_0$ on the trend of $G/\Delta\gamma$ vs. ζ. Data are shown in log-log form. (a) $G_1/\Delta\gamma$ refers to the opening crack, (b) $G_2/\Delta\gamma$ refers to the closing crack. Results are shown for $\Gamma = 0.0015$, $\tilde{p}_\infty = 0$.

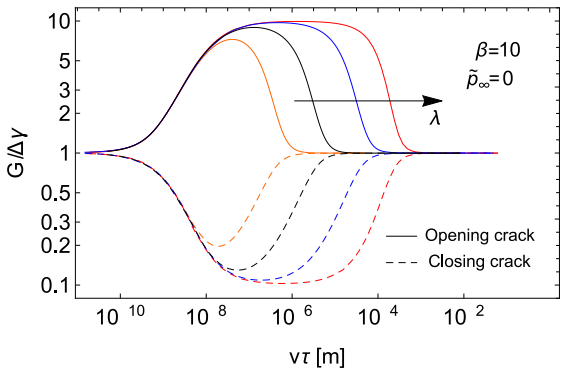

Figure 3.9: The effect of the wavelength of the sinusoidal indenter λ on the trend of $G/\Delta\gamma$ vs. ζ. Data are shown in log-log form. Solid line refers to the opening crack ($G_1/\Delta\gamma$), dashed line refers to the closing crack ($G_2/\Delta\gamma$). Results are shown for $\beta = 10$, $\tilde{p}_\infty = 0$.

3.6 Friction

In this section, we investigate the frictional behavior of the system. Friction is originated by the cyclic deformations occurring during the relative motion between the indenter and the solid and, in turn, by energy dissipation within the viscoelastic material. As a consequence, the contact pressure distribution $p(x)$ is asymmetric, and the resulting contact force acting on the rigid asperity presents a tangential component opposing the indenter sliding motion, which is usually referred to as viscoelastic friction. According to Refs. [25, 30, 131], the viscoelastic friction coefficient can be calculated through Eq. (3.20). However using the dimensionless quatities define so far one obtains that

$$\mu = -\frac{\tilde{\Lambda}}{2\pi}\frac{1}{\tilde{p}_\infty}\int_{\tilde{-l}_1}^{\tilde{l}_2} d\tilde{x}\tilde{p}\left(\tilde{x}\right)\tilde{u}'\left(\tilde{x}\right) \tag{3.39}$$

It follows that the friction coefficient is proportional to $\tilde{\Lambda} = k\Lambda$. Therefore we will refer to the reduce coefficient of friction as $\tilde{\mu} = \mu/\tilde{\Lambda}$. Notably, as already mentioned in the previous section, the reduced friction coefficient $\tilde{\mu}$ takes into account the energy dissipation occurring in the whole viscoelastic solid, i.e. both large- and small-scale viscoelastic hysteresis, according to Eq. (3.37). In order to provide a rough estimate of the contribution to the overall friction ascribable to adhesion hysteresis (i.e., to local viscoelastic losses close to the contact edges), we define the reduced adhesive friction coefficient as

$$\tilde{\mu}_a = \frac{1}{\tilde{\Lambda}}\frac{G_1 - G_2}{\lambda p_\infty} \tag{3.40}$$

Similarly, we also refer to $\tilde{\mu}_0$ as to the reduced friction coefficient calculated in adhesiveless viscoelastic contacts. Notice that, since small-scale viscoealstic losses vanish when $\Delta\gamma = 0$, $\tilde{\mu}_0$ entirely originates from bulk viscoelastic hysteresis. Figure 3.10 reports, at given remote pressure $\tilde{p}_\infty$, the reduced friction coefficients $\tilde{\mu}$, $\tilde{\mu}_\mathrm{a}$ and $\tilde{\mu}_0$ as functions of the dimensionless sliding velocity ζ, for different values of the reduced energy of adhesion Γ. At low velocity (i.e., for $\zeta < 10^{-2}$), the system is in the small-scale viscoelasticity regime; indeed, friction is governed by the adhesion hysteresis, therefore $\tilde{\mu} \simeq \tilde{\mu}_\mathrm{a}$, in agreement with Eq. (3.38). As expected, increasing Γ leads to significantly higher values of $\tilde{\mu}$, as the term $G_1 - G_2$ in Eq. (3.40) increases. At intermediate velocities (i.e., for $10^{-2} < \zeta < 1$), also bulk dissipation occurs; importantly, the figure clearly indicates that $\tilde{\mu} \gg \tilde{\mu}_\mathrm{a} + \tilde{\mu}_0$, i.e., that the contributions to friction of the small-scale and of the bulk (i.e. large-scale) viscoelasticity cannot be linearly separated. This is a key result: adhesion increases the contact area, hence, the volume where viscoelastic losses take place, and, in turn, increases the bulk viscoelastic dissipation [see also Fig. 3.2(a)]. At higher velocity (i.e., for $1 < \zeta < 10$), this effect is even clearer, as $\tilde{\mu_a} < 0$ while $\tilde{\mu} > \tilde{\mu_0} > 0$. Indeed, when bulk dissipation is involved in the frictional response, $\tilde{\mu_a}$ is a qualitative estimation of the sole contribution to friction ascribable to the contact edges, which can also become negative when more energy is recovered during

sliding in closing the leading edge compared to that required to open the trailing one (i.e., $G_2 > G_1$). At very high velocity, the contact edges behave almost elastically (glassy region), thus the small-scale viscoelastic energy dissipation vanishes, and the great majority of energy dissipation occurs in the bulk of the material.

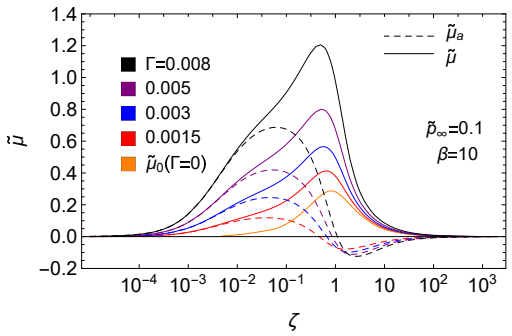

Figure 3.10: The reduced viscoelastic friction coefficient $\tilde{\mu} = \mu/\tilde{\Lambda}$ (solid lines) as a function of the dimensionless sliding velocity ζ, for different values of the reduced energy of adhesion Γ under load controlled conditions. In the same figure, we also show the reduced adhesive friction coefficient $\tilde{\mu}_\mathrm{a}$ (dashed line), and the reduced friction coefficient $\tilde{\mu}_0$ corresponding to adhesiveless conditions (solid black line).

Fig. 3.12(a, b) shows the reduced friction coefficient $\tilde{\mu}$ versus the sliding dimensionless speed ζ for different values of the dimensionless remote pressure $\tilde{p}_\infty$ and the dimensionless penetration $\tilde{\Delta}$, respectively. The specific dependence of the friction coefficient on $\tilde{\Delta}$ and $\tilde{p}_\infty$ is affected by different mechanisms, related to both the adhesion hysteresis and the bulk viscoelasticity. At relatively high velocity (i.e., for $\zeta > 1$), friction is mostly governed by bulk dissipation, and the curve μ vs. ζ roughly depends on the size of the contact area a, as discussed in Refs. [43, 103, 131]. The first effect is that, since the excitation frequency in the bulk material can be estimated as $\omega \approx 2\pi v/a = 2\pi\zeta/(\tilde{a}\tau)$, and the viscoelastic dissipation takes its maximum at $\omega \approx 1/\tau$, the dimensionless sliding velocity ζ_0 associated to the μ peak roughly depends on the value of a as $\zeta_0 \approx \tilde{a}/2\pi$. Indeed, Figs. 3.12(a, b) show that increasing $\tilde{\Delta}$ or $\tilde{p}_\infty$ (i.e., increasing a) has the effect of shifting the friction peak location ζ_0 at higher values, for both adhesive and adhesiveless contacts. Secondly, dimensional arguments [103] show that the friction coefficient can be roughly estimated as $\mu \approx (\delta/2a)\,\mathrm{Im}[E(\omega)]/\,|E(\omega)|$, with $\delta = \Lambda\,(1 - \cos ka) \approx \Lambda(ka)^2/2$ being the local indenter penetration. Figs. 3.12(a, b) show, indeed, that increasing $\tilde{\Delta}$ or $\tilde{p}_\infty$ (i.e., increasing a) leads to higher peak values for μ. However, these arguments only consider the bulk dissipation. On the contrary, at low velocities (i.e., for $\zeta < 10^{-2}$), most of the contribution to friction arises from adhesion hysteresis ($\mu \approx \mu_\mathrm{a}$). Therefore, the reduction of μ reported under these condition as $\tilde{\Delta}$ and $\tilde{p}_\infty$ are increased is immediately explained recalling that, in Eq. (3.40), the term $G_1 - G_2$ only depends on ζ (see also Fig. 3.7 and Chapter 5). Hence, given the value of ζ, the adhesive friction coefficient must decrease as $\tilde{p}_\infty$ is increased, in agreement with Refs. [120] and [37]. Moreover, it is worth noticing, that under load controlled conditions [Fig. 3.10 and Fig. 3.12(a)],

the μ vs. ζ curves present a hump localized at the value of ζ corresponding to the maximum of μ_a, followed by a peak at higher velocity, where maximum bulk dissipation occurs.

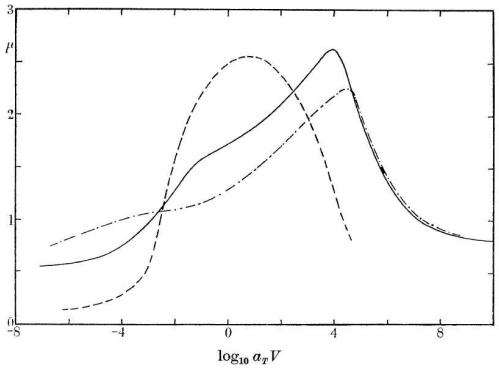

Figure 3.11: The measured friction coefficient μ as a function of the dimensionless sliding velocity taken from Ref [27] for styrene-butadiene rubber sliding against three surfaces: smooth clean (dashed); rough clean (solid); rough dusted (dot-dashed). See [27] for further details.

In Figure 3.11, we report the experimental measurements provided by Grosch in [27] for sliding friction of rubber samples. Regardless of the numerical values, which depend on the specific rubber property and surface roughness parameters, Grosch's trends are in very good agreement with our numerical predictions. Notably, using a clean smooth surface (dashed line) as sliding counterpart, only adhesive friction occurs. Dealing with a clean rough surface (continuum line), both adhesive hysteresys and bulk viscoelasticity play a key role on μ; whereas, adhesion can be completely masked by introducing a fine poweder at the interface (dot-dashed line).

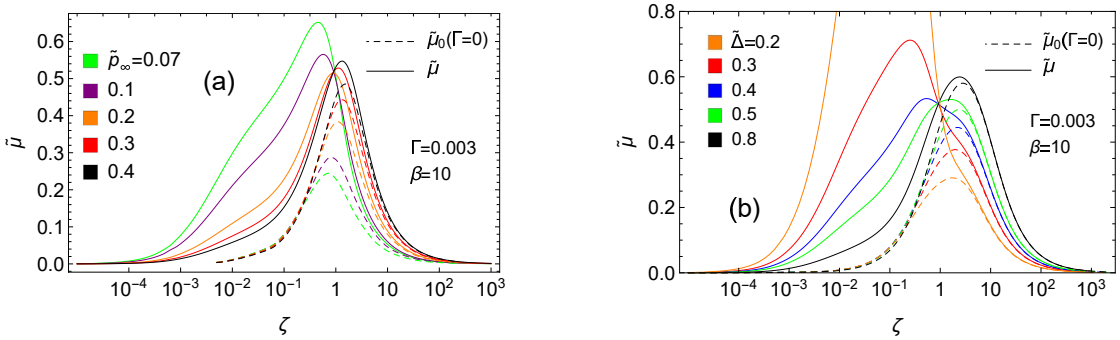

Figure 3.12: The reduced viscoelastic friction coefficient $\tilde{\mu} = \mu/\tilde{\Lambda}$ (solid lines) as function of the dimensionless sliding velocity ζ, under load controlled conditions (a) and displacement controlled conditions (b). In the same figure, we also show the reduced friction coefficient $\tilde{\mu}_0$ corresponding to adhesiveless conditions (dashed line).

Under displacement controlled conditions (i.e., fixed Δ), the behavior is slightly different and curves might, instead, exhibit ad adhesive friction peak followed by

a hump as the velocity is increased (see curves at $\tilde{\Delta} = 0.3$ and $\tilde{\Delta} = 0.4$). This follows from the fact that when the penetration is prescribed the contact area is much less dependent on the effective bulk stiffness and in turn on the sliding velocity. Moreover, the contact length is much closer to what is found in the case of adhesiveless viscoelastic contact [see also Fig. 3.2(a)]. Therefore, in this case, at high velocity (i.e., for $\zeta > 1$), the effect of adhesion is very poor, and $\tilde{\mu} \approx \tilde{\mu}_0$. Nonetheless, at low velocity, adhesion plays a key role as $\mu \approx \mu_a$. Note that under fixed penetration the friction coefficient tends to diverge at intermediate velocity (for $\tilde{\Delta} \lesssim 0.3$) since the remote pressure tends to vanish and even become negative (as shown in the next section) while the lateral stress remains finite.

The overall frictional behavior under negative $\tilde{p}_\infty$ is shown in Fig. 3.13, where the trends of the dimensionless lateral remote stress $\tilde{\sigma}_{fr}$ and of the associated adhesive contribution $\tilde{\sigma}_a = 2\left(G_1 - G_2\right) / \left(\lambda \tilde{\Lambda} E_0^*\right)$ are shown as function of ζ. In this case, the effect of the bulk viscoelasticity on the lateral force is less significant and the adhesive friction stress provides a good estimation of the actual lateral stress (observe that at negative loads we always observe $G_1 - G_2 > 0$, as shown in Fig. (3.7)). At low velocity, the lateral stress $\tilde{\sigma}_{fr} \simeq \tilde{\sigma}_a$ and is therefore independent on $\tilde{p}_\infty$, in agreement with the previous discussion. At quite high velocity velocity instead, increasing the tensile normal stress $|p_\infty|$ implies a slight decrease of $\tilde{\sigma}_{fr}$, ascribable to the smaller size of contact area leading in turn to a smaller amount of bulk dissipation.

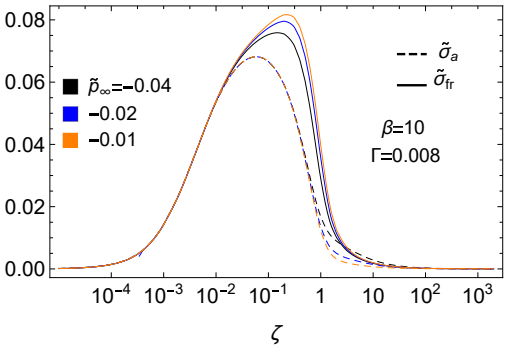

Figure 3.13: The frictional behavior under negative dimensionless normal remote pressure $\tilde{p}_\infty$ as function of the dimensionless sliding velocity ζ. Solid lines represent the dimensionless remote lateral stress $\tilde{\sigma}_{fr}$. Dashed lines represent the dimensionless adhesive lateral stress $\tilde{\sigma}_a = 2\left(G_1 - G_2\right) / \left(\lambda \tilde{\Lambda} E_0^*\right)$.

3.7 Adhesive properties of the contact

In this section the adhesive properties of the contact are investigated in terms of toughness T (i.e. amount of work required to separate the contacting bodies) and adhesive strength (i.e. pull-off remote pressure p_{out}) of the contact interface. In

dimensionless terms the toughness $\tilde{T} = 2\left(1-\nu^2\right)T/\left(\Lambda^2 E_0\right)$ is defined as

$$\tilde{T} = 2\pi \int_{\tilde{\Delta}_0}^{\tilde{\Delta}_{\text{out}}} \tilde{p}_\infty(\tilde{\Delta}) d\tilde{\Delta} \tag{3.41}$$

where $\tilde{\Delta}_{\text{out}}$ is the dimensionless penetration at which pull-off occurs, $\tilde{\Delta}_0$ is the dimensionless penetration corresponding to $\tilde{p}_\infty = 0$. Notably, both $\tilde{\Delta}_{\text{out}}$ and $\tilde{\Delta}_0$ depend on the dimensionless sliding velocity ζ. In Fig. 3.14(a) the quantity $\tilde{T}$ is plotted against ζ for different values of the dimensionless adhesive parameter Γ. Instead, Fig. 3.14(b) provides a complete adhesion-strength map: the iso-ζ and iso-Γ curves are shown in the $|\tilde{p}_{\text{out}}|$ vs. $|\tilde{\Delta}_{\text{out}}|$ plane. In agreement with the experimental observations reported in Ref. [32], we note that in the range of velocity where small-scale viscoelasticity effects governs the contact behavior (i.e., $10^{-2} < \zeta < 10^{-1}$), both the adhesive toughness and the adhesive strength take their maximum values. Interestingly, the trend of $|\tilde{p}_{\text{out}}|$ vs. ζ is non-monotonic; notably, at very high velocity, due to the glassy stiff behavior of the material, the contact interface is able to withstand high tensile loads (i.e. large pull-off pressures). However, in the same conditions the system's toughness $\tilde{T}$ is very low as $\tilde{\Delta}_{\text{out}}$ drops. Interestingly, a similar limiting behavior is reported in the case of thin elastic adhesives, where the material confinement induced by the rigid substrate leads very high contact stiffness [47,48]. In order to provide deeper insights on the origin of adhesion enhancement, Fig. 3.14 (c) compares the pull-off remote stress $|\tilde{p}_{\text{out}}|$ with the quantity $\left|(\tilde{p}_{off})_0\right|$, i.e., the pull-off pressure calculated for a purely elastic material with elastic modulus $|E\left(\omega = \zeta/\tau\right)|$. We observe that $|(\tilde{p}_{\text{out}})_0|$ monotonically increases because of the monotonic material stiffening occurring as ζ is increased. However, the pull-off load $|\tilde{p}_{\text{out}}|$ rises up well above $|(\tilde{p}_{\text{out}})_0|$, already at very low velocity, confirming that at low velocity the pull-off enhancement is triggered by the small-scale viscoelastic losses.

In Fig. 3.15 the equilibrium diagrams $\tilde{p}_\infty$ vs. $\tilde{a}$ and $\tilde{p}_\infty$ vs. $\tilde{\Delta}$ are shown, for different values of ζ. The curves presents a qualitatively similar shape compared to the elastic adhesive case [37]. We observe that, for a fixed value of $\tilde{\Delta}$, $\tilde{p}_\infty$ non-monotonically depends on ζ (see also Fig. 3.16). Moreover, at low velocities (i.e., for $\zeta < 0.1 = 0.001, \zeta = 0.01, \zeta = 0.1$) the maximum positve load, i.e., the so called *snap into full-contact* pressure, decreases as ζ is increased, as a consequence of the viscoelasticity-induced enhanced adhesion. The overall dependence of the *snap into full-contact* pressure p_{IN} from the sliding velocity is shown in Fig. 3.14(d). Note that the scenario is reversed at high velocities, as larger values of ζ entail a strong viscoelastic material stiffening, leading to very large values of p_{IN}. The diagrams in Fig. 3.15 also report unstable branches. Specifically, for $\tilde{\Delta} \to 1$ the slope of the $\tilde{p}_\infty$ vs. $\tilde{\Delta}$ curve is negative, i.e., under these conditions the system is unstable and jumps into full-contact, analogously to the elastic case, as discussed in [37]. Notably, a contact solutions is stable when the second variation of the virtual work of internal stresses with respect to the contact coordinates at the equilibrium point is positive at both contact edges (see Chapter 1). This condition is not satisfied in points on the dashed lines in Fig. 3.15 (c).

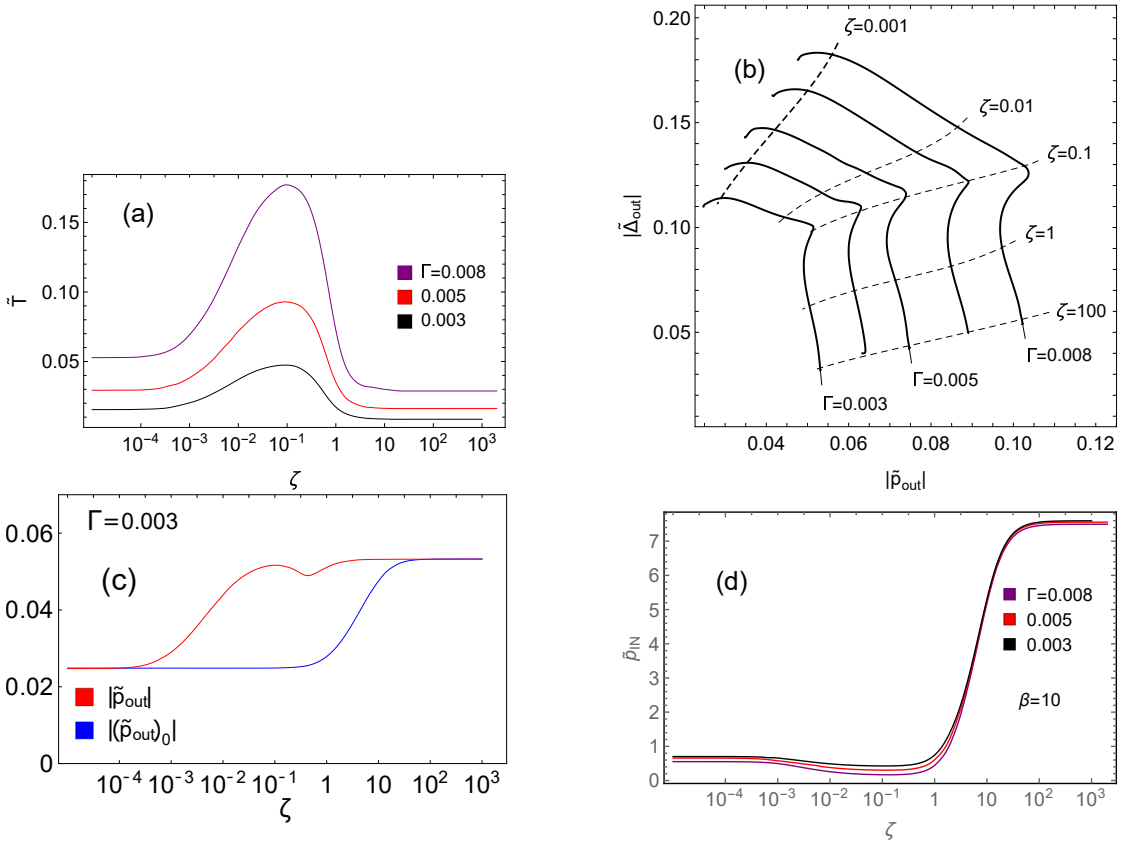

Figure 3.14: (a): The dimensionless work needed to cause detachment $\tilde{T}$ as a function of the dimensionless sliding velocity ζ, for different values of the reduced energy of adhesion Γ. (b): iso-ζ (dashed lines) and iso-Γ (solid lines) curves in the $|\tilde{\Delta}_{\rm out}|$ vs $|\tilde{p}_{\rm out}|$ plane, being $\tilde{p}_{\rm out}$ the dimensionless pull-off remote pressure and $\tilde{\Delta}_{\rm out}$ the dimensionless penetration at which the pull-off occurs. (c) The dimensionless pull-off remote pressure $|\tilde{p}_{\rm out}|$ and the elastic dimensionless pull-off remote pressure $|(\tilde{p}_{\rm out})_0|$ calculated assuming a velocity dependent Young modulus $|E(\omega = \zeta/\tau)|$, as function of ζ. (d) The dimensionless snap into full-contact remote pressure $\tilde{p}_{IN}$ as function of ζ for different values of Γ. Results are shown for $\beta = 10$.

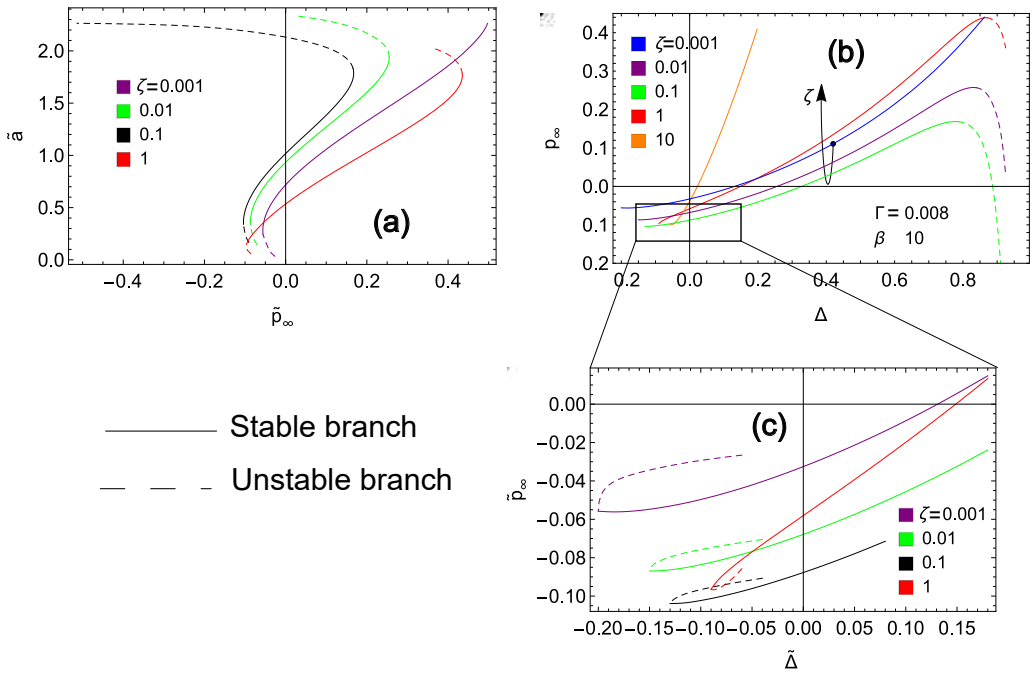

Figure 3.15: Equilibrium diagrams including stable (solid line) and unstable (dashed line) branches, for different values of the dimensionless sliding velocity ζ. (a) The dimensionless contact half-length $\tilde{a}$ as function of dimensionless remote pressure $\tilde{p}_\infty$. (b) The dimensionless remote pressure $\tilde{p}_\infty$ as a function of the dimensionless penetration $\tilde{\Delta}$. (c) Magnification of (b). Results are shown for $\beta = 10$, $\Gamma = 0.008$.

In Fig.3.16 (a) we report the overall dependence of $\tilde{p}_\infty$ from ζ under fixed (positive) penetration. The specular curve of $\tilde{\Delta}$ vs. ζ under constant (positive) $\tilde{p}_\infty$ is presented in Fig. 3.16 (b). The trends clearly reflect the adhesion enhancement occurring at low and intermediate velocity: under constant load the indenter sinks inside the rubber substrate (i.e., $\tilde{\Delta}$ increases) and, analogously, under constant displacement the indenter is pulled by a tensile force despite the penetration is positive for intermediate values of ζ. The reported behavior at the low and high velocity limits instead depends on the different effective stiffness of the material.

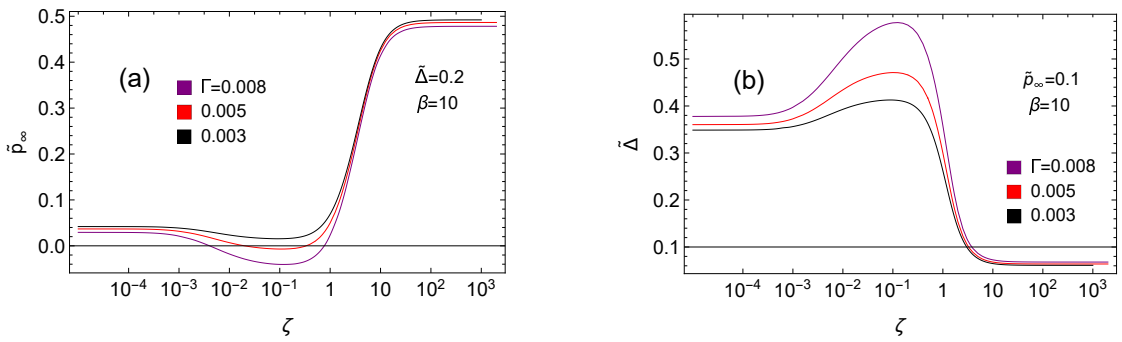

Figure 3.16: (a): The dimensionless remote pressure $\tilde{p}_\infty$ as function of the dimensionless velocity ζ under constant penetration $\tilde{\Delta}$ for different values of the reduced energy of adhesion Γ. (b) The dimensionless penetration $\tilde{\Delta}$ as function of the dimensionless velocity ζ under constant dimensionless remote pressure $\tilde{p}_\infty$ for different values of the reduced energy of adhesion Γ.

3.8 The effect of the process zone's length

As mentioned in Sec. 3.1 the quantity δA in Eq. (3.12) represents a characteristic size of the problem. Fig. 3.17 investigates its effect on the predicted contact solutions. Specifically, the reduced energy release rates $G_1/\Delta\gamma$ and $G_2/\Delta\gamma$ at the contact trailing and leading edges are reported as function of the dimensionless speed, for different values of $\delta\tilde{l}_1$ and $\delta\tilde{l}_2$ set in Eqs. (3.25). A more detailed discussion on how these result are related to the asymptotic local stress and displacement fields in the small-scale viscoelastic regime and on the physical meaning of the characteristic length is provided in Chapter 5. Importantly, the figure shows that the contact solution is not affected by the value of the parameter for a wide range of sliding velocities (i.e., for $\zeta \gtrsim 0.1$), and only the small-scale viscoealstic regime is affected. A qualitative explanation is that the assumption of infinitely short range adhesive forces results into a paradox, i.e., that the material is excited at infinitely high frequencies close to the crack tip, no matter how low the velocity is. Therefore small-scale viscoealstic effects are always present at distance from the crack's tip of order $\sim v\tau$ (as shown in Chapter 5). As a consequence, if, for instance, one sets $\delta l \simeq v\tau$, the low velocity limit elastic solution can never be recovered. Consistently, the figure indicates that, given a fixed value of $\delta\tilde{l}$, the low velocity limit, i.e., $G = \Delta\gamma$, is obtained for $\zeta \lesssim 0.01\delta\tilde{l}$. Notably, close to the opening and closing crack tips, the materials response is elastic (glassy), and therefore the crack opening or closing displacement gap at small distance d from the tip can be written as

$$\Delta u(x) = K_I/E^*_\infty\sqrt{8/\pi d} \tag{3.42}$$

and the local stress presents the square root singularity

$$\sigma(x) = \frac{K_I}{\sqrt{2\pi d}} \tag{3.43}$$

Therefore, taking the limit $\delta A \to 0$, Eqs. (3.42, 3.43) can be used in the closure equation (3.12), which therefore in this case reads as

$$\frac{K_I^2}{2E_\infty^*} = \Delta\gamma \tag{3.44}$$

In the small-scale viscoelastic regime, this leads to an incorrect result, i.e., that the energy release rates are velocity-independent and $G_1 = (E_\infty/E_0)\,\Delta\gamma$ and $G_2 = (E_0/E_\infty)\,\Delta\gamma$. This corresponds to the black lines shown in Fig. 3.17. Indeed, the real response of the system is correctly predicted when $\delta\tilde{l}_1$ and $\delta\tilde{l}_2$ are small but finite quantities, whose order of magnitude resembles that of the so-called process zone [69, 132, 133]. When the parameters $\delta\tilde{l}_1$ and $\delta\tilde{l}_2$ are correctly set in this way, Eqs. (3.42, 3.43) no longer apply in the small-scale viscoelastic regime for distances from the crack tips of order $\delta\tilde{l}_1$ and $\delta\tilde{l}_2$. This is due to the presence of the pressure peak shown in Fig.3.3 at the leading edge and to the trumpet displacement shape shown in Fig. 3.5 at the trailing edge, which are localized very close to the crack tips. Therefore, Eq. (3.44) only applies at relatively high velocity.

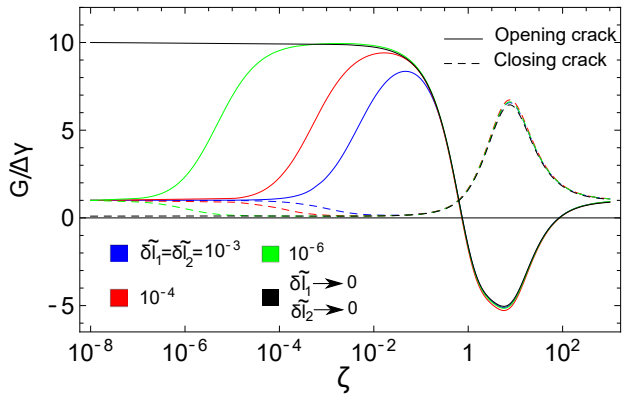

Figure 3.17: The reduced energy release rates at the trailing (solid lines) and leading (dashed lines) contact edges as function of the dimensionless sliding velocity ζ predicted by setting different values of the dimensionless parameters $\delta\tilde{l}_1$ and $\delta\tilde{l}_2$ in Eq. (3.25). Taking the limit $\delta\tilde{l}_1 \to 0$ and $\delta\tilde{l}_2 \to 0$ (black line) is equivalent to enforce the closure equation in the form expressed by Eq. (3.44). Results refer to $\beta = 10$, $\tilde{\Delta} = 0.4$, $\Gamma = 0.003$.

3.9 Conclusion

In this chapter, we presented a novel theory of adhesive viscoelastic contact mechanics in the presence of relative sliding or rolling motion between the viscoelastic solid and the rigid rough indenter. We found that close to the contact edges, the viscoelastic behavior is governed by small-scale viscoelasticity. In this case, the local excitation frequency depends on the ratio between the sliding speed at the leading and trailing edges (closing and opening cracks) and the corresponding crack tip radii. In the bulk of the material, instead, viscoelastic hysteresis

occurs at an excitation frequency given by the ratio between the sliding speed and the macroscopic contact size. As a consequence, the overall contact response can be governed by either the small- and large-scale viscoelasticity, depending on the specific value of the sliding velocity. Indeed, in agreement with the experiments [28, 32], we have shown that at relatively low sliding velocity the bulk of the material behaves as a soft elastic body, and the interaction between interfacial adhesion and small-scale viscoelasticity leads to an increase of the contact area, mostly localized at the trailing edge of the contact, and to a strong enhancement of the pull-off load. Small-scale viscoelasticity induces a different adhesive response of the trailing and leading edges, whose difference is mostly responsible of the overall frictional response of the contact. At intermediate velocities, bulk viscoelasticity and local viscoelasticity coexist, leading to a strong increase of friction compared to the corresponding adhesiveless contact case. This peculiar result is in perfect agreement with the observations made by Grosch on rubber adhesive friction [27]. The present theory also allows to quantify the energy release rates G_1 and G_2 (at the trailing and leading edge, respectively) as functions of the sliding velocity. A detailed analysis of these trends has shown that, because of the finiteness of the contact area, G_1 and G_2 follow a non-monotonic trend, which may also differ from the simple bell-shaped curve depending on load conditions and on the relative interplay between small-scale and bulk viscoelasticity.

Chapter 4

Enhancement of adhesion strength in viscoelastic unsteady contacts

The viscoelastic response of rubbery-like material is often identified as a major source of adhesion enhancement. Chapter 3 clearly demonstrated that this is a pivotal aspect of steady-state sliding contacts, in which the increase of the pull-off force and the contact area enlargement result from viscoelastic losses localized at the contact trailing edge. Importantly, this phenomenon also governs unsteady contacts when the relative motion consists of dynamic normal loading. Countless experimental studies (see for instance [33–36]) have shown that detaching a rigid indenter from a viscoelastic substrate by applying a finite normal velocity might require a force significantly higher compared to predictions of theoretical elastic models (e.g., the JKR model). Viscoelasticity allows, in fact, to properly tune and regulate adhesion, with fundamental implications in all those engineering applications in which objects must be picked, moved, and released through adhesive forces. However, the overall contact behavior and, in turn, the pull-off force value, are affected by the entire loading time-history and the overall effect of viscoelasticity on the effective adhesion in unsteady contacts is a complex phenomenon, not fully understood yet. Indeed, lab tests are often devoted at investigating the effect of different physical variables and enforced time loading histories. For instance, loading-unloading cycles are carried at different velocities and by changing the amplitude of the cycle [36, 134, 136]. Similarly, the effect of the dwell time before retraction is investigated [137, 138], as well as the effect of the applied preload [34, 139]. Dynamic analyses are often devoted to investigating the contact quantities under oscillating force or displacement as function of the applied frequency [140, 141], or by superimposing micro-vibrations and a mean velocity of retraction [119]. In all of these experimental investigations, the observed contact behavior significantly deviate from the JKR predictions: the aforementioned increase of the effective adhesion strength is associated with significative hysteresis in cyclic oscillations and in some cases adhesion can be even masked (see for instance [119]). Also in this class of unsteady contacts, most of existing

theoretical and numerical studies are based on the small-scale viscoelasticity assumption. The latter is often exploited by replacing the adhesive energy $\Delta\gamma$ in the JKR equilibrium relations with a velocity-dependent term, which is fitted from experimental data [36, 67] or assumed as input parameter in order to account for local viscoelastic losses [63, 64]. However, neglecting the bulk viscoelasticity might prevent to tackle many of the characteristic phenomena. In the present Chapter, the energy formulation presented in Chapter 3 is generalized to general unsteady conditions (dynamic loading). Hence, in the present analysis, we formally derive a general Griffith-like criterion for viscoelastic contacts and unsteady crack propagation in hysteretic materials. We derive the energy balance by relying on the D'Alembert virtual work principle: the variation of adhesion energy due to a virtual change of the contact radius (the Lagrangian coordinate) must be precisely balanced by the virtual work of internal stresses. Notably, in unsteady conditions, the virtual work formulation must properly account for the time dependency of all the contact quantities. Our findings are in perfect agreement with experimental results and Lennard-Jones based numerical calculations [65, 66, 135, 142], and clearly indicate that viscoelasticity plays a major role in affecting the adhesion enhancement depending on the specific loading-history. Our theoretical approach also provides very profound insights into the physical mechanisms governing experimentally observed phenomena such as the enhancement of pull-off force during fast retraction [33–36], the hysteresis during the approach-retraction cycle [36, 136], and effective contact stiffness during high frequency oscillations [140, 141].

4.1 Formulation

We consider the adhesive contact between a linear viscoelastic half-space and a rigid sphere of radius R subjected to a time-varying rigid normal displacement $u_0(t)$, as shown in Fig 4.1. According to [30, 128] and to the discussion presented in Chapter 2, under general unsteady conditions the normal displacement field $u(\mathbf{x}, t)$ of the viscoelastic half-space surface is given by

$$u(\mathbf{x},t) = J(0)\int dx_1^2 \mathcal{G}(\mathbf{x}-\mathbf{x}_1)\sigma(\mathbf{x}_1,t) + \int_{-\infty}^{t} dt_1 \dot{J}(t-t_1)\int dx_1^2 \mathcal{G}(\mathbf{x}-\mathbf{x}_1)\sigma(\mathbf{x}_1,t_1) \tag{4.1}$$

where $\mathbf{x}$ is the in-plane position vector (see Fig (4.1)), t is the time variable, $\sigma(\mathbf{x}, t)$ is the interfacial normal stress distribution, $J(t)$ is the viscoelastic creep function, and $\mathcal{G}(\mathbf{x}) = (1-\nu^2)|\mathbf{x}|^{-1}/\pi$. Since we only consider the normal approach/retraction of the sphere, the problem at hand is axisymmetric, i.e., at each time step t all quantities depend only on the distance $r = |\mathbf{x}|$ from the contact center (see Fig. 4.1). This is of course a mixed boundary value problem: under the assumption of infinitely short range interfacial adhesive interactions, outside the circular contact region of radius $a(t)$ the surface stresses must vanish, i.e. $\sigma(r, t) = 0$ for $r > a(t)$, whilst within the contact region the surface displacement field is prescribed, i.e. $u(r, t) = s(r, t)$ for $r \leq a(t)$, with $s(r, t) = u_0(t) + r^2/(2R)$ being the spherical indenter surface at time t. We also define the local interfacial gap as $g(r, t) =$

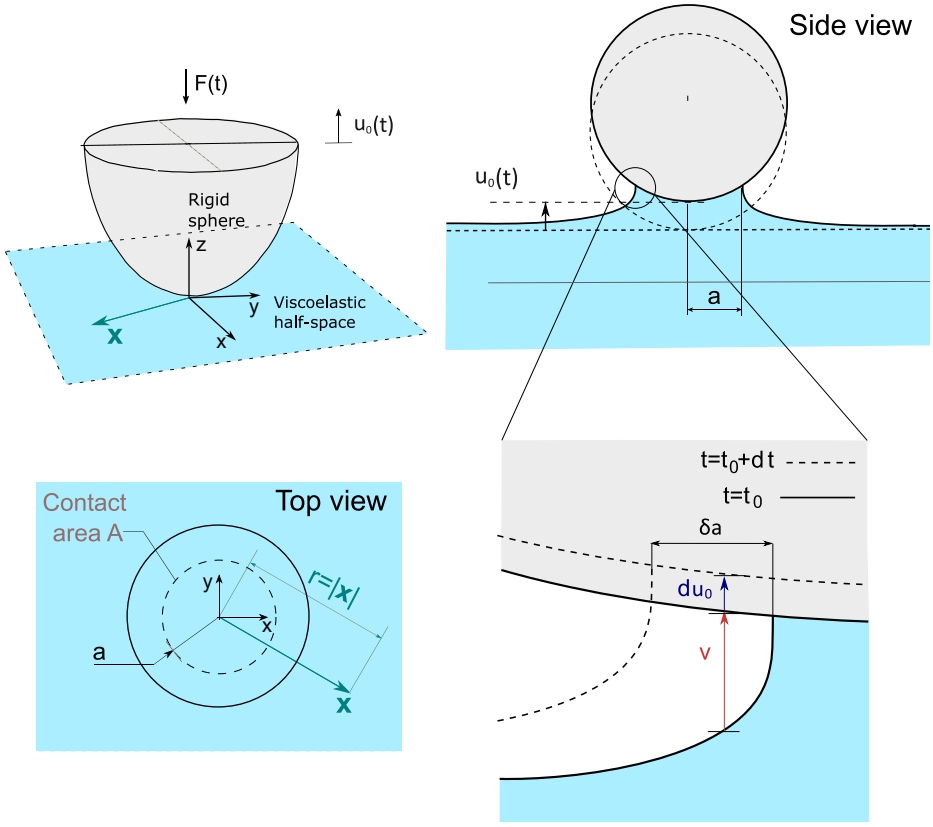

Figure 4.1: The schematic of the adhesive contact between a viscoelastic half-space and a rigid sphere, with time-varying normal rigid displacement $u_0(t)$. The inset represents the virtual component v of the local displacement $v + du_0$ close to the contact edge associated with the contact area variation δa and indenter rigid displacement du_0.

$s(r,t) - u(r,t)$, so that $g(r,t) = 0$ for $r \leq a(t)$. Note that, given a time-history of the rigid normal displacement $u_0(t)$, Eq. (4.1) cannot be solved as the time-dependent contact radius $a(t)$ is unknown, and an additional closure equation is needed to solve the problem. Of course also in this class of unsteady contacts, in adhesiveless conditions the closure condition is simply that the interfacial contact stress must vanish at the boundary of the contact area; for adhesive contacts instead, an energy based condition should be identified. In virtue of the principle of virtual works, the equilibrium configuration at time t requires that the work of external forces δL_E due to an admissible virtual displacements field equates the work of internal stresses δL_I due to the corresponding compatible virtual strain field. Since the virtual displacements field $\delta\mathbf{v}(r,z,t)$ must satisfy the boundary conditions at time t (i.e., the kinematic constraints), we have $\delta\mathbf{v}(x,z,t) = 0$ within the contact region, i.e. where the time-dependent constraint $u(r,t) = s(r,t)$ is prescribed. Then, neglecting body forces, at equilibrium we have

$$\delta L_I = \int_W \sigma_{ij}\delta\varepsilon_{ij}dV = \int_{\partial W} \sigma \cdot \delta\mathbf{v}dA = \delta L_E \tag{4.2}$$

for any admissible virtual displacement $\delta\mathbf{v}$ and its associated internal strain tensor $\delta\varepsilon_{ij}$, where σ is the surface stress field, and σ_{ij} is the internal stress tensor.

For the contact problem represented in Fig. 4.1, we assume a virtual variation (i.e., at fixed time t) of the contact configuration so that the contact radius increases from $a(t)$ to $a(t) + \delta a$. Consequently, the asymptotic surface displacements at the contact edge [i.e., for $|r - a(t)| \ll a(t)$] changes by the quantity $v^-(r) = g[r \geq a(t), t]$. This can be described by the virtual displacement process $v(r,\eta) = v^-(r)H(\eta)$, where $H(\eta)$ is the unit step function, and η is the process parameter spanning the entire real axis. Therefore, at each step of the process, the virtual normal displacement $\delta v(r,\eta)$ obeys the equation

$$\delta v(r,\eta) = \frac{\partial v}{\partial \eta}d\eta = v^-(r)\delta(\eta)d\eta \tag{4.3}$$

where $\delta(\eta)$ is the Dirac delta function. Similarly the asymptotic stress distribution σ_{a} close to the boundary of the contact area [i.e., for $|a(t) - r| \ll a(t)$] has the form $\sigma_{\mathrm{a}}[a(t) - r, t] = \sigma[r < a(t), t]$. Therefore, during the virtual displacement process governed by the parameter η, the corresponding asymptotic surface stresses are given by

$$\sigma(r,\eta) = \sigma^+(r)H(\eta) \tag{4.4}$$

where $\sigma^+(r) = \sigma_{\mathrm{a}}[a(t) + \delta a - r, t]$. It follows that during the entire η-governed process, the total virtual work $(\delta L_I)_{\mathrm{T}}$ of internal stresses due to the contact radius virtual variation from $a(t)$ to $a(t) + \delta a$ can be calculated as

$$(\delta L_I)_{\mathrm{T}} = 2\pi \int_a^{a+\delta a} rdr \int_{-\infty}^{\infty} d\eta\sigma(r,\eta)\frac{\partial v}{\partial \eta} = 2\pi \int_a^{a+\delta a} rdr\sigma^+(r)\, v^-(r) \int_{-\infty}^{\infty} d\eta H(\eta)\,\delta(\eta) \tag{4.5}$$

and, recalling that $\int_{-\infty}^{\infty} d\eta H(\eta)\,\delta(\eta) = 1/2$, we finally get

$$(\delta L_I)_{\mathrm{T}} = \pi a \int_a^{a+\delta a} dr \sigma^+(r)\, v^-(r) \tag{4.6}$$

The virtual (external) work of adhesive forces during the entire displacement process is instead

$$(\delta L_E)_{\mathrm{T}} = 2\pi \Delta\gamma a \delta a \tag{4.7}$$

Thus, exploiting Eq. (4.2) at each single step of the displacement process, the energy balance gives

$$(\delta L_I)_{\mathrm{T}} = (\delta L_E)_{\mathrm{T}} \tag{4.8}$$

which, using Eqs. (4.6,4.7), can be rewritten as

$$\frac{1}{2\delta a} \int_a^{a+\delta a} dr \sigma^+(r) v^-(r) = \Delta\gamma \tag{4.9}$$

Eq. (4.9) represents the generalization of the Griffith fracture criterion for unsteady contacts and holds true for both elastic and viscoelastic materials. The positive quantity δa should be chosen of the same order of magnitude of the the so-called 'process zone' at the contact edges [129]. Specific cases, such as thin pressure-sensitive membrane [143, 144], might require replacing in Eq. (4.9) the adhesion energy $\Delta\gamma$ with a modified energy of adhesion which depends on both the propagation speed of the crack tip and temperature of the process zone. The quantity δa or equivalently the length of the process zone is an additional (short) length scale, whose choice does not affects the physical qualitative behavior of the viscoelastic contact problem at hand, as it only shifts the frequency of the local excitation occurring close to the boundary of the contact, as shown in Chapter 3. Notably, Eq. 4.9 is formally the same as that derived in Chapter 3 for steady sliding contacts following a different argument.

4.2 Numerical implementation

In this section, we describe the numerical procedure employed to solve Eq. (4.1). We refer to the viscoelastic creep's function with single relaxation time given by Eq. (4.20). In this case, taking the time derivative of Eq. (4.1) leads to

$$\dot{u}(\mathbf{x},t) = \frac{1}{E_\infty} \int dx_1^2 \mathcal{G}(\mathbf{x}-\mathbf{x}_1)\dot{\sigma}(\mathbf{x}_1,t) \tag{4.10}$$

$$- \frac{1}{\tau^2 E_1} \exp\left(-\frac{t}{\tau}\right) \int_{-\infty}^{t} dt_1 \exp\left(\frac{t_1}{\tau}\right) \int dx_1^2 \mathcal{G}(\mathbf{x}-\mathbf{x}_1)\sigma(\mathbf{x}_1,t_1) \tag{4.11}$$

$$+ \frac{1}{\tau E_1} \int dx_1^2 \mathcal{G}(\mathbf{x}-\mathbf{x}_1)\sigma(\mathbf{x}_1,t)$$

Using again Eqs. (4.1, 4.20) yields the following time-differential equation:

$$\dot{u}(\mathbf{x},t)=\frac{1}{E_\infty}\int dx_1^2\mathcal{G}(\mathbf{x}-\mathbf{x}_1)\dot{\sigma}(\mathbf{x}_1,t)+\frac{1}{\tau E_0}\int dx_1^2\mathcal{G}(\mathbf{x}-\mathbf{x}_1)\sigma(\mathbf{x}_1,t)-\frac{u(\mathbf{x},t)}{\tau} \tag{4.12}$$

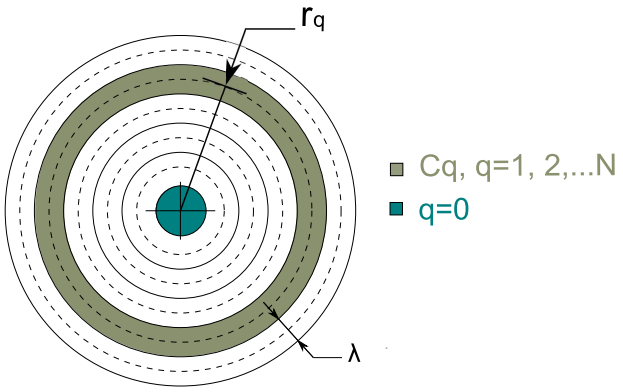

Figure 4.2: The discretization of spatial domain for the numerical resolution of Eq. 4.1

which can be solved avoiding integration over the whole time history. Using a numerical quadrature rule and exploiting the axisymmetric nature of the problem, the spatial domain is discretized as shown in Fig. 4.2 into N circular annulus C_q of constant width λ (with $\lambda/a \ll 1$) placed at radii $r_q = q\lambda + \lambda/2$, and a circle C_0 of radius λ placed at $r_0 = 0$. Each area is subjected to uniform stress $\sigma_q(t) = \sigma(r_q, t)$, $q = 0, 1, ...N$, and Eq.4.12 can be rewritten as

$$\dot{u}_h(t) = \dot{u}(r_h,t)=\frac{1}{E_\infty}\sum_{q=0}^{N}\dot{\sigma}_q(t)\int_{C_q}dx_1^2\mathcal{G}(\mathbf{x}-\mathbf{x}_1)+ \tag{4.13}$$

$$+\frac{1}{\tau E_0}\sum_{q=0}^{N}\sigma_q(t)\int_{C_q}dx_1^2\mathcal{G}(\mathbf{x}-\mathbf{x}_1)-\frac{u_h(t)}{\tau} \tag{4.14}$$

where $\int_{C_q} dx_1^2\mathcal{G}(\mathbf{x}-\mathbf{x}_1) = \tilde{\mathcal{G}}(r_h, r_q) = \tilde{\mathcal{G}}_{hq}$ is an axisymmetric field that represents the surface displacement at radius r_h induced on an elastic half-space of unit modulus by a uniform unit stress acting over C_q. $\tilde{\mathcal{G}}_{hq}$ can be easily calculated. Indeed, following [145, 146], the quantity

$$\mathcal{K}(r_h,r_q)=\begin{cases}(1-\nu^2)\,\pi^{-1}4r_q\mathbf{E}(r_h/r_q), & r_h\le r_q\\ (1-\nu^2)\,\pi^{-1}4r_h\left[\mathbf{E}(r_q/r_h)\ -(1-(r_q/r_h)^2)\mathbf{K}(r_q/r_h)\right], & r_h>r_q\end{cases} \tag{4.15}$$

is the surface displacement at radius r_h resulting from a uniform unit stress field acting over a circle of radius r_q in the elastic problem (notably, a similar solution is given in Ref. [147] for uniform tangential stresses). In Eq. (4.15), $\mathbf{K}(\rho) = \int_0^{\pi/2} d\xi(1-\rho^2\sin^2(\xi))^{-1/2}$ and $\mathbf{E}(\rho) = \int_0^{\pi/2} d\xi(1-\rho^2\sin^2(\xi))^{1/2}$ are the complete elliptic integrals of the first and second kind, respectively. Thus, according to Fig. 4.2, $\tilde{\mathcal{G}}_{h0} = \mathcal{K}(r_h, \lambda)$ and, using the superposition of effects:

$$\tilde{\mathcal{G}}_{hq} = \mathcal{K}(r_h, r_q + \lambda/2) - \mathcal{K}(r_h, r_q - \lambda/2), \qquad q \neq 0 \tag{4.16}$$

The time domain is discretized with small steps ε, with $\varepsilon/\tau \ll 1$ and the discrete form of Eq. 4.12 can be written at time $t_k = k\varepsilon$ with $k = 1, 2, ...$Note that we define $u_h^k(r_h, t_k)$ and $\sigma_h^k = \sigma(r_h, t_k)$ and write

$$\left(1 + \frac{\varepsilon}{\tau}\right) u_h^k = \left(\frac{1}{E_\infty} + \frac{\varepsilon}{\tau E_0}\right) \sum_{q=0}^{N} \tilde{\mathcal{G}}_{hq} \sigma_q^k + A_h^{k-1} \tag{4.17}$$

where the quantity

$$A_h^k = u_h^k - \frac{1}{E_\infty} \sum_{q=0}^{N} \tilde{\mathcal{G}}_{hq} \sigma_q^k \tag{4.18}$$

has already been determined up to time t^{k-1}. The linear system of equations Eq. (4.17) allows to calculate, for any given value of the contact radius a, the stress distribution in the contact area and the displacement and gap distributions out of the contact area. Then, enforcing the energy balance condition Eq. (4.9) the equilibrium value $a^k = a\left(t^k\right)$ of the contact radius can be determined.

4.3 Contact parameters

Results are shown in terms of the following dimensionless quantities: $\tilde{p} = (1-\nu^2)\, p/(\pi E_0)$, $\tilde{u} = u/R$, $\tilde{\gamma} = (1-\nu^2)\,\Delta\gamma/(\pi E_0 R)$, $\tilde{F} = (1-\nu^2)\, F/(\pi E_0 R^2)$, $\tilde{V} = V\tau/R$, $\tilde{u}_0 = u_0/R$, $\tilde{\Delta} = \Delta/R$, $\tilde{t} = t/\tau$, $\tilde{r} = r/R$, $\tilde{\mathbf{x}} = \mathbf{x}/R$, $\tilde{J} = E_0 J$, $\tilde{a} = a/R$, with $p(r,t) = -\sigma(r,t)$ being the contact pressure, $\Delta = -u_0$ the contact penetration, and $F = \int d^2x p(r,t)$ the normal compressive applied force. In our calculations, we set $\delta\tilde{a} = 0.013$, $\tilde{\gamma} = 1.6 \times 10^{-4}$ (unless differently specified), and $E_\infty/E_0 = 10$. We also define the normal approach-retraction speed of the sphere as $V = |\dot{u}_0| = \left|\dot{\Delta}\right|$, where the superposed dot '$\cdot$' stands for the time derivative. Unless differently specified, V is the controlled parameter in our calculations. Moreover, the linear viscoelasticity of the material is modeled assuming a single relaxation-time τ and relaxation function given by

$$G(t) = \mathcal{H}(t)\left\{E_\infty + (E_0 - E_\infty)\left[1 - \exp\left(-\frac{t}{\tau}\right)\right]\right\} \tag{4.19}$$

also corresponding to the creep function given by

$$J(t) = \mathcal{H}(t)\left\{\frac{1}{E_\infty} + \left(\frac{1}{E_0} - \frac{1}{E_\infty}\right)\left[1 - \exp\left(-\frac{E_0}{E_\infty}\frac{t}{\tau}\right)\right]\right\} \tag{4.20}$$

where E_0, and E_∞ are the low-frequency and very high-frequency viscoelastic moduli of the material respectively.

4.4 Approach-retraction cycles

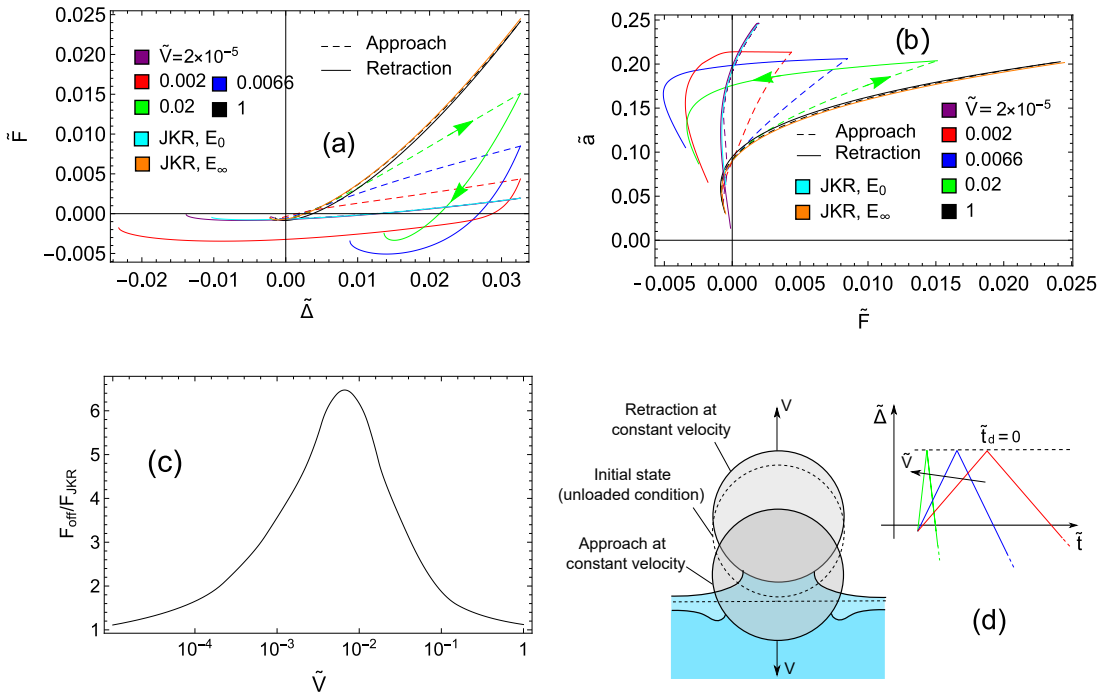

Figure 4.3: Approach-retraction cycles at different dimensionless sphere velocity $\tilde{V}$. Dashed and solid lines refer, respectively, to indentation and retraction, until pull-off occurs. (a) The dimensionless applied load $\tilde{F}$ vs. the dimensionless indentation depth $\tilde{\Delta}$. (b) The dimensionless contact radius $\tilde{a}$ vs. the dimensionless applied load $\tilde{F}$. The JKR elastic curves corresponding to moduli E_0 and E_∞ are reported for comparison. (c) The amplification ratio between the pull-off force F_{off} and the corresponding pull-off force F_{JKR} predicted by the JKR theory, shown as function of the dimensionless sphere velocity. (d) process schematic and the qualitative dimensionless penetration $\tilde{\Delta}$ time-history. Results are shown for $\tilde{\gamma} = 0.00016$, $E_\infty/E_0 = 10$.

Firstly, we focus on the effect of the imposed indenter dimensionless speed $\tilde{V}$ in approach–retraction (A-R) cycles with vanishing dwell time $\tilde{t}_d = t_d/\tau \to 0$, as reported in Fig. 4.3. Calculations are initialized assuming that the unloaded half-space instantaneously jumps into contact at $\tilde{\Delta} = 0$. Since this represent an instantaneous loading condition, regardless of $\tilde{V}$, at the very initial stage of the loading history the system's response is purely elastic and therefore follows the adhesive JKR solution with the elastic modulus given by E_∞. At very low A-R speed (see results for $\tilde{V} = 2 \times 10^{-5}$), the loading process is sufficiently slow to allow for full relaxation of the viscoelastic material, and hence the soft elastic JKR response with low frequency modulus E_0 is recovered during both approach and retraction. Therefore, in this case, the only source of hysteresis is the fact that the *jump into contact* solution differs from the pull-off one. Similarly, at very high speed (i.e., $\tilde{V} \gg 1$), the material behaves as a stiff elastic body and the glassy elastic JKR response occurs, again with vanishing hysteresis during the loading-unloading cycles. As expected, in both cases the maximum tensile load (i.e. the pull-off force) takes the same value, independently of the effective elastic modulus, in agreement with the JKR theory (see Chapter 1). Nonetheless, results in Fig. 4.3 clearly show that viscoelastic dissipation induces large adhesive hysteresis in A-R cycles over a large range of intermediate values of $\tilde{V}$. Qualitatively similar experimental results have been obtained [33, 34, 36, 139]. Importantly, during retraction, the system is able to withstand significantly larger tensile loads compared to the elastic case, as also clearly experimentally observed in [34, 67, 136, 139, 148]. A closer look at Fig. 4.3(a) reveals that the maximum tensile force can either occur at larger retraction distances compared to the elastic JKR and, for relatively large A-R speeds, even at positive penetration $\Delta > 0$, in agreement with experimental results shown in [33,35]. In the latter case, at the end of the approach stage, the material has not reached the viscoelastic glassy response yet. However, when the indenter motion is reversed (i.e., the speed jumps from $\dot{\Delta} = V$ to $\dot{\Delta} = -V$), the glassy behavior is triggered (with elastic modulus E_∞) and, since retraction occurs sufficiently fast, viscoelastic dissipation prevents the material from relaxing and detachment occurs at positive values of penetration Δ, with contact area and tensile load much larger than the elastic case.

Fig. 4.4 reports the surface displacement and the pressure distributions during an approach-retraction cycle at the given dimensionless speed $\tilde{V} = 0.002$. Focusing on the approach stage, beside the expected adhesion-induced square root singularity at the contact boundary, the interfacial pressure distribution also presents a positive annular peak close to the advancing circular perimeter of the contact area. A similar trend has been reported for viscoelastic adhesiveless approaching contacts in Ref. [128], at the leading edge of rolling (or frictionless sliding) viscoelastic contacts [30, 103, 107] (see also Chapters 3) and is predicted by the viscoelastic crack closing analysis (see Chapter 5). Moreover, during the early stages of the retraction process, the size of the contact area is almost unchanged, and it drops only once the maximum tensile load is reached. This prediction is supported by experimental observation [34, 36, 67, 148]. Notice that, during the retraction stage, the annular pressure peak disappears. Coherently, the pressure

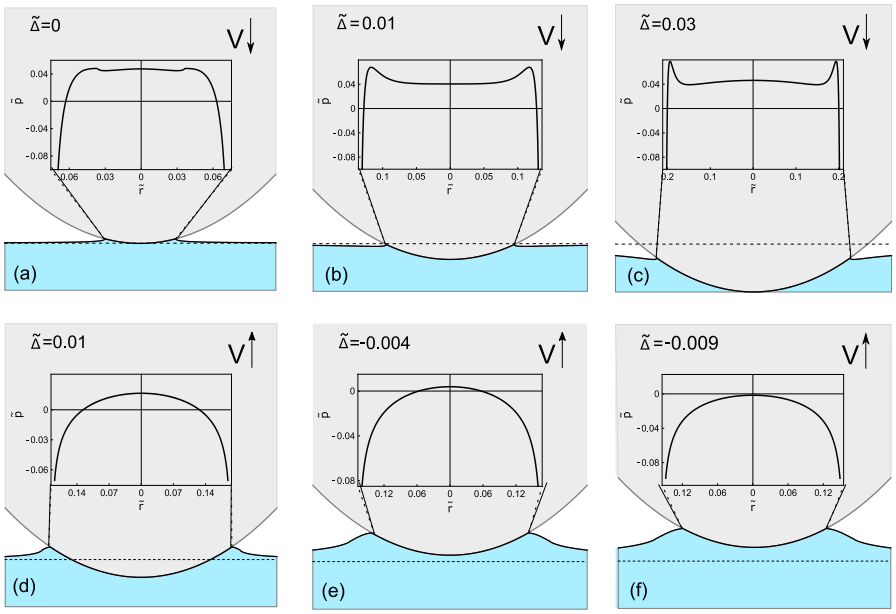

Figure 4.4: The deformed contact configuration during indentation (a-c) and retraction (d-f) at dimensionless sphere speed $\tilde{V} = 0.002$ (i.e, blue line in Fig.4.3) for different values of the dimensionless penetration $\tilde{\Delta}$. The inset shows the corresponding dimensionless contact pressure distribution $\tilde{p}$. Results are shown for $\tilde{\gamma} = 0.00016$, $E_\infty/E_0 = 10$.

peak is not predicted by the viscoelastic crack opening analysis (see Chapter 5). In this case instead, the adhesion-induced pressure singularity is associated with a trumpet-like opening crack shape, as predicted by De Gennes [129], as also observed in steady state sliding contacts (Chapters 3) and in agreement with Chapter 5.

4.5 Retraction from fully relaxed state

Results in Fig. 4.3 have shown that a viscoelastic-induced enhancement of the pull-off force can be observed at intermediate approach-retraction speeds, i.e. when the material has not yet fully entered the glassy state during the approach stage. Hence, one may guess that the enhancement of pull-off force or, equivalently, of the adhesion strength should be even more amplified if the retraction stage is allowed to begin, at finite speed, immediately after an extremely slow approach stage. This correspond to retraction from fully relaxed conditions at fixed positive penetration $\Delta > 0$ (dwell time $t_\mathrm{d} \to +\infty$), which is what we report in Fig. 4.5 for different dimensionless retraction speeds $\tilde{V}$. Specifically, retraction starts from point B at given dimensionless penetration $\tilde{\Delta}_\mathrm{B} = 0.032$ which coincides with the elastic JKR solution (i.e., with elastic modulus E_0) with dimensionless contact radius $\tilde{a}_\mathrm{B} = 0.245$ and dimensionless normal load $\tilde{F}_\mathrm{B} = 1.87 \times 10^{-3}$. During retraction, given a finite speed V, the contact penetration can be expressed as $\Delta = \Delta_B - H(t)\,Vt$, where $H(t)$ is the unit step function, and the retraction speed

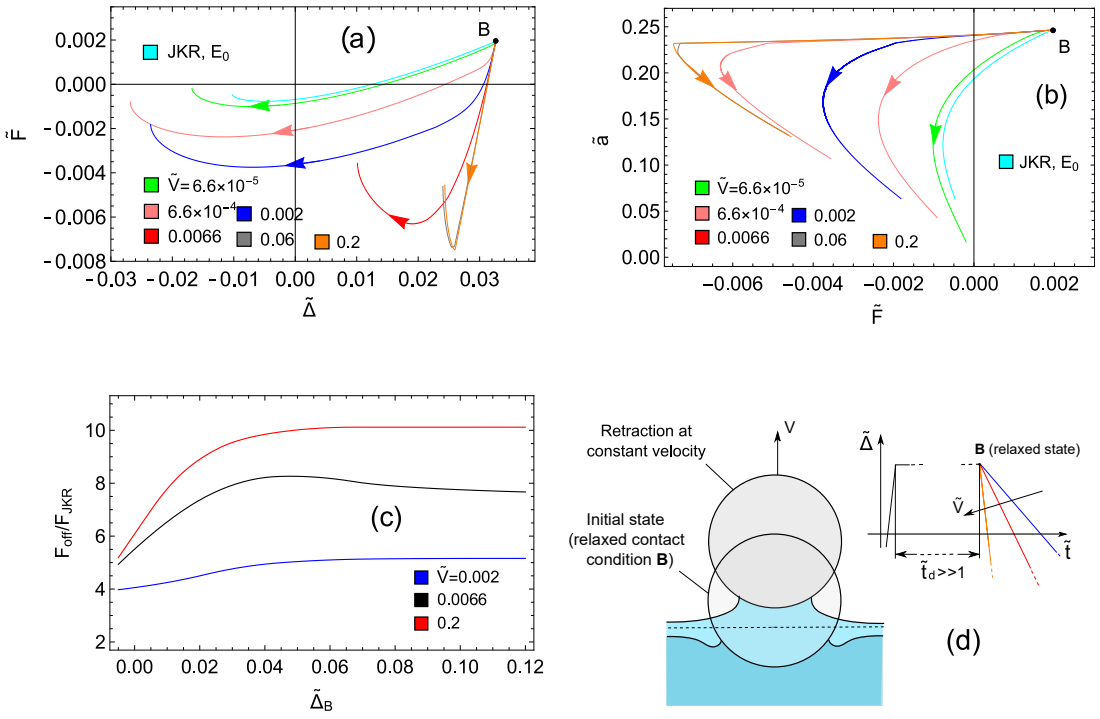

Figure 4.5: Sphere retraction at different dimensionless speed $\tilde{V}$ from fully relaxed conditions (point B, with $\tilde{\Delta}_B = 0.032$). (a) The dimensionless applied load $\tilde{F}$ vs. the dimensionless indentation depth $\tilde{\Delta}$. (b) The dimensionless contact radius $\tilde{a}$ vs. the dimensionless applied load $\tilde{F}$. (c) The pull-off force amplification ratio $F_{\text{off}}/F_{\text{JKR}}$ vs. the initial dimensionless penetration $\tilde{\Delta}_B$ for different values of dimensionless retraction speed. (d) The process qualitative time-history. Results are shown for $\tilde{\gamma} = 0.00016$, $E_\infty/E_0 = 10$.

instantaneously jumps from 0 to $-V$ at $t = 0$ (notice, $\dot{\Delta} = -H(t)V$). Therefore, at the early stages of the retraction process (i.e., for $t \ll \tau$), the material response is elastic, with modulus E_∞. Importantly, Fig. 4.5 shows that in this case the asymptotic response at very high velocity of retraction is no-longer described by the JKR curve, as instead observed in Fig. 4.3 . Now, some considerations can be made to explain the reported results: (i) a decrease of the contact area can only occur if the condition $g(r,t) \geq 0$ is fulfilled, (ii) a certain time or, equivalently, a certain retraction distance is required before enough elastic energy is stored into the system, (iii) a reduction of the contact area can only take place if the release of mechanical plus elastic energy is enough to compensate the change of adhesion energy. One concludes that during the initial stages of the retraction process the contact area will remain almost constant in a, say, 'frozen' state. When this happens the relation between the applied load F and the penetration Δ must obey the flat-punch linear relation [53, 149]

$$F = F_B - 2a_B \frac{E_\infty}{1-\nu^2}(\Delta_B - \Delta) = F_B - 2a_B \frac{E_\infty}{1-\nu^2} Vt \tag{4.21}$$

Interestingly, a similar behavior is also observed in temperature controlled systems [150], when the deformed material is cooled below the glass transition temperature T_g resulting in an almost 'frozen' contact shape. Provided that the material relaxation process has not yet started at detachment (i.e., the retraction velocity is sufficiently high), the pull-off force F_{off} is much larger that the JKR prediction F_{JKR}, i.e. $F_{off} > F_{JKR} = 3\Delta\gamma\pi R/2$. As a consequence, we conclude that during fast retraction: (i) the material is in the glassy state hence, att pull-off the energy release rate $G = K_I^2/(2E_\infty^*)$ with $E_\infty^* = E_\infty(1-\nu^2)$ must be necessarily equal to the adhesion energy per unit area, i.e. $G = \Delta\gamma$ (i.e., no enhancement of the effective energy of adhesion occurs- see also Secs. 4.9 and 4.10), (ii) the force - penetration and the force - area curves are significantly different from JKR predictions (see Chapter 1), (iii) the pull-off force cannot be predicted by JKR theory. Therefore, any experimental/numerical estimation of the effective adhesion energy at high speed pull-off through JKR is inappropriate [33, 63–67]. Conversely, during slow retraction the material has enough time to partially relax. As a consequence, the maximum tensile force decreases compared to the value predicted by the aforementioned arguments and monotonically diminishes with decreasing V, eventually reaching the elastic JKR value for extremely slow retraction speed. Contact stickiness and toughness are related to the minimum (negative) value of Δ before pull-off, as described in [45, 48]. In this regard, we note that for very small values of V the soft elastic JKR limit is recovered, but, at intermediate values of V (see curves for $\tilde{V} = 6.6 * 10^{-4}$) , a significantly larger elongations before pull-off is observed, compared to the elastic case. This happens when hysteretic viscoelastic losses occur only close to the circular boundary of the contact (small-scale viscoelasticity), where the material is excited on a time scale of order $\rho/|\dot{a}| \approx \rho/V \approx \tau$, where $\rho \ll R$ is the radius of curvature of the contact adhesive neck. In such conditions, the bulk of the material is instead excited on time scales of order $R/V > \tau$, thus behaving as a soft elastic material with modulus E_0. In

such small-scale viscoelasticity regime the energy release rate increases with the retraction speed (as better reported in Sec. 4.9), and the load-penetration and load-area curves are well approximated by the JKR predictions, provided that the adhesion energy $\Delta\gamma$ is replaced by an effective value $\Delta\gamma_{\text{eff}} = G$ (where G is the energy release rate). Note that only in this case the pull-off force can be correctly estimated by using the adapted JKR theory, i.e. $F_{\text{off}} = (F_{\text{JKR}})_{\text{eff}} = 3\pi\Delta\gamma_{\text{eff}}R/2$. Fig. 4.5 also reports the effect of the initial contact penetration $\tilde{\Delta}_{\text{B}}$ on the normalized pull-off force $F_{\text{off}}/F_{\text{JKR}}$ and shows that the maximum pull-off enhancement reaches a plateau at high penetration (i.e., high preload), with $F_{\text{off}}/F_{\text{JKR}} \approx E_\infty/E_0$ at very high retraction speed. Interestingly, at smaller speeds the ratio $F_{\text{off}}/F_{\text{JKR}}$ is less dependent on the initial condition, in agreement with numerical results shown in [66]. In Fig. 4.6 we report the surface displacement and the pressure distributions during the fast retraction from the relaxed state B at dimensionless speed value $\tilde{V} = 0.2$. The contact area is almost unchanged from the initial value in (a) and (b) and rapidly drops (c) close to the pull-off condition. Interestingly, Fig. 4.6 (c) shows that the fast detaching mechanism results into a deformed surface shape that perfectly preserves the memory of the initial deformation, and only an "elastic component" of the displacement is instantaneusly recovered for $a < |\mathbf{x}| < a_B$ as the contact boundary's radius recedes from a_B to a. Indeed, for $a < |\mathbf{x}| < a_{\text{B}}$ the displacement gap present the standard shape associated with the high frequency modulus

$$\Delta u(|\mathbf{x}|) = K_I/E^*_\infty\sqrt{8/\pi(|\mathbf{x}| - a)} \tag{4.22}$$

whereas for for $|\mathbf{x}| > a_{\text{B}}$ the shape function discontinuously switches to

$$\Delta u(|\mathbf{x}|) \simeq \Delta u(a_{\text{B}}) + K_I/E^*_0\sqrt{8/\pi(|\mathbf{x}| - a_{\text{B}})}. \tag{4.23}$$

in agreement with the discussion presented in Sec. 4.10.

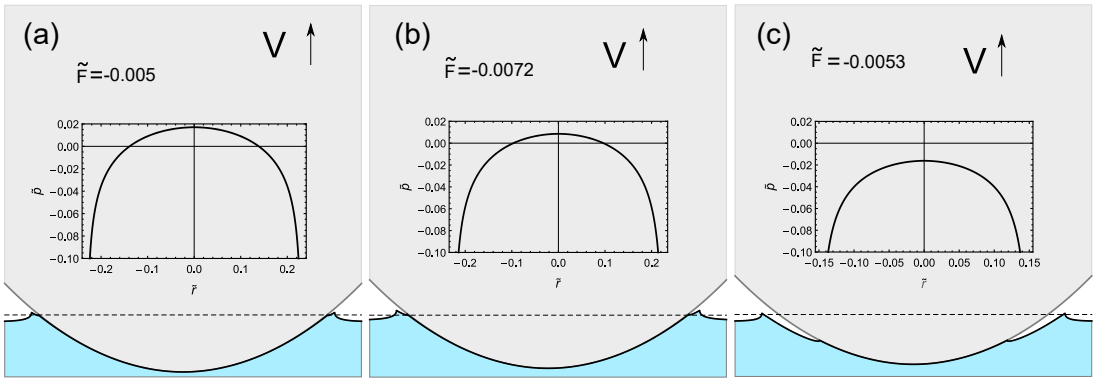

Figure 4.6: The progressive evolution [from (a) to (c)] of the pressure and displacement fields during the fast retraction at constant velocity, starting from the fully relaxed state at point B. Reults are shown for $\tilde{V} = 0.2$, $\tilde{\gamma} = 0.00016$, $\beta = 10$ and refer to three different values of the applied force.

4.6 The effect of the dwell time

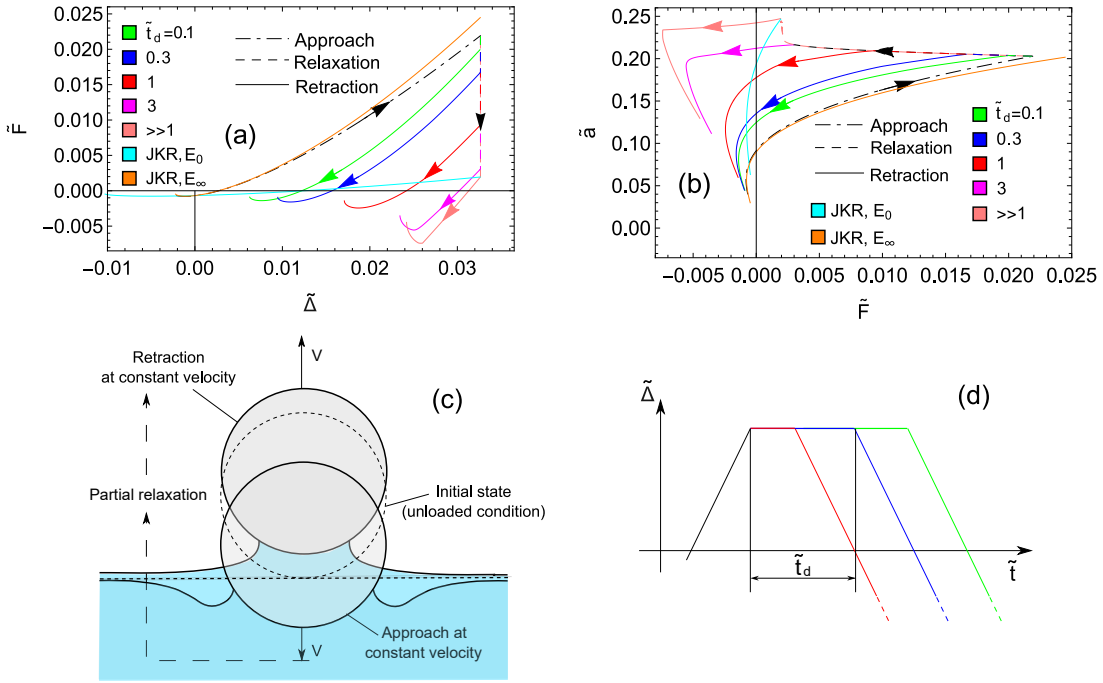

Figure 4.7: Approach-retraction cycles with non-vanishing dimensionless dwell time $\tilde{t}_d$, allowing for partial material relaxation. The dimensionless sphere speeed is $\tilde{V} = 0.1$. (a) The $\tilde{F}$ vs. $\tilde{\Delta}$ and (b) the $\tilde{a}$ vs. $\tilde{F}$ equilibrium diagrams for different values of $\tilde{t}_d$. (c) and (d) are the process schematic and the qualitative dimensionless penetration $\tilde{\Delta}$ time-history, respectively. Results are shown for $\tilde{\gamma} = 0.00016$, $E_\infty/E_0 = 10$.

In Fig.4.7 we report the effect on the adhesive contact behavior of the dimensionless dwell time $\tilde{t}_\mathrm{d}$, i.e. the time delay between the end of the approaching stage and the initiation of the retraction process. Since the value $\tilde{t}_\mathrm{d}$ physically alters the stress-strain history, it necessarily affects the system response during retraction, while the approach stage is unaffected. We present results for dimensionless speed $\tilde{V} = 0.1$, and show that increasing $\tilde{t}_\mathrm{d}$ above 1 yields larger pull-off forces. To understand this peculiar behavior, we observe that the material relaxation increases with $\tilde{t}_\mathrm{d}$ and, for $\tilde{t}_\mathrm{d} \gg 1$, the retraction behavior approaches the flat punch with very large pull off forces, as discussed above. Moreover, the A-R speed $\tilde{V}$ plays a central role, as increasing $\tilde{V}$ require larger $\tilde{t}_\mathrm{d}$ values to achieve relaxation and, in turn, enter the flat-punch regime. For $\tilde{V} = 0.1$ the sphere's velocity is quite high, hence the material's response during the approach stage is almost elastic and follows the (glassy) elastic JKR curve. Hence, according to results shown in Sec. 4.4, the pull-off force value tends to the JKR one for $\tilde{t}_\mathrm{d} \ll 1$. Under these conditions, the adhesive behavior is therefore highly affected by the presence of a finite dwell time.

4.7 The contact behavior under constant force

Figs. 4.8 reports the retraction behavior under load-controlled conditions assuming the same fully relaxed initial conditions (point B in the figure) as in Figs. 4.5. This time the tensile force is instantaneously applied following a step change to the negative value $F_0 < -F_{\mathrm{JKR}}$, i.e. $F(t) = F_{\mathrm{B}} + (F_0 - F_{\mathrm{B}})\, H(t)$. The application of this step change in the applied load leads to an initial high frequency glassy response of the system with modulus E_∞ so that the linear flat punch behavior is again recovered at the initial stages of the load controlled retraction. Then, the penetration also jumps to Δ_0 following the relation $F_0 = F_{\mathrm{B}} - 2a_{\mathrm{B}}E^*_\infty(\Delta_{\mathrm{B}} - \Delta_0)$, where $E^*_\infty = E_\infty/(1-\nu^2)$. After this step change, the contact area and the penetration Δ monotonically decrease with time, as well as the retraction speed, and eventually becomes unstable and detach [see Fig. 4.8(b)]. This happens at significantly larger elongations (i.e., larger contact toughness) compared to V-controlled (dashed) curves associated with the same pull-off forces F_0.

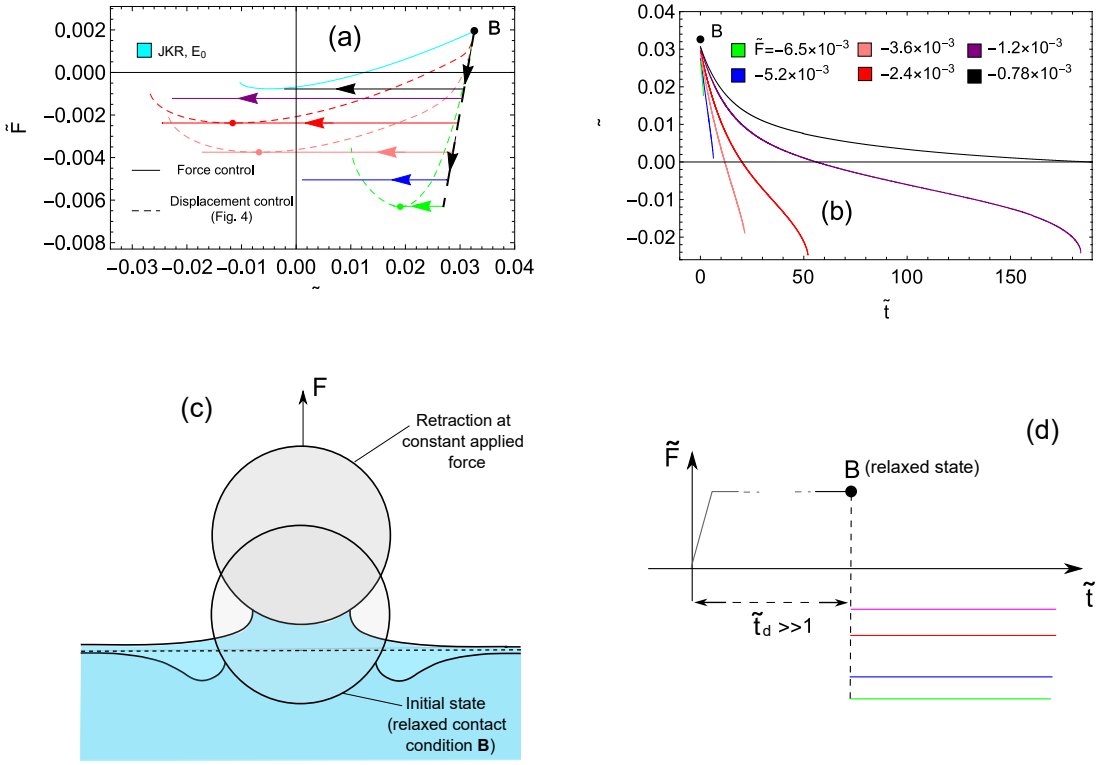

Figure 4.8: The contact behavior under constant tensile force $\tilde{F}$ instantaneously applied once the fully relaxed elastic condition is recovered (point B, with $\tilde{\Delta}_{\mathrm{B}} = 0.032$). (a) The $\tilde{F}$ vs. $\tilde{\Delta}$ equilibrium diagram for different values of the applied tensile force $\tilde{F}$ (solid lines); in the same figure, the dashed line is the behavior at constant retraction velocity corresponding the same pull-off force. (b) The dimensionless indentation depth $\tilde{\Delta}$ shown as function of the dimensionless time $\tilde{t}$ for different values of the applied tensile force $\tilde{F}$. (c) and (d) are the process schematic and the qualitative dimensionless penetration $\tilde{\Delta}$ time-history, respectively. Results are shown for $\tilde{\gamma} = 0.00016$, $E_\infty/E_0 = 10$.

4.8 Oscillations

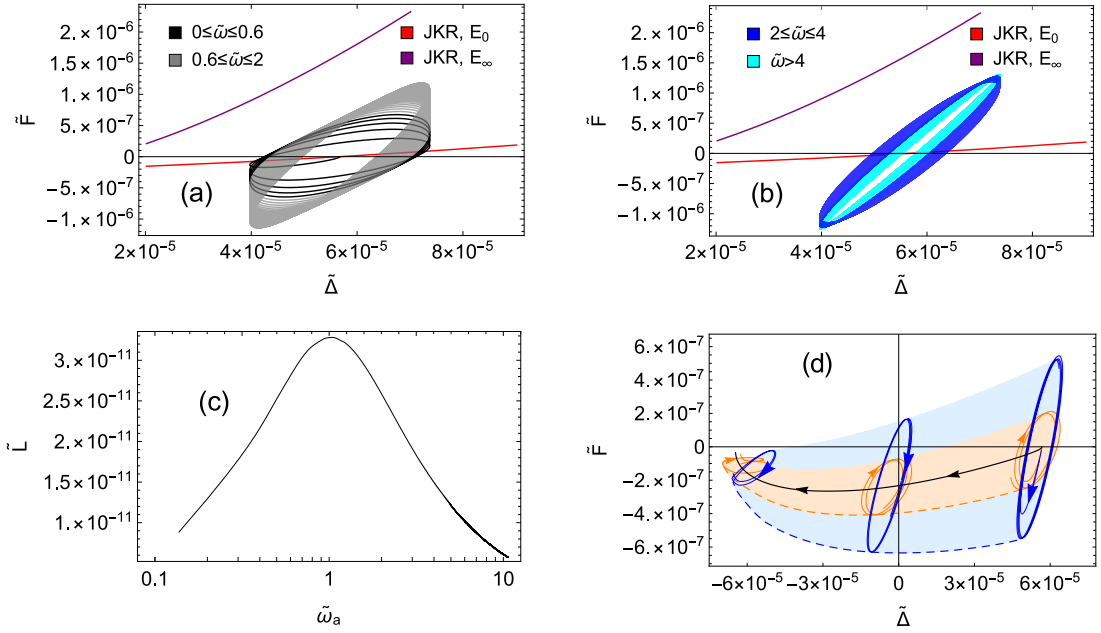

Figure 4.9: Results for normal oscillations: (a,b,c) frequency (up-)sweep around a given dimensionless penetration $\tilde{\Delta}_0$ with $\tilde{\Delta}\left(\tilde{t}\right) = \tilde{\Delta}_0 + \tilde{\Delta}_1 \sin\left[\tilde{\omega}\left(\tilde{t}\right)\tilde{t}/2\right]$ and $\tilde{\omega}(\tilde{t}) = \alpha\tilde{t}$; (d) constant frequency oscillation superimposed to steady retraction at $\tilde{V} = 10^{-7}$ from $\tilde{\Delta}_0$ with $\tilde{\Delta}\left(\tilde{t}\right) = \tilde{\Delta}_0 - \tilde{V}\tilde{t} + \tilde{\Delta}_2 \sin\left[\tilde{\omega}\tilde{t}\right]$. Specifically, (a,b) are the equilibrium diagram for $\tilde{F}$ vs. $\tilde{\Delta}(t)$, (c) is the dimensionless energy $\tilde{L} = (1-\nu^2)L/(\pi E_0 R^3)$ dissipated per cycle vs. the dimensionless frequency $\tilde{\omega}_a$ averaged per cycle, and (d) are the equilibrium diagrams $\tilde{F}$ vs. $\tilde{\Delta}(t)$ for $\tilde{\omega} = 0.35$ (orange line) and $\tilde{\omega} = 1.4$ (blue line). Results refer to $\tilde{\gamma} = 5 \times 10^{-8}$, $E_\infty/E_0 = 10$, $\tilde{\Delta}_0 = 5.7 \times 10^{-5}$, $\tilde{\Delta}_1 = -1.7 \times 10^{-5}$, $\tilde{\Delta}_2 = -8.5 \times 10^{-6}$, and $\alpha = 0.006$.

Fig. 4.9 reports the contact behavior of the contact when the penetration oscillates and refers to $\tilde{\gamma} = 5 \times 10^{-8}$ and $\delta\tilde{a} = 8.5 \times 10^{-4}$. Specifically, Fig. 4.9(a,b,c) presents results for a linear frequency sweep, i.e. $\tilde{\Delta}\left(\tilde{t}\right) = \tilde{\Delta}_0 + \tilde{\Delta}_1 \sin\left[\tilde{\omega}\left(\tilde{t}\right)\tilde{t}/2\right]$, with $\tilde{\omega} = \tau\left(d\theta/dt\right) = \alpha\tilde{t}$, $\alpha = 0.006$, $\tilde{\Delta}_1 = -1.7 \times 10^{-5}$. The the initial penetration $\tilde{\Delta}_0 = 5.7 \times 10^{-5}$ corresponds to the fully-relaxed (modulus E_0) JKR solution for $\tilde{F} = 0$. As the frequency is increased [see Fig.4.9(a,b)] the slope of the F vs. Δ curve increases because of the material stiffening, see also [65, 103, 140, 141]. The amount of energy dissipated per cycle $\tilde{L} = (1-\nu^2)L/(\pi E_0 R^3)$ roughly equates the area of the cycle in the $\tilde{\Delta}$ vs. $\tilde{F}$ diagram and is reported in Fig. 4.9(c) as a function of the external excitation frequency $\tilde{\omega}$. The observed bell-shaped behavior is expected, as at very low and very high excitation frequencies the material behaves elastically, with vanishing hysteresis. At intermediate frequency (i.e., $\tilde{\omega} \approx 1$) the material response is in the transition region of the viscoelastic spectrum, and the viscoelastic energy dissipation takes its maximum value. More interestingly, Fig. 4.9(d) refers to the case of constant frequency oscillations (at different frequencies) superimposed to steady retraction at speed $\tilde{V} = 10^{-7}$, so

that $\tilde{\Delta}\left(\tilde{t}\right) = \tilde{\Delta}_0 - \tilde{V}\tilde{t} + \tilde{\Delta}_2 \sin\left(\tilde{\omega}\tilde{t}\right)$ with $\tilde{\Delta}_2 = -8.5 \times 10^{-6}$, $\tilde{\omega} = 0.35$ (orange line) and $\tilde{\omega} = 1.4$ (blue line). Noteworthy, the envelopes of the maximum tensile loads (dashed lines) reached during the oscillating retraction stage significantly increase compared to the case of steady retraction (black curve, with no oscillations), thus paving the way to possible vibration based techniques to control interfacial adhesive strength, as experimentally observed by Shui *et al.* [119].

4.9 The energy release rate, the elastic energy, and viscoelastic energy dissipation

In viscoelastic materials undergoing deformations, the work of internal stresses is partially stored as elastic potential energy and partially dissipated, leading to viscoelastic hysteresis. Neglecting kinetic energy or inertia forces, energy balance requires the work per unit time of external and internal forces to be equal, i.e.

$$F\ \dot{\Delta} + \Delta\gamma\dot{A} = \dot{U} + P_{\mathrm{d}} \tag{4.24}$$

where $\dot{U}$ and P_{d} are the time-derivative of the stored elastic energy and the hysteretic energy losses per unit time, respectively. Most importantly, the energy release rate G can be defined also for non conservative materials (see also Chapter 3), as the change in the total mechanical energy per unit change in the contact area. Therefore, from Eq. (4.24), we have

$$G = \frac{\dot{U}}{\dot{A}} - F\frac{\dot{\Delta}}{\dot{A}} = \frac{dU}{dA} - F\frac{d\Delta}{dA}, \tag{4.25}$$

and

$$G = \Delta\gamma - P_{\mathrm{d}}/\dot{A} \tag{4.26}$$

which shows that G is a key quantity in adhesive contact mechanics, sometimes referred to as the effective energy of adhesion or, in other words, the generalized driving force inducing the contact area change. Consequently, calculating G is a crucial (and usually tough) task, which requires to determine either $\dot{U}$ or P_{d} as functions of the interfacial stress distribution $\sigma(\mathbf{x}, t)$. Aiming at accomplishing this task, we calculate the work per unit time P done by the internal stresses which, at equilibrium is only related to the stress and displacement distributions on the half-space surface. In the most general case (i.e., neglecting axial symmetry), we have

$$\begin{aligned} P\left(t\right) &= \int d^2x \sigma\left(\mathbf{x}, t\right) \dot{u}\left(\mathbf{x}, t\right) \\ &= \int d^2x d^2x_1 \mathcal{G}\left(\mathbf{x} - \mathbf{x}_1\right) \sigma\left(\mathbf{x}, t\right) \dot{\varepsilon}\left(\mathbf{x}_1, t\right) \end{aligned} \tag{4.27}$$

where

$$\varepsilon(\mathbf{x}, t) = \int_{-\infty}^{t} dt_1 J(t - t_1)\dot{\sigma}(\mathbf{x}, t_1) = \varepsilon_0(\mathbf{x}, t) + \sum_{k=1}^{n} \varepsilon_k(\mathbf{x}, t) \tag{4.28}$$

is an apparent local surface strain, $J(t) = E_\infty^{-1} + \sum_{k=1}^{n} E_k^{-1} \left[1 - \exp\left(-t/\tau_k\right)\right]$ is the creep function for a generic linear viscoelastic material with an arbitrary number n of relaxation times τ_k, and

$$\begin{aligned} \varepsilon_0(\mathbf{x}, t) &= \frac{\sigma(\mathbf{x}, t)}{E_\infty} \\ \varepsilon_k(\mathbf{x}, t) &= \int_{-\infty}^{t} dt_1 \frac{1}{E_k} \left[1 - \exp\left(-\frac{t - t_1}{\tau_k}\right)\right] \dot{\sigma}(\mathbf{x}, t_1) \end{aligned} \tag{4.29}$$

are, respectively, the elastic contribution to ε associated with the high-frequency modulus E_∞, and the viscoelastic contributions associated with each single k-th Voigt element. We then have

$$\sigma\left(\mathbf{x}, t\right) = E_\infty \varepsilon_0\left(\mathbf{x}, t\right) = E_k \varepsilon_k\left(\mathbf{x}, t\right) + \tau_k E_k \dot{\varepsilon}_k\left(\mathbf{x}, t\right), \qquad k = 1, ..., n \tag{4.30}$$

where $E_k \varepsilon_k(\mathbf{x}, t)$ and $\tau_k E_k \dot{\varepsilon}_k(\mathbf{x}, t)$ represent, respectively, the elastic and viscous stress components associated with the k-th Voigt element. Combining Eqs. (4.27, 4.28, 4.29,4.30) gives the expression of the elastic $\dot{U}$ and dissipative P_d contributions to P (i.e., $P = \dot{U} + P_\mathrm{d}$). In particular,

$$\dot{U}(t) = \int dx^2 dx_1^2 \mathcal{G}\left(\mathbf{x} - \mathbf{x}_1\right) \left[E_\infty \varepsilon_0\left(\mathbf{x}, t\right) \dot{\varepsilon}_0\left(\mathbf{x}_1, t\right) + \sum_{k=1}^{n} E_k \varepsilon_k\left(\mathbf{x}, t\right) \dot{\varepsilon}_k\left(\mathbf{x}_1, t\right)\right] \tag{4.31}$$

and

$$P_\mathrm{d}(t) = \sum_{k=1}^{n} \int dx^2 dx_1^2 \mathcal{G}(\mathbf{x} - \mathbf{x}_1) \tau_k E_k \varepsilon_k\left(\mathbf{x}, t\right) \dot{\varepsilon}_k\left(\mathbf{x}_1, t\right) \tag{4.32}$$

Note that in Eq. (4.31) the quantity $\mathcal{G}\left(\mathbf{x}\right)$ is a symmetric function so that it is possible to find the expression of the elastic energy as

$$U\left(t\right) = \frac{1}{2} \int dx^2 dx_1^2 \mathcal{G}\left(\mathbf{x} - \mathbf{x}_1\right) \left[E_\infty \varepsilon_0\left(\mathbf{x}, t\right) \varepsilon_0\left(\mathbf{x}_1, t\right) + \sum_{k=1}^{n} E_k \varepsilon_k\left(\mathbf{x}, t\right) \varepsilon_k\left(\mathbf{x}_1, t\right)\right] \tag{4.33}$$

The energy release rate G can be calculated using Eqs. (4.25, 4.31) at any given time t once solved the viscoelastic problem, i.e. for known values of $\sigma\left(\mathbf{x}, t\right)$, $u\left(\mathbf{x}, t\right)$, and the contact domain $\Omega\left(t\right)$.

Recalling that $G = \Delta\gamma - P_\mathrm{d}/\dot{A}$ and considering that $P_\mathrm{d} > 0$, we find that during the approach stage (i.e., $\dot{A} > 0$) the energy release rate $G < \Delta\gamma$ and can be even negative, whereas during retraction (i.e., $\dot{A} < 0$) the energy release rate $G > \Delta\gamma$. Figure 4.10 reports the trends of the normalized energy release rate $G/\Delta\gamma$ vs. speed, during (a) retraction and (b) approach stages. More specifically, $P_\mathrm{d}/\dot{A}$ vanishes at very-low and very-large A-R speeds, so that in these two limiting cases $G(t) \to \Delta\gamma$. At intermediate speed it increases up to a maximum value, with the resulting bell-shaped behavior being related to the presence of a reference length scale, i.e., finite contact size (see [85, 130] and Chapter 3). For comparison, we recall that the propagation of a opening semi-infinite crack

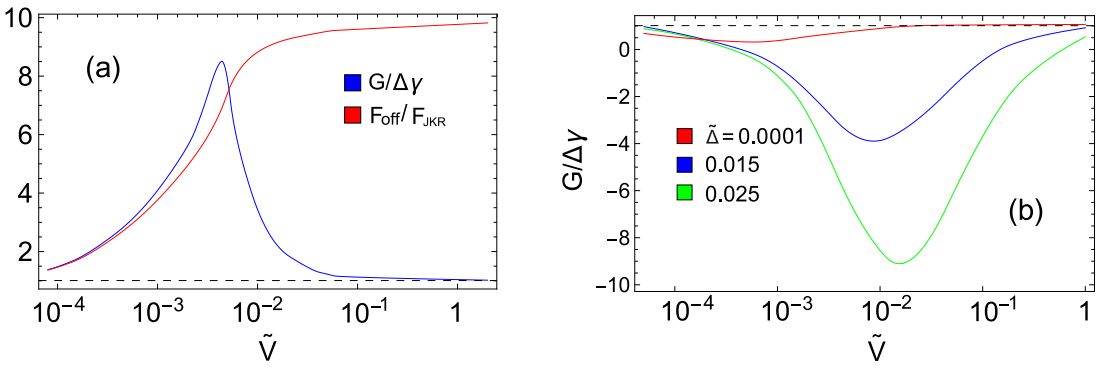

Figure 4.10: The normalized energy release rate $G/\Delta\gamma$ (a) at pull-off (blue line) and (b) during indentation (for different dimensionless penetrations $\tilde{\Delta}$) as functions of the dimensionless retraction velocity (blue line). The viscoelastic-elastic pull-off force ratio $F_{\text{off}}/F_{\text{JKR}}$ is also shown in (a) as red line. Initial condition for calculation is fully relaxed state. Results are shown for $\tilde{\gamma} = 0.00016$, $E_\infty/E_0 = 10$.

in an infinite systems represents a very different scenario, as in this case $P_{\text{d}}/\dot{A}$ must monotonically increase with crack speed and eventually reach a plateau (for isothermal conditions), as shown in [68–72] and in Chapter 5. Noteworthy, since P_{d} accounts for the energy dissipation in the whole viscoelastic material, it can also take values such that $P_{\text{d}}/\dot{A} > \Delta\gamma$, thus entailing $G(t) < 0$ when the sphere is pressed against the viscoelastic half-space [see Fig. 4.10(b)]. Fig. 4.10(a) also reports the normalized maximum tensile load (i.e. the pull-off force) as a function of the retraction speed. It is very important to notice that, despite the bell-shaped rate $G(t)$ vs. $\tilde{V}$ trend, the ratio $F_{\text{off}}/F_{\text{JKR}}$ continuously increases until a limiting value is reached ($F_{\text{off}}/F_{\text{JKR}} \approx E_\infty/E_0$). A deeper look at the retraction behavior [Fig. 4.10(a)] also shows that $G/\Delta\gamma \approx F_{\text{off}}/F_{\text{JKR}}$ only at relatively low retraction speeds, i.e. for $\tilde{V} \lesssim 5 \times 10^{-4}$. This is the limit where small-scale viscoelasticity (i.e., localized non-conservative phenomena close to the edge of the contact) govern the adhesion enhancement (see [37] and Chapter 3), and JKR pull-off approximation $F_{\text{off}} = (F_{\text{JKR}})_{\text{eff}} = 3\pi\Delta\gamma_{\text{eff}}R/2$ holds true (allowing for a rough estimation of $G = \Delta\gamma_{\text{eff}}$). Differently, at large retraction speeds, both the small- and large-scale viscoelasticity vanish (e.g., $G \to \Delta\gamma$), and the pull-off is governed by the glassy flat punch behavior, as discussed in Sec. 4.5. To the best of authors knowledge, this is a novel finding, as previous numerical studies on viscoelastic adhesive contacts (with gap-dependent adhesion) [65, 66, 78, 142] relied on JKR pull-off equation to estimate the energy release rate G even at high retraction speed.

4.10 A closer look into fast retraction

In this section we investigate in deeper detail the contact behavior during a very fast retraction starting from a general fully relaxed state B. Specifically, we present an analytic model that describes the entire equilibrium curves in the high velocity

limit (see Fig.4.5 for $\tilde{V} > 0.2$). Observe that, in agreement with the surface deformation shown in Fig. 4.6 (c), the crack opening gap close to the perimeter of contact is

$$\Delta u(\mathbf{x}) = K_I/E^*_\infty \sqrt{8/\pi(|\mathbf{x}| - a)} \tag{4.34}$$

Therefore, since the asymptotic stress field has the standard square-root form, one might expect the closure equation Eq. 4.9 to read as

$$\frac{K_I^2}{2E^*_\infty} = \Delta\gamma \tag{4.35}$$

However, the crack displacement gap for $a < |\mathbf{x}| < a + \delta a$ is correctly described by Eq. (4.35) only if the contact radius has decreased of a certain amount, at least larger than the quantity δa appearing in Eq. (4.9) which estimates the process zone's length. Therefore, only in this case Eq. (4.34) holds. Indeed, note that the stress intensity factor in the initial state B is

$$K_{I,\mathrm{B}} = (2\Delta\gamma E^*_0)^{1/2} \ll (2\Delta\gamma E^*_\infty)^{1/2} \tag{4.36}$$

Therefore, since during the whole retraction $K_I(\Delta(t))$ must be a continuous function, we conclude that the flat punch-like response reflects the fact that a certain time (or analogously a certain distance) is needed for the stress intensity factor to (linearly) increase to the value provided by Eq. (4.35). This occurs when the contact penetration Δ has decreased to a certain value Δ_C. Then, for $\Delta < \Delta_\mathrm{C}$, the fast decrease of contact radius occurs (see Fig.4.5 for $\tilde{V} > 0.2$), and the contact behavior is determined by Eq. (4.35).
Aiming at deriving the general relation between the stress intensity factor, the contact penetration, and the contact radius during the fast retraction, we define the following quantities:

$$\begin{aligned} \sigma_1(\mathbf{x}, t) &= \sigma(\mathbf{x}, t) - \sigma_{0,\mathrm{B}}(\mathbf{x}) \\ u_1(\mathbf{x}, t) &= u(\mathbf{x}, t) - u_{0,\mathrm{B}}(\mathbf{x}) \end{aligned} \tag{4.37}$$

where $\sigma(\mathbf{x}, t)$ and $u(\mathbf{x}, t)$ are the actual stress and displacement fields at time t, related each other through Eq. (4.1), whilst $\sigma_{0,\mathrm{B}}(\mathbf{x})$ and $u_{0,\mathrm{B}}(\mathbf{x})$ are the stress and displacement fields recovered in the fully relaxed configuration B. Therefore, they are related each other as

$$u_{0,\mathrm{B}}(\mathbf{x}) = \frac{1}{E_0} \int dx_1^2 \mathcal{G}(\mathbf{x} - \mathbf{x}_1)\sigma_{0,\mathrm{B}}(\mathbf{x}_1) \tag{4.38}$$

(note that $u_1(\mathbf{x}, t < 0) = 0$ and $\sigma_1(\mathbf{x}, t < 0) = 0$). Than, the superposition of effects implies that

$$u_1(\mathbf{x}, t) = \int_{-\infty}^{t} dt_1 J(t - t_1) \int dx_1^2 \mathcal{G}(\mathbf{x} - \mathbf{x}_1)\dot{\sigma}_1(\mathbf{x}_1, t_1) \tag{4.39}$$

$$= \frac{1}{E_\infty} \int dx_1^2 \mathcal{G}(\mathbf{x} - \mathbf{x}_1)\sigma_1(\mathbf{x}_1, t) \tag{4.40}$$

where we assumed that, since we focus on the extremely fast retraction, the time scale of the process is $\ll \tau$. We conclude that under these conditions the viscoelastic problem corresponds to the superposition between two elastic problems with different moduli. Moreover, since the contact area during retraction only decreases, Eq. (4.37) shows that $\sigma_1(r,t)$ and $u_1(r,t)$ must satisfy the following boundary conditions

$$\begin{aligned} u_1(\mathbf{x},t) &= \Delta_{\mathrm{B}} - \Delta(t), & |\mathbf{x}| < a < a_{\mathrm{B}} \\ \sigma_1(\mathbf{x},t) &= -\sigma_{0,\mathrm{B}}(\mathbf{x}), & a < |\mathbf{x}| < a_{\mathrm{B}} \\ \sigma_1(\mathbf{x},t) &= 0, & |\mathbf{x}| > a_{\mathrm{B}} \end{aligned} \tag{4.41}$$

Then, as long as $\Delta(t) > \Delta_{\mathrm{C}}$, solving the mixed boundary value problem expressed by Eqs. (4.37, 4.38 , 4.40, 4.41) is quite trivial. In this case, neglecting the small variations of contact radius observed in Fig. 4.5 (b) we can use $a = a_{\mathrm{B}}$ and therefore Eqs. (4.40, 4.41) describe a flat-punch problem [149] that depends on the elastic modulus E_∞. Hence, the stress intensity factor and the force linearly depend on Δ as:

$$K_I(\Delta(t),\Delta_{\mathrm{B}}) = K_{I,\mathrm{JKR}}(\Delta_{\mathrm{B}},a_{\mathrm{B}}) + (\Delta_{\mathrm{B}} - \Delta(t))\,\frac{E^*_\infty}{\sqrt{\pi a_{\mathrm{B}}}}, \qquad \Delta(t) > \Delta_{\mathrm{C}} \tag{4.42}$$

$$F(\Delta(t),\Delta_{\mathrm{B}}) = F_{\mathrm{JKR}}(\Delta_{\mathrm{B}},a_{\mathrm{B}}) - 2a_{\mathrm{B}}E^*_\infty\,(\Delta_{\mathrm{B}} - \Delta(t))\,, \qquad \Delta(t) > \Delta_{\mathrm{C}} \tag{4.43}$$

where

$$K_{I,\mathrm{JKR}}(\Delta,a) = \frac{E^*_0}{\sqrt{\pi a}}(\frac{a^2}{R} - \Delta)$$

$$F_{\mathrm{JKR}}(\Delta,a) = E^*_0 R^{1/2}\Delta^{3/2}\left(\frac{a}{(R\Delta)^{1/2}} - \frac{2}{3}\frac{a^3}{(R\Delta)^{3/2}}\right)$$

are relations provided by [38, 145] for the sphere contact case, and provide the initial values (i.e., at point B) of the stress intensity factor and of the applied force as function of the initial contact penetration and contact radius (i.e., the solution of the elastic problem '0' with modulus E_0). The other terms appearing in Eqs. 4.43 that depend on E_∞ are instead solutions of the flat-punch problem (i.e., problem '1'). Then, Δ_{C} is obtained by solving

$$K_I(\Delta_{\mathrm{C}},\Delta_{\mathrm{B}}) = \sqrt{2E^*_\infty\Delta\gamma} \tag{4.44}$$

However, once that $\Delta(t) < \Delta_{\mathrm{C}}$ the same mixed boundary value problem is less trivial and must be solved considering that the contact area changes and is unknown. However, an additional equation is now available, i.e., the energy closure equation expressed as in Eq. (4.35). In this case, using that $a < a_{\mathrm{B}}$, one can demonstrate that Eqs. (4.37 , 4.38, 4.40, 4.41) imply that the stress intensity factor and the applied force depend on the (yet unknown) contact radius and on the contact penetration as

$$K_I(a,\Delta(t),\Delta_{\rm B}) = K_{I,{\rm JKR}}(\Delta_{\rm B},a) + (\Delta_{\rm B}-\Delta(t))\,\frac{E^*_\infty}{\sqrt{\pi a}}, \qquad \Delta(t)<\Delta_{\rm C} \quad (4.45)$$

$$F(a,\Delta(t),\Delta_{\rm B}) = F_{\rm JKR}(\Delta_{\rm B},a) - 2aE^*_\infty\ (\Delta_{\rm B}-\Delta(t))\,, \qquad \Delta(t)<\Delta_{\rm C} \quad (4.46)$$

Eq. 4.46 follows from the fact that, since the problem expressed by Eqs. (4.40, 4.41) is an elastic problem (i.e., path-independent) the actual stress and displacement fields $\sigma(\mathbf{x},t)$ and $u(\mathbf{x},t)$ in the contact condition $\Delta(t)$ with contact radius a are the same that would be obtained by considering a first decrease of contact radius from $a_{\rm B}$ to a at constant penetration $\Delta_{\rm B}$, followed by a retraction from $\Delta_{\rm B}$ to $\Delta(t)$ at constant contact radius a (this path of course differs from the real one). Moreover, it can be demonstrated that in the first stage of this process, i.e., when $\Delta{=}\Delta_{\rm B}$ and the contact radius is a, the (actual) viscoelastic pressure distribution is exactly the same recovered in the elastic (JKR) case with modulus E_0 assuming penetration $\Delta_{\mathbf{B}}$ and contact radius a. In turn, the latter result is analogue to that presented in chapter 5 for steady-state crack opening in viscoelastic solids and follows form similar arguments. The equilibrium curves $K_I(\Delta(t))$ and $F(\Delta(t))$ are then derived by solving

$$K_I(a,\Delta(t),\Delta_{\rm B}) = \sqrt{2E^*_\infty\Delta\gamma} \quad (4.47)$$

for a at every instant. Fig. 4.11 (a),(b) shows equilibrium diagrams of $\tilde{F}$ vs. $\tilde{\Delta}$ and $\tilde{a}$ vs $\tilde{F}$ for different initial points B. Notably, numerical results (dashed lines, corresponding to dimensionless retraction speed $\tilde{V}=0.2$, see Fig. 4.5) perfectly overlap with the analytical model (solid line) proposed in this section, with small differences ascribable to neglected variations of contact area during the 'flat-punch' stage. Notably, Fig. 4.11 (c) shows that the pull-off force estimation based on the purely elastic flat punch model equation with the high frequency modulus, i.e. (see [149]):

$$F_{\rm off,FP} = \sqrt{8\pi E^*_\infty\Delta\gamma a_{\rm B}^3} \quad (4.48)$$

leads to large overestimation, especially for large values of $\Delta_{\rm B}$.

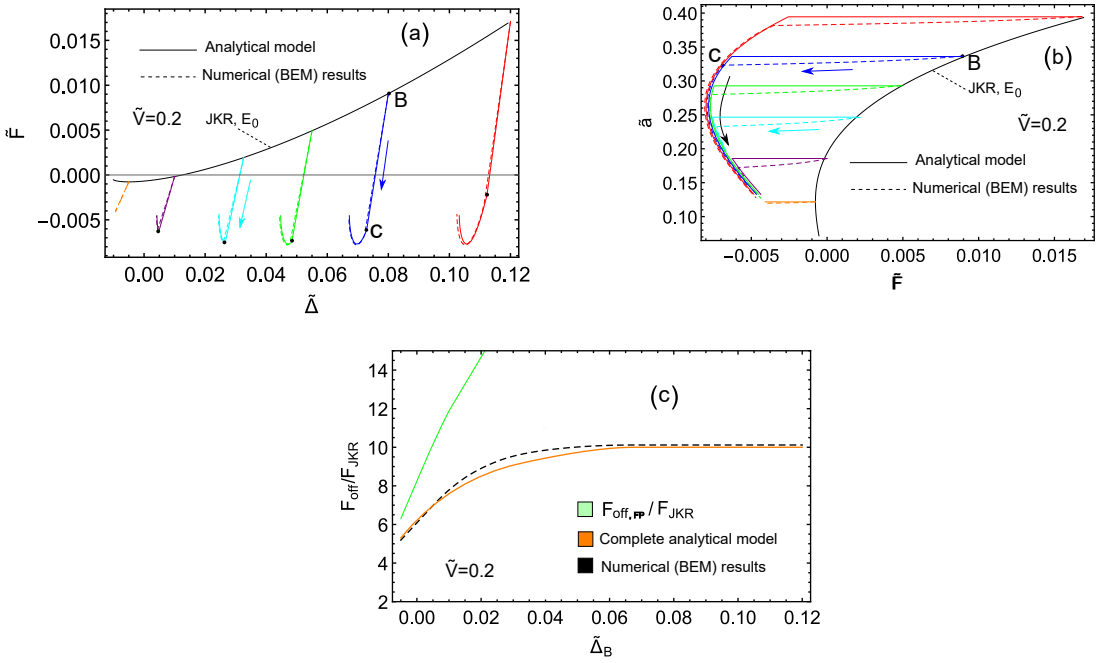

Figure 4.11: The contact behavior under fast retraction from fully relaxed state: comparison between numerical results (dashed line) and results predicted by the analytical proposed in Sec. 4.10 (solid line) for different initial conditions. (a) The dimensionless applied force $\tilde{F}$ vs. the dimensionless penetration $\tilde{\Delta}$ (b) the dimensionless contact radius $\tilde{a}$ vs. the dimensionless applied force $\tilde{F}$. (c) The viscoelastic-elastic pull-off force ratio $F_{\text{off}}/F_{\text{JKR}}$ as function of the initial penetration $\tilde{\Delta}_B$. The green line is the pull-off force in the purely elastic flat punch model assuming a Young modulus equal to E_∞ (see Eq.4.48). Results refer to $\tilde{\gamma} = 0.00016$, $E_\infty/E_0 = 10$.

4.11 Conclusion

In this chapter, the energy approach presented in Chapter 3 has been extended to general unsteady conditions. The problem of the unsteady normal indentation of a rigid sphere into a viscoelastic half-space, in the presence of interfacial adhesion, has been addressed. Additionally, a rigorous procedure to accurately calculate the time evolution of the elastic energy, the viscoelastic energy dissipation, and energy release rate G by relying only on the interfacial stress and displacement distributions has been presented. We found that, depending on the specific time-history of the contact process, the effective adhesion may be significantly enhanced by viscoelasticity. At intermediate approach-retraction speeds, strong adhesive hysteresis is observed because of small-scale viscoelastic dissipation localized close to the perimeter of the contact area, which also entails the ability of the system to withstand very high tensile loads. Hysteresis vanishes at very high and very low approach-retraction speed as the material response falls, respectively, in the high frequency (stiff) or low frequency (soft) elastic regimes. More importantly, our theory predicts the extremely large pull-off forces observed experimentally when retraction starts from a completely relaxed loaded state, with sufficiently high retraction speed. In this case, the material has no time to relax and exhibits a 'frozen' glassy elastic state, thus resembling the behavior of a flat-punch with a linear force-penetration relation. Moreover, we found that at sufficiently large retraction speed V, the energy release rate reduces with the increasing V down to the thermodynamic surface energy value $\Delta\gamma$. However, in such conditions the contact behavior significantly deviates from JKR theory as small-scale viscoelasticity cannot be invoked in this case. This implies that the JKR model cannot be employed to estimate the energy release from pull-off force at high retraction speeds, as this procedure significantly overestimates G.

Chapter 5

Steady and unsteady crack propagation in viscoelastic solids

In Chapter 1 we clarified that crack equilibrium and propagation in elastic materials are governed by the balance between the surface energy per unit area $\Delta\gamma$ and the energy release rate G. Since in linear elasticity G depends on the externally applied loading condition only through the stress intensity factor K_I and the material's elastic constants, the critical condition for fracture $G > \Delta\gamma$ is easily solved as long as the dipendence of K_I from the applied load or displacement is determined for the specific problem's geometry. However, the intrinsic viscoelastic response of rubbery-like materials might result into much more complex phenomena, as shown in Chapters (3, 4). Indeed, in the presence of non-conservative behaviors the Griffth energy balance has to be properly modified. Overall, viscoelastic fracture mechanics is a topic of large interest. Several theoretical models of viscoelastic crack propagation have been proposed over the last decades, and we refer the reader to [154, 164] for a detailed review of the topic. Many of the existing studies are based on cohesive zone models [68, 70, 84, 153]. In this class of approaches, the stress singularity at the crack tip is removed by exploiting a stress-gap adhesive law within the failure zone. Other studies are based energetic arguments, firstly introduced qualitatively by De Gennes [156] and subsequently formalized by Persson [69]. Although steady-state propagation has been widely investigated, very less has been done for unsteady fracture. Additionally, also the experimental literature is far more limited. This discrepancy can be (at least partially) explained observing that when a crack propagates in steady-state regime within a widely extended medium theoretical formulations are significantly semplified. Indeed, as the material is fully relaxed in the majority of its volume, elastic models can be exploited to derive the dependence of G from the applied load or displacement, as shown in [89, 158] for different geometries. Hence, G can be experimentally measured and compared with theoretical predictions. In this case, the steady crack opening speed resulting from a certain applied load is the one ensuring that the energy equilibrium $G = \Delta\gamma + E_d$ is satisfied, where E_d is the internally dissipated energy for each unit advance of the crack's tip position, and only depends on the crack velocity [157]. As result, G is velocity dependent and for

an opening crack the energy balance implies $G > \Delta\gamma$ [157], whereas for a closing crack one obtains $G < \Delta\gamma$ [155] (note that for a closing crack $G = \Delta\gamma - E_d$). Anyway, if the aforementioned assumptions are relaxed, the calculation of G and E_d in unsteady conditions is much more complex, as they depend on the entire time-history of the internal strain and stress fields, as shown in Chapter 4. These arguments have fundamental implications when a viscoelastic sheet containing a pre-existing crack initially unloaded is subjected to a step-function force. In this case, the instantaneous initial response of the viscoelastic material is purely elastic everywhere within the solid with the high frequency modulus E_∞. Thus, the crack equilibrium in the earliest stage of the loading history is described by the Griffith fracture criterion, hence if the applied load is such that $\Delta\gamma > G = K_I^2/(2E_\infty)$ crack cannot propagate. However, in this case, after showing an instantaneous glassy response the material undergoes viscoelastic creep within its whole volume and the magnitude of the strain field monotonically increases over time and, in turn, also the elastic energy stored in the polymeric chains. This suggests that fracture might occur after a certain time, once a certain threshold of elastic energy needed for propagating the crack is stored. This phenomenon, usually referred to as delayed fracture, has been experimentally observed in lab tests carried on polymeric [159,160] and colloidal [162,163] gels and Homalite polymers [161] exhibiting viscoelastic relological behavior.
In this chapter the energy approach object of this dissertation is applied to study the steady and unsteady crack propagation in viscoelastic media. In the first three sections, we study the crack propagation and healing in infinitely extended systems. In this case, the crack behavior resembles the local response at the contact edges in steady-state sliding contacts in the small-scale viscoelastic regime (Chapter 3). In this chapter, the features of displacement and stress fields and the overall effect of the process zone's length are deeply investigated. Results are also compared in detail with previous studies. In the fourth section, the energy closure equation derived in unsteady contacts in Chapter 4 is applied to the unsteady crack propagation problem, with particular focus on the delayed fracture.

5.1 Steady crack opening and closing behavior

Let us consider a single crack opening or closing at constant velocity v in an infinite viscoelastic media. This guarantees that infinitely far from the crack tip the material is fully relaxed so that it behaves as an elastic material with low frequency Young's modulus E_0. We also assume that the velocity is sufficiently high or the process zone sufficiently small to assume that the entire viscoelastic energy dissipation occurs far from the crack tip. This means that at the crack tip the material is the glassy state and its response is governed by the high frequency Young's modulus E_∞. Of course this hypothesis is questionable in ligth of the findings by Creton et al [133]. We assume steady state conditions and we assume a reference frame co-moving with the crack tip (see Fig. 5.1). Therefore, the explicit time-dependence of the moving displacement and stress field is masked

and we can write: $u(x,t) = u(x-vt) = u(x)$ and $\sigma(x,t) = \sigma(x-vt) = \sigma(x)$ where we used the substitution $x \to x+vt$. Then, the elastic-viscoelastic correspondence principle (see Chapter 2) implies that:

$$u\left(x\right) = J\left(0\right)\int dx'\mathcal{G}\left(x-x'\right)\sigma\left(x'\right) + \int_{0^+}^{+\infty} dt\dot{J}\left(t\right)\int dx'\mathcal{G}\left(x+vt-x'\right)\sigma\left(x'\right) \tag{5.1}$$

where $J\left(t\right)$ is the creep function and $\mathcal{G}(x)$ is the elastic Green's function for a material of unit modulus for the plain strain or plane stress problem. Now let us call the reference displacement $u_1\left(x,t\right)$ the quantity

$$u_1\left(x\right) = \int dx'\mathcal{G}\left(x-x'\right)\sigma\left(x'\right) \tag{5.2}$$

Notably, it represents the elastic displacement that would be obtained because of the real stress distribution $\sigma\left(x\right)$ assuming a unitary Young modulus. Therefore we also note that

$$u_1\left(x+vt\right) = \int dx'\mathcal{G}\left(x+vt-x'\right)\sigma\left(x'\right)$$

so that we can write

$$u\left(x\right) = J\left(0\right)u_1\left(x\right) + \int_{0^+}^{+\infty} dt\dot{J}\left(t\right)u_1\left(x+vt\right) \tag{5.3}$$

In very similar way it is easy to show that by defining the reference stress distribution $\sigma_1\left(x\right)$ such that

$$u\left(x\right) = \int dx'\mathcal{G}\left(x-x'\right)\sigma_1\left(x'\right) \tag{5.4}$$

$\sigma_1\left(x\right)$ represent the elastic stress that would be obtained in corrispondence of the real displacement distribution $u\left(x\right)$ assuming a unitary Young modulus. In such a case one can also write the dual formulation of Eq. (5.3) that is:

$$\sigma\left(x\right) = R\left(0\right)\sigma_1\left(x\right) + \int_{0^+}^{+\infty} dt\dot{R}\left(t\right)\sigma_1\left(x+vt\right) \tag{5.5}$$

where $R\left(t\right)$ is the relaxation function.

Notably, these expressions apply for the asymptotic stress and displacement fields at the contact edges in the small-scale viscoelastic regime of sliding contacts (Chapter 3). In what follows, the displacement and stress fields in the visocoelastic crack opening and closing problems are calculated as function of the applied stress intensity factor and of the crack's velocity. The problem is than closed by enforcing the energy equilibrium, allowing to derive the energy release rate vs. crack's speed curve.

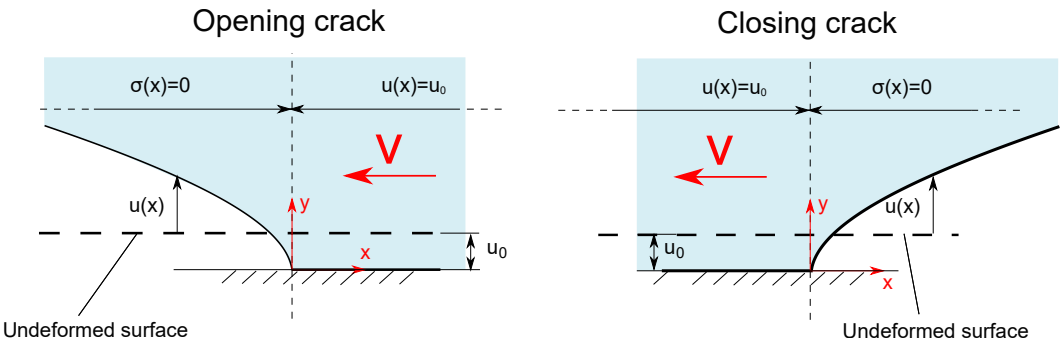

Figure 5.1: The schematic of the steady-state crack propagation problem in a reference frame co-moving with the crack tip for (left) opening crack and (right) closing crack.

5.2 Crack opening in steady-state conditions

We assume that the crack is opening with the crack tip advancing at constant velocity $v > 0$ in an infinitely extended medium under steady state conditions. As shown in Fig. 5.1, using a reference frame co-moving with the crack tip the boundary conditions of the mixed boundary value problem are

$$\begin{aligned} u(x) &= u_0; \qquad x \geq 0 \\ \sigma(x) &= 0; \qquad x < 0 \end{aligned} \tag{5.6}$$

Where u_0 is a remotely enforced displacement. To solve the problem of the opening viscoelastic crack let first us assume that

$$u_1(x) = \kappa u_0; \qquad x \geq 0$$

and let us calculate the quantity κ such the real (for the viscoelastic material) boundary conditions Eq. (5.6) are satisfied. For $x \geq 0$, using Eq. (5.3) and recalling that $u(x \geq 0) = u_0$ and that the time integration is made for $t > 0$ so that $u(x + vt) = u_0$ we get

$$\kappa = 1/J(\infty) = E_0 \tag{5.7}$$

where E_0 is the low frequency modulus of the viscoelastic material. Now in order to calculate the stress distribution for $x > 0$ let us use Eq. (5.2) by enforcing the condition that $\sigma(x < 0) = 0$, so we obtain

$$u_1(x > 0) = E_0 u_0 = \int dx' \mathcal{G}(x - x') \sigma(x') = \int_{0^+}^{+\infty} dx' \mathcal{G}(x - x') \sigma(x') \tag{5.8}$$

that can be rephrased as

$$u_0 = J(\infty) \int_{0^+}^{+\infty} dx' \mathcal{G}(x - x') \sigma(x') \tag{5.9}$$

which allow to calculate the stress distribution for $x > 0$. We can then calculate

$$u_1(x < 0) = \int_{0^+}^{+\infty} dx' \mathcal{G}(x - x') \sigma(x') \tag{5.10}$$

and

$$u\left(x<0\right)=J\left(0\right)u_{1}\left(x\right)+\int_{0^{+}}^{+\infty}dt\dot{J}\left(t\right)u_{1}\left(x+vt\right) \tag{5.11}$$

Note that the calculated displacement field $u\left(x\right)$ and $\sigma\left(x\right)$ satisfy Eq. (5.1) and the boundary conditions Eq. (5.6) and therefore represent the unique solution of the viscoelastic state. From this treatment we immediately conclude that for the opening crack the viscoelastic stress distribution $\sigma\left(x\right)$ coincides with the stress distribution that would be obtained for the perfectly elastic case with elastic modulus E_0 as follows from Eq. (5.9). The displacement, instead, for $x<0$ will differ from that of the perfectly elastic case as follows from Eq. (5.10). Note that, in this case, we cannot apply the inverse argument i.e. moving from the condition $\sigma\left(x<0\right)=0$ and using Eq. (5.5), (as done in the next section for the closing crack) since we need to integrate for positive times and then the quantity $x+vt$ becomes positive for $t>-x/v$ thus preventing us from moving further. Now let us calculate the energy release rate. We move from the consideration that the singular behavior of the stresses close to the crack tip is given by

$$\sigma\left(x\right)=\frac{K_{I}}{\sqrt{2\pi x}} \tag{5.12}$$

where K_I is stress intensity factor of the corresponding elastic case and is equal to the stress intensity factor of the viscoelastic case i.e.

$$\left(K_{I}\right)_{1}=K_{I}$$

Since in the problem at hand the system is infinitely extended, i.e., the viscoelastic material is fully relaxed within the majority of its volume, the energy release rate has the same expression of the reference elastic problem:

$$G=\frac{K_{I}^{2}}{2E_{0}} \tag{5.13}$$

Now we note that from Eq. (5.10) it follows that:

$$u_{1}\left(x<0\right)\approx E_{0}u_{0}+K_{I}\sqrt{\frac{8\left|x\right|}{\pi}} \tag{5.14}$$

Notably, in Eq. (5.11), the corrective term is eventually responsible for the classical trumpet shape of the viscoelastic deformed profile shown in Fig. 5.2. Indeed, its contribution tends to vanish very close to the crack's tip, specifically for $|x|\ll v\tau$, where we obtain

$$u\left(x<0\right)\approx u_{0}+\frac{K_{I}}{E_{\infty}}\sqrt{\frac{8\left|x\right|}{\pi}},\qquad\left|x\right|\ll v\tau \tag{5.15}$$

Using this expression, the radius of curvature of the crack is:

$$\rho_{1}=\frac{4}{\pi}\left(\frac{K_{I}}{E_{\infty}}\right)^{2}=\frac{8}{\pi}\frac{E_{0}}{E_{\infty}^{2}}\frac{K_{I}^{2}}{2E_{0}}=\frac{8G}{\pi\beta E_{\infty}} \tag{5.16}$$

Instead, for $|x| \gg v\tau$ the material is fully relaxed, indeed Eq. (5.11) gives

$$u\left(x<0\right) \approx \frac{u_1\left(x<0\right)}{E_0} = u_0 + \frac{K_I}{E_0}\sqrt{\frac{8\left|x\right|}{\pi}}, \quad |x| \gg v\tau \tag{5.17}$$

which allows to identify a remote (much larger) crack tip radius (see Fig. 5.2), consistently with the overall trumpet shape:

$$\rho_2 = \frac{4}{\pi}\left(\frac{K_I}{E_0}\right)^2 = \frac{8G}{\pi E_0} \tag{5.18}$$

Notably, both radii are proportional to the energy release rate and the ratio $\rho_2/\rho_1 = \left(E_\infty/E_0\right)^2$ is extremely large if one considers that E_∞/E_0 might be larger than 10^3. However, for a given value of the stress intensity factor K_I (i.e., for a given value of the energy release rate) the steady crack velocity must be determined as part of the solution. At this aim, we enforce that at virtual variations of the crack's length the work of internal stresses must be balanced by the work of (external) adhesive forces. The mathematical and physical framework is exactly analogue to that presented for steady state sliding contacts (Chapter 3) and Eq. (3.4) also applies to the present opening crack problem. Therefore, the (virtual) work of internal stresses over a small virtual variation δa of the crack tip position is

$$\left(\delta L_I\right)_T = \frac{1}{2}\int_0^{\delta a} \sigma\left(x\right)\left[u\left(x-\delta a\right) - u_0\right] dx \tag{5.19}$$

and is exactly balanced by the (virtual) work of external adhesive forces

$$\left(\delta L_E\right)_T = \Delta\gamma\delta a \tag{5.20}$$

so that at equilibrium we can write

$$\left(\delta L_I\right)_T = \left(\delta L_E\right)_T \tag{5.21}$$

Now note that taking the limit $\delta a \to 0$ and substituting Eqs. (5.12, 5.15) into Eq. (5.19) leads to

$$\left(\delta L_I\right)_T = \frac{K_I^2}{2E_\infty}\delta a \tag{5.22}$$

Therefore, using Eqs. (5.21, 5.20, 5.13), we obtain

$$G = \frac{E_\infty}{E_0}\Delta\gamma \tag{5.23}$$

This velocity-independent expression would be in significant contrast with experimental evidences. This apparent contradiction follows from the fact that exploiting the energy balance in the limit $\delta a \to 0$ might be a not proper physical assumption. Indeed, in real fracture processes, the standard square root law expressed by Eq. (5.12) only applies up to some finite distance from the crack tip, below

which the local behavior is governed by complex phenomena not included in linear models, such as formation of cavities, plastic deformations and large deformations in non-linear regime [69, 132, 133]. The zone in which these phenomena come into play and Eq. (5.12) is no longer valid is usually referred to as process-zone. Eq. (5.23) suggests that not introducing this characteristic length in the model leads to unreasonable predictions. This is a well-known issue in viscoelastic fracture mechanics, as observed in [69, 164]. In our theory, δa should take the same order of magnitude as the characteristic length of the problem, i.e., the size of the process zone. Observe now that since Eq. (5.23) is recovered as long as the displacement gap has the square root expression given by Eq. (5.15), this result is obtained as long as $\delta a \ll \tau v$. One might expect that if the crack's velocity is extremely high the quantity τv is reasonably very much higher than the process zone length. Therefore, in the high velocity limit Eq. (5.23) is recovered. On the other hand, in the limit of infinitely slow crack growth, one might expect that the process zone length is $\delta a \gg \tau v$. Therefore, in this case, within the very major part of the integration domain in Eq. (5.19) the displacement field is now given by Eq. (5.17) (i.e., the material is fully relaxed). Hence, in this case we obtain

$$(\delta L_I)_T = \frac{K_I^2}{2E_0}\delta a \tag{5.24}$$

and, using again Eqs. (5.21, 5.13), we finally recover $G = \Delta\gamma$. This represents the correct limit result for low crack propagation speed. Hence, we conclude the overall G vs. v trend is correctly predicted when δa is set to small but finite values, whose order of magnitude is the same of the process zone's length. Similarly, in the energy approach proposed by Persson and Brener (PB) for viscoelastic crack opening [69], the viscoelastic dissipation within the bulk of the material can be correctly calculated only if a cut-off length is introduced in the model. The latter is estimated as the distance a^* from the crack tip at which the square root singularity of the stress distribution takes some critical value σ_c, i.e., $a^* = \left[K_I/(\sqrt{2\pi}\sigma_c)^2\right]$. Therefore, the quantity $a_0 = \left[2\Delta\gamma/(\sqrt{2\pi}\sigma_c)^2\right]$, i.e. the cut-off length in the limit of slowly moving crack, is an input parameter of the Persson-Brener theory. Note that, also in this case, we neglect the effect of local non-liner phenomena that would require to substitute $\Delta\gamma$ with an effective adhesion term, representing the energy release rate in the limit of slow moving crack. Notably, Eq. (5.13) shows that $a^*(v) = a_0 G(v)/\Delta\gamma$. In our discussion, we exploit the Persson-Brener estimation of the process zone's length and we assume that the velocity-dependent process-zone's length is

$$\delta a(v) = \alpha \left(\frac{K_I(v)}{\sqrt{2\pi}\sigma_c}\right)^2 \tag{5.25}$$

where α is an arbitrary real constant. Fig. 5.3. Shows the G vs. v trend obtained by enforcing the energy closure equation Eq. (5.21), in which the velocity-dependent displacement gap is calculated according to Eqs. (5.3, 5.14), the stress field $\sigma(x)$ is given by Eq. (5.12), the stress-intensity factor is related to G according to Eq. (5.13) and parameter δa is velocity-dependent and set as shown in Eq.

(5.25). In the figure, results of the Persson-Brener theory are also reported. The almost perfect overlap among the two theories is obtained when $\alpha \simeq 0.3$. Moreover, changing the parameter α only shifts the curve and does not affect its shape. Following other studies, as those of Schapery and Greenwood based on a cohesive zone model [40, 84], the characteristic length of the system, i.e., the unbonding zone's length in which the internal stress assumes a constant value σ_0, takes the value $\delta a = \pi K_I^2/(8\sigma_0^2)$. This is equivalent at setting $\alpha \simeq 2.5$ (see the red curve in figure) if we assume that in Eq. (5.25) the critical stress σ_c has the same meaning as the quantity σ_0 of the Greenwood's model. In a recent study [85], Persson observed that the best overlapp among the PB theory and the Greenwood's results is obtained by setting $\sigma_0 \simeq 3\sigma_c$. Interestingly, assuming that $\delta a = \pi K_I^2/(8\sigma_0^2)$ as in the Greenwood model and that $\sigma_0 \simeq 3\sigma_c$, is therefore equivalent at setting $\alpha \simeq 0.3$ in Eq. (5.25). The remarkable result is that the qualitative trend is in any case not affected by of the detailed description of debonding processes at the crack tip, and both the PB theory, the Greenwood-Schapery model and the theory object of this thesis provide consistent results by relying on significantly different approaches.

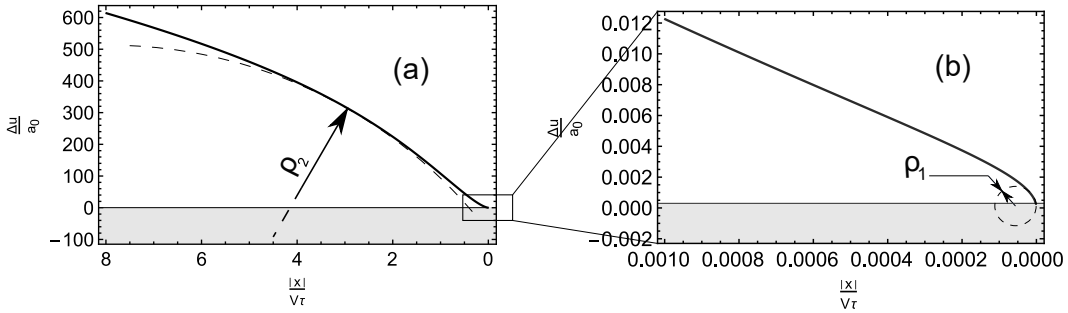

Figure 5.2: (a) The viscoelastic trumpet shape of the opening crack's deformed profile in terms of dimensionless displacement gap $\Delta u/a_0$, where $a_0 = 2\Delta\gamma/\left(\sqrt{2\pi}\sigma_c\right)^2$ represents the estimation of the process-zone's length in the limit of slowly moving crack. ρ_2, given by Eq. (5.18), is the curvature radius describing the fully relaxed region at distance from the crack tip $|x| \gg v\tau$. (b) shows the magnification at the crack tip ($|x| \ll v\tau$) where the shape of the profile reflects a glassy response described by a smaller radius of curvature ρ_1 given by Eq. (5.16). Results refer to $v/v_0 = 3 \times 10^3$ with $v_0 = a_0/\tau$ and $E_\infty/E_0 = 10^3$ and single relaxation time creep's function.

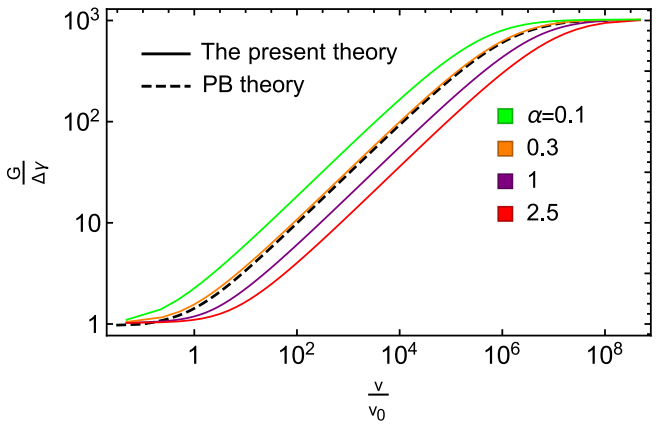

Figure 5.3: The normalized energy release rate $G/\Delta\gamma$ as function of the dimensionless opening crack's velocity v/v_0 in a log-log diagram, where $v_0 = a_0/\tau$, being τ the single relaxation time of the viscoelastic material and $a_0 = 2\Delta\gamma/\left(\sqrt{2\pi}\sigma_c\right)^2$ represents the estimation of the process-zone's length in the limit of slowly moving crack. The solid lines refer to the present theory's predictions, for different values of the real constant α in Eq. (5.25). The dashed line refers to the Persson-Brener theory's predictions [69]. Results are given for $E_\infty/E_0 = 10^3$ and single relaxation time creep's function

.

5.3 Crack closing in steady-state conditions

We assume that the crack is closing with the crack tip advancing at constant velocity $v > 0$. Assuming the reference frame co-moving with the crack's tip, as shown in Fig. 5.1, the boundary conditions are

$$\begin{aligned} \sigma(x) &= 0; \qquad x > 0 \\ u(x) &= u_0; \qquad x \leq 0 \end{aligned} \tag{5.26}$$

This time for $x > 0$ the stress $\sigma(x + vt) = 0$ and we can proceed all the other way around, so let us assume that $\sigma_1(x > 0) = 0$ and let us check that this condition leads to the right solution. Indeed, using Eq. (5.5)

$$\sigma(x) = R(0)\,\sigma_1(x) + \int_{0^+}^{+\infty} dt \dot{R}(t)\,\sigma_1(x + vt) = 0; \qquad x > 0 \tag{5.27}$$

Hence, the first of the two boundary conditions Eq. (5.26) is already satisfied. Now let us calculate the $\sigma_1(x < 0)$ by inverting Eq. (5.4) for $x < 0$, i.e. by solving the following equation

$$u(x < 0) = u_0 = \int_{-\infty}^{0^-} dx' \mathcal{G}(x - x')\,\sigma_1(x') \tag{5.28}$$

Then, we use Eq. (5.4) to calculate

$$u(x > 0) = \int_{-\infty}^{0^-} dx' \mathcal{G}(x - x')\,\sigma_1(x') \tag{5.29}$$

and Eq. (5.5) to calculate the stress for $x < 0$

$$\sigma(x) = R(0)\,\sigma_1(x) + \int_{0^+}^{|x|/v} dt\dot{R}(t)\,\sigma_1(x+vt) \tag{5.30}$$

The determined solution [$u(x)$ and $\sigma(x)$] satisfies Eq. (5.1) and the boundary conditions given in Eq. (5.26), and therefore represents the unique solution of the viscoelastic state. Now we define the reference elastic analogue stress field $\sigma_e(x)$

$$\sigma_e(x<0) = \frac{(K_I)_1}{\sqrt{2\pi x}}$$

that satisfies

$$u(x>0) = J(\infty)\int_{-\infty}^{0^-} dx'\mathcal{G}(x-x')\,\sigma_e(x') \tag{5.31}$$

where $u(x)$ is the displacement of the viscoelastic problem. Moreover, $\sigma_1(x)$ and $\sigma_e(x)$ are related each other as

$$\sigma_1(x) = J(\infty)\,\sigma_{el}(x) = \frac{1}{E_0}\sigma_e(x)$$

Then, following Eq. (5.29) the displacement field of the viscoelastic problem is:

$$u(x>0) = u_0 + \frac{(K_I)_1}{E_0}\sqrt{\frac{8x}{\pi}} \tag{5.32}$$

This discussion shows that the displacement-stress behavior of the viscoelastic closing crack is specular to that of the opening crack. Indeed, in this case the the viscoelastic displacement field $u(x)$ coincides with the one that would be obtained for the perfectly elastic case with elastic modulus E_0 as follows from Eqs. (5.28, 5.29, 5.31). The stress instead differs, as follows from Eq. (5.30). This is in agreement with Schapery's analysis [68, 84]. Notably, Eq. (5.30) shows that very close to the crack tip, for $|x| \ll v\tau$, we have

$$\sigma(x<0) \approx R\left(0^+\right)\sigma_1(x<0) \approx \frac{E_\infty}{E_0}\frac{(K_I)_1}{\sqrt{2\pi|x|}}, \quad |x| \ll v\tau \tag{5.33}$$

which means that the stress intensity factor K_I of the viscoelastic case is related to that of the elastic analogue $(K_I)_1$ as

$$K_I \approx \frac{E_\infty}{E_0}(K_I)_1 \tag{5.34}$$

Instead, as expected, sufficiently far from the crack tip, i.e., for $|x| \gg v\tau$, the stress viscoelastic distribution recovers the one of the elastic case since the material is fully relaxed:

$$\sigma(x<0) \approx \frac{(K_I)_1}{\sqrt{2\pi|x|}}, \quad |x| \gg v\tau \tag{5.35}$$

Hence the energy release rate of the viscoelastic problem is

$$G = \frac{(K_I)_1^2}{2E_0} \tag{5.36}$$

And, therefore, according to the crack shape provided by Eq. (5.32) the crack tip radius for a viscoelastic crack closing is again proportional to the energy release rate:

$$\rho_2 = \frac{4}{\pi}\left(\frac{(K_I)_1}{E_0}\right)^2 = \frac{8G}{\pi E_0}$$

Observe that the profile trumpet shape is not predicted for the closing crack and is specific of the opening case. In Fig. 5.4 we show the overall stress distribution for a closing crack. Notably, at distance of order τv from the crack's tip, the stress distribution presents a negative (i.e., compressive) peak. A similar result has been shown in Chapter 3 at the contact leading edge in sliding contacts, in Chapter 4 during normal indentation, and by Greenwood [70] using a cohesive-zone model for crack closing, and is not predicted for opening crack cases. Once the energy equilibrium is enforced, this behavior entails a completely different scenario from the opening crack case.
The energy balance at the crack tip reads as:

$$(\delta L_I)_T = \frac{1}{2}\int_0^{\delta a} \sigma\,(-x)\,[u\,(\delta a - x) - u_0]\,dx = (\delta L_E)_T = \Delta\gamma\delta a \tag{5.37}$$

Also in this case, taking the limit $\delta a \to 0$ and using Eqs. (5.32, 5.33) gives again

$$(\delta L_I)_T = \frac{K_I^2}{2E_\infty}\delta a \tag{5.38}$$

However, since now the energy release rate is related to the 'remote' stress intensity factor $(K_I)_1 \neq K_I$, using Eqs. (5.34, 5.36, 5.37, 5.38) this time yields:

$$G = \frac{E_0}{E_\infty}\Delta\gamma \tag{5.39}$$

i.e., the effective energy of adhesion would be velocity-independent and very much smaller than $\Delta\gamma$. However, also for the closing crack, the actual G vs. v curve can be predicted by assuming that δa is a small but finite quantity and, analogously to the opening crack case, Eq. (5.39) represents the result for extremely high crack speed, corresponding to $\delta a \ll v\tau$. On the other hand, at very low velocity, since $\delta a \gg v\tau$, in Eq. (5.37) the stress field is this time almost entirely represented by Eq. (5.35), therefore we obtain

$$(\delta L_I)_T = \frac{K_I^2}{2E_0}\delta a \tag{5.40}$$

and in turn, using Eqs. (5.36, 5.37), we get $G = \Delta\gamma$. In [151], Persson adapted the PB theory to the closing crack case [see Fig. 5.5(a)]. However, he observed

that assuming again that the cut-off length $a^* = \left[K_I/(\sqrt{2\pi}\sigma_c)\right]^2$ might lead to a physically unreasonable scenario. Indeed, in the limit of high velocity, the cut-off length would be $a^* = G(v \to \infty)/\Delta\gamma a_0 = E_0/E_\infty a_0$, i.e., well below atomic distances considered that typically a_0 is of order 1 nm and that $E_0/E_\infty \simeq 10^{-3}$. Therefore, he also presented a modified theory in which the cut-off length is assumed constant and equal to a_0 (see Fig. 5.5 (a)). In Fig. 5.5 (a) we report the G vs. v trend predicted by the present theory, adopting the two approaches proposed by Persson for the characteristic length estimation. First (solid pink lines), we exploit the same velocity dependent expression of the parameter δa, as already done for the opening crack:

$$\delta a(v) = \alpha \left(\frac{(K_I)_1(v)}{\sqrt{2\pi}\sigma_c} \right)^2 \tag{5.41}$$

where we remind that $(K_I)_1(v) = \sqrt{2E_0 G(v)}$ is the stress intensity factor recovered at distance $|x| \gg v\tau$. Then, we assume that δa is constant (solid blue line) and equal to

$$\delta a = \alpha a_0 = \alpha \left(\frac{2\Delta\gamma}{\sqrt{2\pi}\sigma_c} \right)^2 \tag{5.42}$$

Results indicate consistency between the proposed theory and the Persson's approach, as long as the assumptions made while estimating the characteristic cut off-length are the same. The almost perfect overlap is obtained when $\alpha \simeq 0.5$.
Data shown in Fig. 5.5 (b) instead are based on the Schapery's model of the cohesive zone for a viscoelastic closing crack. According to Schapery [68], the remote stress intensity factor $(K_I)_1$ and the characteristic cohesive zone's length δa for a crack closing in a viscoelastic media must satisfy the following equation:

$$(K_I)_1 = \alpha\sigma_0 E_0 \left(\frac{2}{\pi}\right)^{1/2} \int_0^{\delta a} J\left(\frac{\zeta - \delta a}{v}\right) \zeta^{-1/2} d\zeta \tag{5.43}$$

where α is an arbitrary dimensionless real constant that we set in our calculation. The resulting energy release rate vs. the crack velocity trend is reported in Fig. 5.5(b). The figure also reports the results obtained by Greenwood [70] based on the Schapery's model. The overlap among the two theories is obtained by setting $\alpha = 0.5$. We conclude that, despite the description of the process zone is still a partially unsolved problem, the theory object of this thesis provides consistent results with previous studies as long as the same assumptions are made while estimating the characteristic length scale associated with local non-linear phenomena at the crack tip.

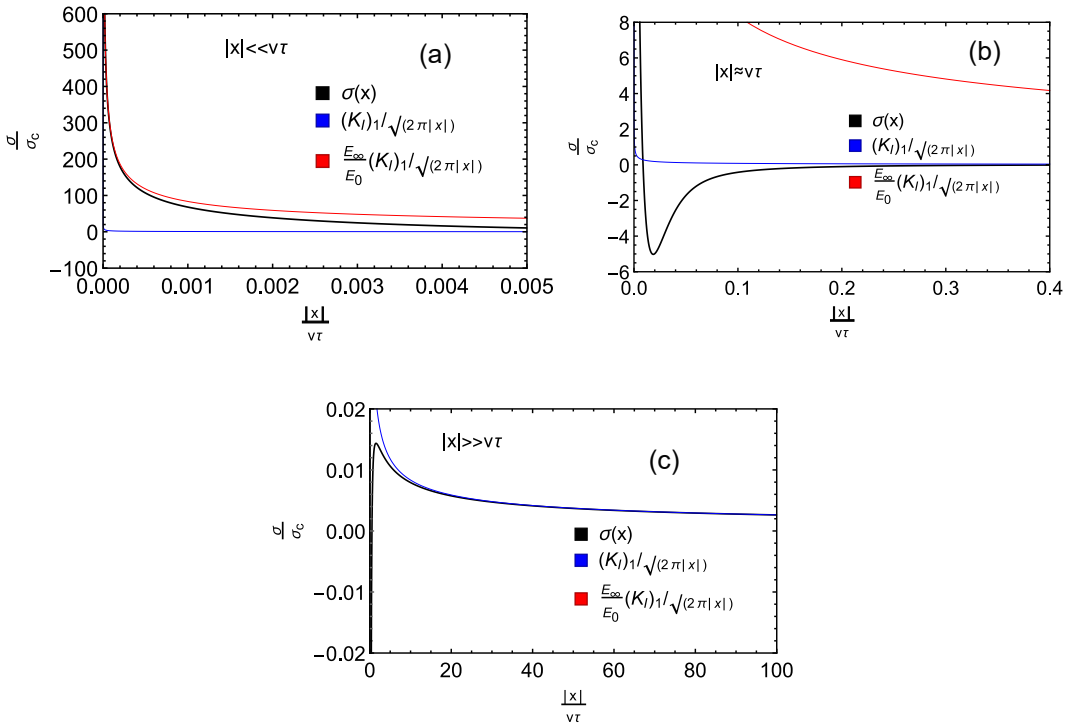

Figure 5.4: The dimensionless stress distribution for a steady closing crack at distance from the crack's tip $\ll v\tau$ (a), $\simeq v\tau$ (b) and $\gg v\tau$ (c). Note that σ_c is a critical value of the stress in the process-zone, whose order of magnitude is $\Delta\gamma/\epsilon$, being ϵ the range of adhesive interactions. The asymptotic limits recovered close to the crack tip (red line) and far from the crack tip (blue line) described by the standard square root expression are reported. Note that the stress-intensity factor close to the tip is E_∞/E_0 times larger than that recovered far from the tip. Results are given for $E_\infty/E_0 = 10^2$ and single relaxation time creep's function.

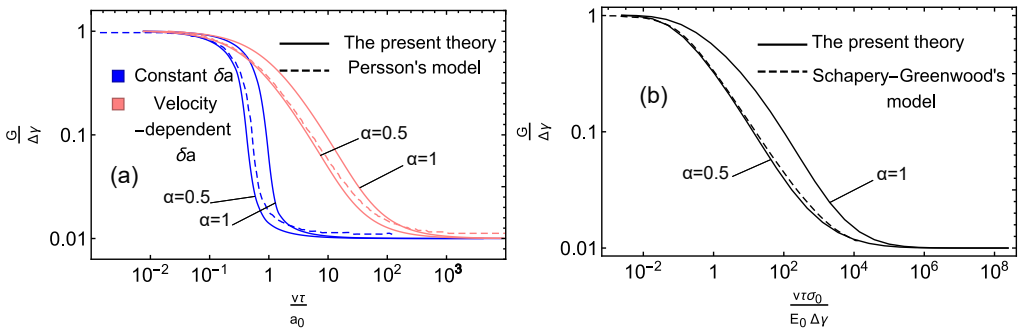

Figure 5.5: (a) Comparison between the present theory (solid lines) and the Persson's model (dashed lines, adapted from Fig. 8 in [151]) for the steady state closing crack. The normalized energy release rate $G/\Delta\gamma$ is shown as function of the dimensionless closing crack's velocity $v\tau/a_0$ in a log-log diagram, where $a_0 = 2\Delta\gamma/\left(\sqrt{2\pi}\sigma_c\right)^2$ represents the estimation of the cut-off length in the limit of slowly moving crack according to the PB theory. Pink lines refer to calculations performed assuming that the parameter δa in Eq. (5.37) is velocity-dependent as given by Eq. (5.41). Blue lines refer to calculations performed assuming velocity-independent δa given by Eq. (5.42). The reported data from [151] refer to the same assumptions with $\alpha = 1$. (b) Comparison between the present theory (solid lines) and the Greenwood's model (dashed line, adapted from Fig. 6 in [70]) for the steady state closing crack. Calculations are performed assuming that the parameter δa in Eq. (5.37) is velocity-dependent and given by Eq. (5.43), which represents the Schapery's estimation of the cohesive-zone length [68] when $\alpha = 1$. The normalized energy release rate $G/\Delta\gamma$ is shown as function of the dimensionless closing crack's velocity $v\tau\sigma_0/(E_0\Delta\gamma)$ in a log-log diagram, where σ_0 is the constant stress acting within the cohesive-zone. All results are given for $E_\infty/E_0 = 10^2$ and single relaxation time creep's function.

5.4 Unsteady crack propagation: the delayed fracture

In this section, we apply the general energy closure equation of unsteady contacts (Chapter 4) to study the unsteady propagation of a crack in a viscoelastic solid, with specific focus on the so called delayed fracture. As shown in Secs. (5.2, 5.3), the virtual work balance expressed at the tip of the crack allows to write the equilibrium equation given a certain value of the stress intensity factor K_I. In unsteady conditions, K_I is generally time-dependent and is related to the time-history of the remotely applied displacements or forces depending on the system's geometry. In this section, we consider a linear viscoelastic sheet of length L and heigth $2h$ containing a pre-existing crack, whose initial length is a_0. We assume that $a_0 > h$ and $L \gg h$, as shown in Fig. 5.6. The specimen is subjected to a generic time-dependent normal force $F(t)$ and associated time-dependent displacement $u_\infty(t)$ of the upper and lower rigid surfaces as shown in the figure. In our study, the controlled parameter is the force and the resulting time-dependent crack tip position in the considered reference frame and crack's length are $x_0(t)$ and $a(t)$. Note that, due to the specimen geometry, very far from the crack tip, for $x_1 \to +\infty$, the material is subjected to uniaxial uniform stress $\sigma_\infty(t)$ and to the corresponding uniform deformation $\varepsilon_\infty(t) = u_\infty(t)/h$, related each other through to the linear viscoelastic constitutive equation:

$$\varepsilon_\infty(t) = \int_{-\infty}^{t} dt_1 J(t-t_1)\dot{\sigma}_\infty(t_1) \tag{5.44}$$

where $J(t)$ is the viscoelastic creep's function. Let us focus on a discontinuously applied constant stress, i.e., we consider

$$\sigma_\infty(t) = \sigma_0 H(t) \tag{5.45}$$

where $H(t)$ is the unit-step function. Notably, in this pure-shear geometry [89,90], the stress intensity factor is related to the remote stress as

$$K_I(t) = \sigma_\infty(t)\sqrt{h} \tag{5.46}$$

Therefore, also the stress intensity factor undergoes the step function

$$K_I(t) = K_{I,0} H(t) \tag{5.47}$$

where $K_{I,0} = \sigma_0\sqrt{h}$. Also observe that, according to Eq. (5.44) and following the same arguments introduced in Sec. 4.9, the elastic energy density as function of time is

$$W = \frac{1}{2}\sigma_0^2 \left\{ \frac{1}{E_\infty} + \sum_{j=1}^{N} \frac{[1-\exp(-t/\tau_j)]^2}{E_j} \right\} \tag{5.48}$$

i.e., W is the total elastic energy stored in the N Voigt elements of the viscoelastic linear model. Now observe that, for $t \to 0^+$ the response of the material is purely

elastic everywhere within the solid, with the high frequency modulus E_∞. Therefore, within the very initial stage of the loading time-history, the crack equilibrium and propagation are governed by the balance between the energy release rate and the intrinsic surface energy $\Delta\gamma$ of the material. Now let us suppose that

$$G(t=0^+) = \frac{1}{2}h\frac{\sigma_0^2}{E_\infty} = \frac{K_{I,0}^2}{2E_\infty} < \Delta\gamma \tag{5.49}$$

Under these conditions, crack propagation is energetically prevented. However, crack cannot heal either, as the molecular bonds at the interface are irreversibly broken. We conclude that the crack's length remains unchanged for a certain amount of time. Now, let us observe that, after a certain time has passed: (I) the crack propagation can occur if the release of mechanical plus elastic energy is enough to compensate the change of adhesion energy plus the internally dissipated energy (see Sec. 4.9); (II) the elastic energy is a monotonically increasing function of time [see Eq. (5.48)]. Therefore, one might expect that the propagation of the crack can occur with a certain delay, once the material's creep has allowed for a sufficient amount of elastic to be stored within the solid. However, during the creep response, the crack equilibrium is no longer described by the Griffith equation due to the presence of internal dissipation. Therefore, in order to tackle the delayed fracture, we need to include the non-conservative work contribution in the equilibrium equation, i.e., we need to enforce the virtual work balance at the tip of the crack. Thus, let us focus on the asymptotic stress and displacement fields. Sufficiently close to the crack tip, the stress field presents the standard square-root singularity. Specifically the time-varying normal stress along the crack surface can be written as

$$\sigma(x_1, x_0, t) = \frac{K_I(t)}{\sqrt{2\pi\,(x_1 - x_0(t))}}\mathcal{H}[x_1 - x_0(t)]\mathcal{H}(t) \tag{5.50}$$

where $\mathcal{H}(x)$ and $\mathcal{H}(t)$ are the unit step-functions in the space and time domain, x_1 is the lateral coordinate and $x_0(t)$ is the coordinate of the crack's tip in the fixed reference frame, as shown in Fig. 5.6. Exploiting linearity, translational invariance and the elastic-viscoelastic correspondence principle (see Chapter 2), the corresponding asymptotic time-dependent surface displacement on the crack's surface is

$$u(x_1, x_0, t) = J(0)\int d\zeta\mathcal{G}(x_1-\zeta)\sigma(\zeta, x_0, t)+\int_{-\infty}^{t} dt_1\dot{J}(t-t_1)\int d\zeta\mathcal{G}(x_1-\zeta)\sigma(\zeta, x_0, t_1) \tag{5.51}$$

where $\mathcal{G}(x)$ is the Green's function of the corresponding elastic problem for a material of unitary modulus. Now observe that, in Eq. (5.51) the quantity

$$\int d\zeta\mathcal{G}(x_1 - \zeta)\sigma(\zeta, x_0, t) = u_1(x_1, x_0, t) \tag{5.52}$$

is the crack surface gap for an elastic material of unitary modulus resulting from a stress intensity factor equal to $K_I(t)$ and, using Eq. (5.50), it takes the well-known

form:

$$u_1(x_1, x_0, t) = K_I(t)\sqrt{8/\pi\,(x_0(t) - x_1)}\mathcal{H}[x_0(t) - x_1]\mathcal{H}(t) \tag{5.53}$$

allowing to re-write Eq. (5.51) as

$$u(x_1, x_0, t) = J(0)u_1(x_1, x_0, t) + \int_{-\infty}^{t} dt_1 \dot{J}(t - t_1)u_1(x_1, x_0, t_1) \tag{5.54}$$

which can be easily handled numerically. However, $x_0(t)$ must be determined by enforcing the closure equation. With this aim in mind, we recall the general expression of the virtual work principle, i.e.,

$$\delta L_I = \int_W \sigma_{ij}\delta\varepsilon_{ij}dA = \int_{\partial W} \sigma \cdot \delta\mathbf{v}dx = \delta L_E \tag{5.55}$$

for any admissible virtual displacement $\delta\mathbf{v}$ and its associated internal strain tensor $\delta\varepsilon_{ij}$, where σ is the surface stress field, and σ_{ij} is the internal stress tensor. Let us recall that in a virtual process time is 'frozen'. Thus, since the remote displacement u_∞ only depends on time according to Eq. 5.44, we conclude that $\delta\mathbf{v}$ must vanish on the upper and lower rigid interfaces of the sheet and the deformation of the contour resulting from the virtual variation of the crack tip position is the red line shown in Fig. 5.6. Thus, the work of internal stresses entirely results from the asymptotic stress field at the crack's tip and the closure equation is identical to that derived in Chapter 4 for unsteady contact mechanics. Therefore, the virtual work of internals stresses is

$$(\delta L_I)_T = \frac{1}{2}\int_a^{a+\delta a} dx_1 \sigma^+(x_1)v^-(x_1) \tag{5.56}$$

where $\sigma^+(x_1)$ and $v^-(x_1)$ are the asymptotic fields at the crack tip and the virtual work of adhesive forces is

$$(\delta L_E)_T = \delta a \Delta\gamma \tag{5.57}$$

where δa is a positive quantity that represents the infinitesimal virtual variation of the crack length and must take the same order of magnitude of the local process-zone. Now, we move back to our analysis. Observe that, for $t = 0^+$ in Eq. (5.56) we have

$$v^-(x_1) = K_I/E_\infty\sqrt{8/\pi\,(a + \delta a - x_1)} \tag{5.58}$$

$$\sigma^+(x_1) = K_I/\sqrt{2\pi\,(x_1 - a)} \tag{5.59}$$

therefore we get

$$(\delta L_I)_T\,(t = 0^+) = \frac{K_I^2}{2E_\infty}\delta a \tag{5.60}$$

i.e., the (virtual) internal work recovers the standard expression of the energy release rate, and this is consistent with the initial elastic (glassy) response. Assuming that $K_{I,0} < \sqrt{2\Delta\gamma E_\infty}$, crack propagation is prevented. Thus, we assume that the

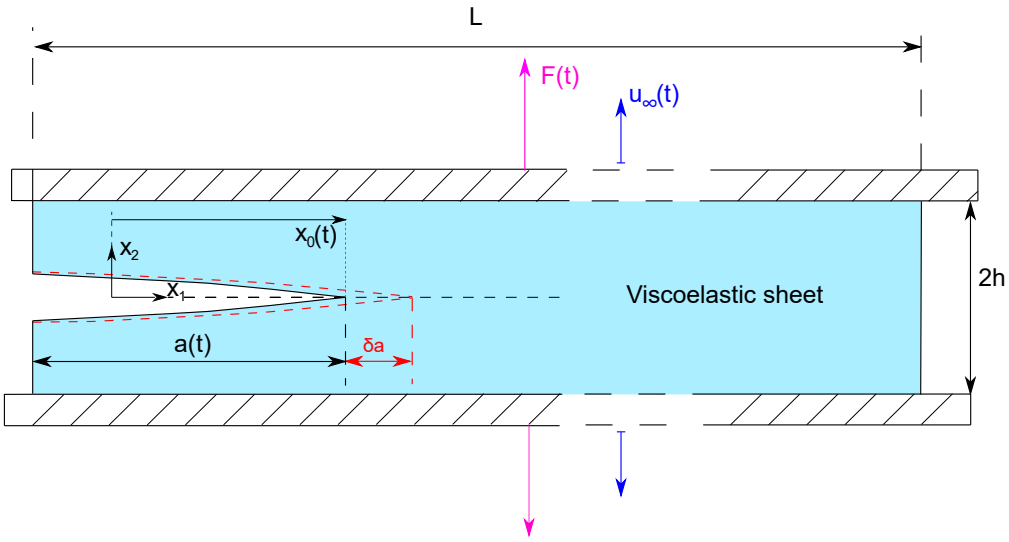

Figure 5.6: The schematic of the unsteady crack problem for a pure shear geometry. The red dashed line identifies the virtual deformation of the contour resulting from a virtual variation δa of the time-dependent crack's length a. $x_0(t)$ is the coordinate of the crack's tip in the considered fixed reference frame.

crack's tip position remains unchanged until a certain time instant t_d. Notably, for $t < t_d$, since $x_0(t) = x_0(t = 0)$ Eq. (5.54) can be expressed as

$$u(x_1, x_0, t) = u_1(x_1, x_0, t)J(t) \tag{5.61}$$

$$= J(t)K_{I,0}\sqrt{8/\pi[x_0(0) - x_1]}\mathcal{H}[x_0(0) - x_1] \tag{5.62}$$

Therefore, in Eq. (5.56) for $t < t_d$ we have

$$v^-(x_1) = J(t)K_{I,0}\sqrt{8/\pi\,(a + \delta a - x_1)} \tag{5.63}$$

$$\sigma^+(x_1) = K_I/\sqrt{2\pi\,(x_1 - a)} \tag{5.64}$$

leading to:

$$(\delta L_I)_T\,(t) = \frac{1}{2}K_{I,0}^2 J(t)\delta a \tag{5.65}$$

Since $J(t)$ is a monotonically increasing function, the condition of incipient crack propagation, i.e., $(\delta L_I)_T = (\delta L_E)_T$, is reached at time t_d corresponding to:

$$\frac{1}{2}K_{I,0}^2 J(t_d) = \Delta\gamma \tag{5.66}$$

After crack propagation starts (i.e., for $t > t_d$) the time-dependent crack tip position $x_0(t)$ must be calculated numerically. Indeed, for $t > t_d$ the displacement field must be calculated according to Eq. (5.54), i.e., considering that $x_0(t)$ is time-dependent. Therefore, Eq. (5.65) is no longer valid for $t > t_d$. The numerical resolution is based on the simple discretization of the time domain in steps Δt.

Assuming that x_0 has been determined up to time step t_k, the value $x_0(t_{k+1}) > x_0(t_k)$ is the one ensuring that the closure equation:

$$\frac{1}{2\delta a}\int_a^{a+\delta a} dx_1 \sigma^+(x_1)v^-(x_1) = \Delta\gamma \tag{5.67}$$

is satisfied at time t_{k+1}, where the stress field is given by Eq. (5.50) and the displacement field is calculated by writing Eqs. (5.53, 5.54) at time t_{k+1}. The delayed fracture behavior is summarized in Fig. 5.7. Notably, delayed fracture occurs when the applied stress intensity factor $K_{I,0}$ satisfies the following inequality:

$$\sqrt{2\Delta\gamma E_0} < K_{I,0} < \sqrt{2\Delta\gamma E_\infty} \tag{5.68}$$

Indeed, supposing $K_{I,0} > \sqrt{2\Delta\gamma E_\infty}$ crack propagates instantaneously since in such a case we have $(\delta L_I)_T(t = 0^+) > \Delta\gamma$. On the other hand, since according to Eq. (5.65) for $t < t_d$ the maximum value that $(\delta L_I)_T(t)$ can take is $1/2K_{I,0}^2/E_0$, crack will never propagate if $K_{I,0} < \sqrt{2\Delta\gamma E_0}$. In Fig. 5.7 the normalized delay-time t_d/τ is plotted as function of the dimensionless parameter $h_o\sigma_\infty^2/(2\Delta\gamma E_0)$ according to Eq.(5.66) in which we used:

$$J(t) = \left\{\frac{1}{E_\infty} + \left[\frac{1}{E_0} - \frac{1}{E_\infty}\right][1 - \exp(-t/\tau)]\right\} H(t)$$

A qualitatively similar trend of the delayed propagation time vs. the applied

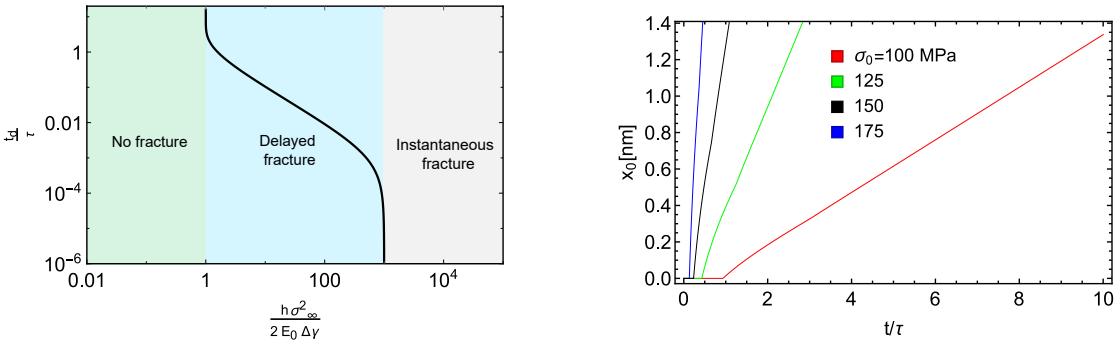

Figure 5.7: (a) The normalized delay time t_d/τ as function of the dimensionless parameter $h_o\sigma_\infty^2/(2\Delta\gamma E_0) = K_I^2/(2\Delta\gamma E_0)$ in a log-log diagram. Results refer to $E_\infty/E_0 = 10^3$. The delayed fracture is predicted as long as the inequality (5.68) is satisfied [cyan region in Figure (a)]. (b) The crack tip position x_0 as function of the dimensionless time t/τ for different values of the applied remote stress . Results are shown for $E_0 = 650$ MPa, $E_\infty = 10E_0$, $\tau = 10^{-3}$ s, $h = 6.2$ nm, $\nu = 0.5$, $\Delta\gamma = 0.03$ N/m. The critical stress in Eq. (5.69) has been estimated as $\sigma_c = \Delta\gamma/\epsilon$ where we set as range of adhesive interactions $\epsilon = 0.36$ nm.

stress has been experimentally observed [159, 162, 162]. In Fig. 5.7 (b) we report the overall trend $x_0(t)$ of the crack tip's position as function of the normalized time, for different values of the remotely applied stress. In the all of the reported cases, crack propagation occurs with a certain delay, i.e., Eq. (5.68) is satisfied.

Notably, the delay-time equation 5.66 has been derived without any assumption on the process zone length. Instead, for $t > t_d$ the quantity δa in Eq. (4.9) is set as

$$\delta a = \left(\frac{K_{I,0}}{\sqrt{2\pi}\sigma_c} \right)^2 \tag{5.69}$$

where σ_c is some characteristic stress whose order of magnitude is $\sigma_c = \Delta\gamma/\epsilon$, being ϵ the range of adhesive interactions. Eq. (5.69) represents the estimation of the process zone's length. Interestingly, Fig. (5.7) (b) shows that crack propagation starts with a certain finite speed. As expected, increasing the remote stress leads to higher crack velocity.

5.5 Conclusion

In this chapter, the crack propagation and healing in infinitely extended viscoelastic media has been studied. When steady state conditions are assumed, the displacement and stress fields present specular behaviors in the opening and closing crack cases. In the opening case, the stress distribution is the same recovered in an equivalent purely elastic problem. Instead, the displacement field is different, and presents a characteristic trumpet shape that reflects the elastic glassy response close to the crack tip and an elastic rubbery response at large distance. On the other hand, in the closing crack case, the displacement field is the same of the corresponding elastic problem and the stress distribution presents a very peculiar different trend. Specifically, very close to the crack tip, the stress intensity factor is much higher compared to the fully relaxed elastic case, reflecting a glassy response. The equivalent elastic stress intensity factor is instead recovered very far from the tip, where the material is fully relaxed. The overall energy release rate vs. crack velocity trend is predicted by enforcing the energy balance presented in Chapter 3. For both the opening and closing crack cases, results are in solid agreement with previous studies, as long as the same assumptions are made while estimating the characteristic problem's length, i.e., the size of the local process zone. Subsequently, the assumption of steady state crack motion has been relaxed, and the study has focused on the delayed fracture of viscoelastic materials. The time-dependent crack tip position has been determined by enforcing the energy closure equation for unsteady conditions provided in chapter 4. The proposed theory provides results consistent with experimental observation: depending on the magnitude of the applied stress intensity factor, crack propagation can occur either instantaneously and with a certain delay. In the latter case, a closed form relation between the applied stress and the delay-time immediately follows from the energy balance at the crack tip. The latter clearly shows that the phenomenon is related to the material's viscoelastic creep.

Conclusions

This thesis has presented a novel energy formulation to study adhesive contact and fracture mechanics of viscoelastic materials. The energy closure equation of the contact or crack problem has been rigorously formulated by exploiting the principle of virtual work: when virtual variations of the contact domain are considered, the work of the external adhesive forces is balanced by the work of internal stresses. The theoretical framework for deriving the energy equilibrium condition has been developed both in steady and general unsteady conditions. In fact, the proposed formulation is a general Griffith-like criterion for viscoelastic adhesion. Overall, the energy arguments provide deep insights on physical mechanisms responsible for experimentally observed phenomena. Indeed, the theory allows to tackle the viscoelastic-adhesive contact behavior in general conditions, and to correctly model the viscoelastic dissipation involving the entire volume of the system.
In Chapter 3, the steady-state adhesive sliding contact between a wavy surface and a viscoelastic half-plane has been investigated. Results are in solid agreement with experimental evidence, and many of the characteristic phenomena resulting from the complex interplay between adhesion and viscoelasticity have been addressed. The velocity-dependent friction coefficient is found highly increased compared to adhesiveless conditions, and the predicted trend is in solid qualitative agreement with experimental data provided by Grosch [27]. Specifically, at low velocity values the frictional response depends on visocelastic losses localized at the contact edges, where the local behavior resemble the propagation of a crack, leading to a certain amount of adhesion hysteresis. At intermediate velocity values, the effect of adhesion is even more important: the increase of contact area entails additional amount of dissipation within the bulk of the material, and the resulting friction increase cannot be explained by simply summing-up independent estimations of small- and large- scale hysteretic losses. The adhesive properties of the system have been investigated in detail as function of the contact parameters. Small-scale losses occurring at the contact trailing edge in fact increase the effective adhesion. Therefore, depending on the sliding velocity, the contact length, the pull-off force and the system's toughness are significantly higher compared to corresponding purely elastic cases.
In Chapter 4, the unsteady normal indentation of a rigid sphere into a viscoelastic half-space has been investigated. Results have elucidated the fundamental role of the specific enforced time-history on the overall response of the system. In the same chapter, a novel methodology to calculate the energy release rate and the amount of internal dissipation has been presented. This has allowed to investigate

the physical mechanisms responsible for the predicted phenomena. Importantly, results clearly indicate that models based on scale-separation exploiting the JKR equations with energy of adhesion replaced by a velocity dependent term might do not properly tackle the real behavior of the system. During approach - retraction cycles with vanishing dwell-time, significative hysteresis is observed and the pull-off force vs. the retraction velocity curve exhibits a bell-shape that reflects the viscoelastic-induced adhesion enhancement. This mostly depends on local dissipation, leading to increased energy release rate. However, a very different behavior is observed when the dwell-time allows for the full relaxation of the material. In this case, the pull-off force monotonically increases with the retraction speed, until a plateau is reached. In the high velocity limit, a flat-punch like behavior is triggered by the glassy response of the material, that prevents the contact area form decreasing. Under this conditions, since the response of the material is elastic, the energy release rate equates the thermodynamical value of the adhesion energy. In this case, the relations between contact quantities deviate from the JKR predictions, therefore, the JKR model cannot predict the contact behavior.
In Chapter 5, the steady and unsteady crack propagation and healing in viscoelastic media has been investigated. When steady state conditions are assumed, the proposed theory correctly predicts the dependence of the energy release rate from the crack's speed, in perfect agreement with previous studies, as long as the same assumptions are made in estimating the process zone's length. Under unsteady conditions, the energy formulation allows to predict a fundamental experimentally observed phenomenon: the so called-delayed fracture. Specifically, when subjected to a discontinuously applied stress, the fracture of a viscoelastic solid might occur with a certain delay-time, which is found to depend on the viscoelastic creep of the material.
Overall, the results presented in this thesis are in agreement with experimental observations and are supported by previous theoretical or numerical studies. Hence, this dissertation aims at providing a general effective, simple and versatile method to predict, investigate and deeply understand the adhesive contact behavior of viscoelastic materials.

References

References

[1] Khashaba, U. A., Othman, R., Najjar, I. M. (2020). Development and characterization of structural adhesives for aerospace industry with alumina nanoparticles under shear and thermo-mechanical impact loads. Proceedings of the Institution of Mechanical Engineers, Part G: Journal of Aerospace Engineering, 234(2), 490-507.

[2] Vilhena, L., Ramalho, A. (2016). Friction of human skin against different fabrics for medical use. Lubricants, 4(1), 6.

[3] Van den Dobbelsteen, J. J., Schooleman, A., Dankelman, J. (2007). Friction dynamics of trocars. Surgical endoscopy, 21, 1338-1343.

[4] Shah, N. V., & Meislin, R. (2013). Current state and use of biological adhesives in orthopedic surgery. Orthopedics, 36(12), 945-956.

[5] Zaokari, Y., Persaud, A., & Ibrahim, A. (2020). Biomaterials for adhesion in orthopedic applications: a review. Engineered Regeneration, 1, 51-63.

[6] Sancaktar, E., & Brinson, H. F. (1980). The viscoelastic shear behavior of a structural adhesive. In Adhesion and Adsorption of Polymers (pp. 279-299). Boston, MA: Springer US.

[7] Bitner, J. L., Rushford, J. L., Rose, W. S., Hunston, D. L., & Riew, C. K. (1981). Viscoelastic fracture of structural adhesives. The Journal of Adhesion, 13(1), 3-28.

[8] Chung, J. Y., Chaudhury, M. K. (2005). Roles of discontinuities in bio-inspired adhesive pads. Journal of the Royal Society Interface, 2(2), 55-61.

[9] Zhou, M., Pesika, N., Zeng, H., Tian, Y., Israelachvili, J. (2013). Recent advances in gecko adhesion and friction mechanisms and development of gecko-inspired dry adhesive surfaces. Friction, 1, 114-129.

[10] Tang, W., Ge, S. R., Zhu, H., Cao, X. C., Li, N. (2008). The influence of normal load and sliding speed on frictional properties of skin. Journal of bionic engineering, 5(1), 33-38.

[11] Menga, N., Afferrante, L., Pugno, N. M., Carbone, G. (2018). The multiple V-shaped double peeling of elastic thin films from elastic soft substrates. Journal of the Mechanics and Physics of Solids, 113, 56-64.

[12] Menga, N., Dini, D., Carbone, G. (2020). Tuning the periodic V-peeling behavior of elastic tapes applied to thin compliant substrates. International Journal of Mechanical Sciences, 170, 105331.

[13] Ceglie, M., Menga, N., Carbone, G. (2022). The role of interfacial friction on the peeling of thin viscoelastic tapes. Journal of the Mechanics and Physics of Solids, 159, 104706.

[14] Ayyildiz, M., Scaraggi, M., Sirin, O., Basdogan, C., Persson, B. N. (2018). Contact mechanics between the human finger and a touchscreen under electroadhesion. Proceedings of the National Academy of Sciences, 115(50), 12668-12673.

[15] Sharp, R. S., Gruber, P., Fina, E. (2016). Circuit racing, track texture, temperature and rubber friction. Vehicle System Dynamics, 54(4), 510-525.

[16] Bhushan, B. (2007). Nanotribology and nanomechanics of MEMS/NEMS and BioMEMS/BioNEMS materials and devices. Microelectronic Engineering, 84(3), 387-412.

[17] Kim, S. H., Asay, D. B., Dugger, M. T. (2007). Nanotribology and MEMS. Nano today, 2(5), 22-29.

[18] Zeng, X., Peng, Y., Yu, M., Lang, H., Cao, X. A., Zou, K. (2018). Dynamic sliding enhancement on the friction and adhesion of graphene, graphene oxide, and fluorinated graphene. ACS applied materials interfaces, 10(9), 8214-8224.

[19] Ding, J. N., Meng, Y. G., & Wen, S. Z. (2000). Mechanical Stability and Sticking in a Model Microelectromechanical Systems (MEMS) under Casimir Forces–Part I: Corrections to the Casimir Force. International Journal of Nonlinear Sciences and Numerical Simulation, 1(Supplement), 373-378.

[20] Taran, B., Amoozegar, S., Bayaz, R. N. D., & Barazandeh, F. (2011, May). The theoretical investigation of the effect of adhesive layers used in microassembly on the dynamic response of a microaccelerometer. In 2011 Symposium on Design, Test, Integration & Packaging of MEMS/MOEMS (DTIP) (pp. 1-6). IEEE.

[21] Ali, U. E., Yang, H., Khayrudinov, V., Modi, G., Cheng, Z., Agarwal, R., Bhaskaran, H. (2022). A Universal Pick-and-Place Assembly for Nanowires. Small, 18(38), 2201968.

[22] Quini, J. G., Marinucci, G. (2012). Polyurethane structural adhesives applied in automotive composite joints. Materials research, 15, 434-439.

[23] Zhang, Y., Chen, B. K., Liu, X., Sun, Y. (2009). Autonomous robotic pick-and-place of microobjects. IEEE transactions on robotics, 26(1), 200-207.

[24] Mengüç, Y., Yang, S. Y., Kim, S., Rogers, J. A., Sitti, M. (2012). Gecko-inspired controllable adhesive structures applied to micromanipulation. Advanced Functional Materials, 22(6), 1246-1254.

[25] Persson, B. N. (2001). Theory of rubber friction and contact mechanics. The Journal of Chemical Physics, 115(8), 3840-3861.

[26] Carbone, G., Putignano, C. (2014). Rough viscoelastic sliding contact: theory and experiments. Physical Review E, 89(3), 032408.

[27] Grosch, K. A. (1963). The relation between the friction and visco-elastic properties of rubber. Proceedings of the Royal Society of London. Series A. Mathematical and Physical Sciences, 274(1356), 21-39.

[28] Barquins, M., Maugis, D., Blouet, J., Courtel, R. (1978). Contact area of a ball rolling on an adhesive viscoelastic material. Wear, 51(2), 375-384.

[29] Hoyer, B. K., Long, R., Rentschler, M. E. (2022). A tribometric device for the rolling contact of soft elastomers. Tribology Letters, 70(2), 39.

[30] Carbone, G., Putignano, C. (2013). A novel methodology to predict sliding and rolling friction of viscoelastic materials: Theory and experiments. Journal of the Mechanics and Physics of Solids, 61(8), 1822-1834.

[31] Hunter, S. C. (1961). The rolling contact of a rigid cylinder with a viscoelastic half space.

[32] Charmet, J. C., Barquins, M. (1996). Adhesive contact and rolling of a rigid cylinder under the pull of gravity on the underside of a smooth-surfaced sheet of rubber. International journal of adhesion and adhesives, 16(4), 249-254.

[33] Giri, M., Bousfield, D. B., & Unertl, W. N. (2001). Dynamic contacts on viscoelastic films: work of adhesion. Langmuir, 17(10), 2973-2981.

[34] Li, M., Jiao, Q., Dai, Q., Shi, L., Huang, W., & Wang, X. (2019). Effects of bulk viscoelasticity and surface wetting on the contact and adhesive properties of a soft material. Polymer Testing, 74, 266-273.

[35] Linghu, C., Yang, X., Liu, Y., Li, D., Gao, H., & Hsia, K. J. (2023). Mechanics of shape-locking-governed R2G adhesion with shape memory polymers. Journal of the Mechanics and Physics of Solids, 170, 105091.

[36] Ahn, D., & Shull, K. R. (1996). JKR studies of acrylic elastomer adhesion to glassy polymer substrates. Macromolecules, 29(12), 4381-4390.

[37] Carbone, G., Mangialardi, L. (2004). Adhesion and friction of an elastic half-space in contact with a slightly wavy rigid surface. Journal of the Mechanics and Physics of Solids, 52(6), 1267-1287.

[38] Johnson, K. L., Kendall, K., Roberts, A. (1971). Surface energy and the contact of elastic solids. Proceedings of the royal society of London. A. mathematical and physical sciences, 324(1558), 301-313.

[39] Guduru, P. R. (2007). Detachment of a rigid solid from an elastic wavy surface: theory. Journal of the Mechanics and Physics of Solids, 55(3), 445-472.

[40] Greenwood, J. A., & Williamson, J. B. P., 1966. Contact of Nominally Flat Surfaces. Proceedings of the Royal Society A: Mathematical, Physical and Engineering Sciences, 295(1442), 300–319.

[41] Carbone, G., Scaraggi, M., & Tartaglino, U. (2009). Adhesive contact of rough surfaces: comparison between numerical calculations and analytical theories. The European Physical Journal E, 30, 65-74.

[42] Carbone, G., Mangialardi, L., & Persson, B. N. J. (2004). Adhesion between a thin elastic plate and a hard randomly rough substrate. Physical Review B, 70(12), 125407.

[43] Menga, N., Afferrante, L., Demelio, G. P., Carbone, G. (2018). Rough contact of sliding viscoelastic layers: numerical calculations and theoretical predictions. Tribology International, 122, 67-75.

[44] Menga, N., Carbone, G., & Dini, D. (2019). Corrigendum to "Do uniform tangential interfacial stresses enhance adhesion?"[Journal of the Mechanics and Physics of Solids 112 (2018) 145–156].

[45] Menga, N., Putignano, C., Afferrante, L., & Carbone, G. (2019). The contact mechanics of coated elastic solids: Effect of coating thickness and stiffness. Tribology Letters, 67, 1-10.

[46] Stan, G., & Adams, G. G. (2016). Adhesive contact between a rigid spherical indenter and an elastic multi-layer coated substrate. International journal of solids and structures, 87, 1-10.

[47] Carbone, G., & Mangialardi, L. (2008). Analysis of the adhesive contact of confined layers by using a Green's function approach. Journal of the Mechanics and Physics of Solids, 56(2), 684-706.

[48] Menga, N., Afferrante, L., Carbone, G. (2016). Adhesive and adhesiveless contact mechanics of elastic layers on slightly wavy rigid substrates. International Journal of Solids and Structures, 88, 101-109.

[49] Lin, Y. Y., Chang, C. F., & Lee, W. T. (2008). Effects of thickness on the largely-deformed JKR (Johnson–Kendall–Roberts) test of soft elastic layers. International Journal of Solids and Structures, 45(7-8), 2220-2232.

[50] Carbone, G., Pierro, E., & Gorb, S. N. (2011). Origin of the superior adhesive performance of mushroom-shaped microstructured surfaces. Soft Matter, 7(12), 5545-5552.

[51] Tabor, D. (1977). Surface forces and surface interactions. In Plenary and Invited Lectures (pp. 3-14). Academic Press.

[52] Muller, V. M., Yushchenko, V. S., Derjaguin, B. V. (1980). On the in fluence of molecular forces on the deformation of an elastic sphere and its sticking to a rigid plane. Journal of Colloid and Interface Science, 77(1), 91-101.

[53] Maugis, D. (1992). Adhesion of spheres: the JKR-DMT transition using a Dugdale model. Journal of colloid and interface science, 150(1), 243-269.

[54] Greenwood, J. A. (1997). Adhesion of elastic spheres. Proceedings of the Royal Society of London. Series A: Mathematical, Physical and Engineering Sciences, 453(1961), 1277-1297.

[55] Gruhn, T., Franke, T., Dimova, R., & Lipowsky, R. (2007). Novel method for measuring the adhesion energy of vesicles. Langmuir, 23(10), 5423-5429.

[56] Das, S., Lahiri, D., Lee, D. Y., Agarwal, A., & Choi, W. (2013). Measurements of the adhesion energy of graphene to metallic substrates. Carbon, 59, 121-129.

[57] Raegen, A. N., Dalnoki-Veress, K., Wan, K. T., & Jones, R. A. L. (2006). Measurement of adhesion energies and Young's modulus in thin polymer films using a novel axi-symmetric peel test geometry. The European Physical Journal E, 19, 453-459.

[58] Shull, K. R. (2002). Contact mechanics and the adhesion of soft solids. Materials Science and Engineering: R: Reports, 36(1), 1-45.

[59] Hui, C. Y., Liu, T., Salez, T., Raphael, E., & Jagota, A. (2015). Indentation of a rigid sphere into an elastic substrate with surface tension and adhesion. Proceedings of the Royal Society A: Mathematical, Physical and Engineering Sciences, 471(2175), 20140727.

[60] She, H., Malotky, D., Chaudhury, M. K. (1998). Estimation of adhesion hysteresis at polymer/oxide interfaces using rolling contact mechanics. Langmuir, 14(11), 3090-3100.

[61] Krijt, S., Dominik, C., Tielens, A. G. G. M. (2014). Rolling friction of adhesive microspheres. Journal of Physics D: Applied Physics, 47(17), 175302.

[62] Zhang, Y., Wang, X., Li, H., Yang, W. (2015). A numerical study of the rolling friction between a microsphere and a substrate considering the adhesive effect. Journal of Physics D: Applied Physics, 49(2), 025501.

[63] Greenwood, J. A., & Johnson, K. L. (2006). Oscillatory loading of a viscoelastic adhesive contact. Journal of colloid and interface science, 296(1), 284-291.

[64] Johnson, K. L. (2000). Contact mechanics and adhesion of viscoelastic spheres.

[65] Afferrante, L., & Violano, G. (2022). On the effective surface energy in viscoelastic Hertzian contacts. Journal of the Mechanics and Physics of Solids, 158, 104669.

[66] Violano, G., Afferrante, L. (2022). Size effects in adhesive contacts of viscoelastic media. European Journal of Mechanics-A/Solids, 96, 104665.

[67] Lorenz, B., Krick, B. A., Mulakaluri, N., Smolyakova, M., Dieluweit, S., Sawyer, W. G., & Persson, B. N. J. (2013). Adhesion: role of bulk viscoelasticity and surface roughness. Journal of Physics: Condensed Matter, 25(22), 225004.

[68] Schapery, R. A. (1989). On the mechanics of crack closing and bonding in linear viscoelastic media. International Journal of Fracture, 39, 163-189.

[69] Persson, B. N. J., Brener, E. A. (2005). Crack propagation in viscoelastic solids. Physical Review E, 71(3), 036123.

[70] Greenwood, J. A. (2004). The theory of viscoelastic crack propagation and healing. Journal of Physics D: Applied Physics, 37(18), 2557.

[71] Barber, M., Donley, J., & Langer, J. S. (1989). Steady-state propagation of a crack in a viscoelastic strip. Physical Review A, 40(1), 366.

[72] Carbone, G., Persson, B. N. J. (2005). Hot cracks in rubber: origin of the giant toughness of rubberlike materials. Physical review letters, 95(11), 114301.

[73] Müser, M. H., Sukhomlinov, S. V., & Pastewka, L. (2023). Interatomic potentials: Achievements and challenges. Advances in Physics: X, 8(1), 2093129.

[74] Luo, J., Liu, J., Xia, H., Ao, X., Fu, Z., Ni, J., & Huang, H. (2024). Finite Element Analysis of Adhesive Contact Behaviors in Elastoplastic and Viscoelastic Media. Tribology Letters, 72(1), 7.

[75] Afferrante, L., Violano, G., & Carbone, G. (2023). Exploring the dynamics of viscoelastic adhesion in rough line contacts. Scientific Reports, 13(1), 15060.

[76] Maghami, A., Wang, Q., Tricarico, M., Ciavarella, M., Li, Q., Papangelo, A. (2024). Bulk and fracture process zone contribution to the rate-dependent adhesion amplification in viscoelastic broad-band materials. Journal of the Mechanics and Physics of Solids, 193, 105844.

[77] Papangelo, A., Nazari, R., Ciavarella, M. (2024). Friction for a sliding adhesive viscoelastic cylinder: Effect of Maugis parameter. European Journal of Mechanics-A/Solids, 107, 105348.

[78] Müser, M. H., & Persson, B. N. (2022). Crack and pull-off dynamics of adhesive, viscoelastic solids. Europhysics Letters, 137(3), 36004.

[79] Persson, B. N., & Scaraggi, M. (2014). Theory of adhesion: Role of surface roughness. The Journal of chemical physics, 141(12).

[80] Lin, Y. Y., & Hui, C. Y. (2002). Mechanics of contact and adhesion between viscoelastic spheres: an analysis of hysteresis during loading and unloading. Journal of Polymer Science Part B: Polymer Physics, 40(9), 772-793.

[81] Haiat, G., Huy, M. P., & Barthel, E. (2003). The adhesive contact of viscoelastic spheres. Journal of the Mechanics and Physics of Solids, 51(1), 69-99.

[82] Haiat, G., & Barthel, E. (2007). An approximate model for the adhesive contact of rough viscoelastic surfaces. Langmuir, 23(23), 11643-11650.

[83] Pérez-Ràfols, F., Van Dokkum, J. S., & Nicola, L. (2023). On the interplay between roughness and viscoelasticity in adhesive hysteresis. Journal of the Mechanics and Physics of Solids, 170, 105079.

[84] Schapery, R. A. (1975). A theory of crack initiation and growth in viscoelastic media: I. Theoretical development. International Journal of fracture, 11, 141-159.

[85] Persson, B. N. J. (2021). On opening crack propagation in viscoelastic solids. Tribology Letters, 69(3), 115.

[86] Greenwood, J. A. (2007). Viscoelastic crack propagation and closing with Lennard-Jones surface forces. Journal of Physics D: Applied Physics, 40(6), 1769.

[87] Inglis, C.E., "Stresses in Plates Due to the Presence of Cracks and Sharp Corners," Transactions of the Institute of Naval Architects, Vol. 55, pp. 219-241, 1913.

[88] Griffith, A. A. (1921). VI. The phenomena of rupture and flow in solids. Philosophical transactions of the royal society of london. Series A, containing papers of a mathematical or physical character, 221(582-593), 163-198.

[89] D'Amico, F., Carbone, G., Foglia, M. M., & Galietti, U. (2013). Moving cracks in viscoelastic materials: Temperature and energy-release-rate measurements. Engineering Fracture Mechanics, 98, 315-325.

[90] Maugis, D. (2000). Contact, adhesion and rupture of elastic solids (Vol. 130). Springer Science & Business Media.

[91] Irwin, G.R., Analysis of stresses and strains near the end of a crack traversing a plate. Journal of Applied Mechanics, 24, 1957, 361–364.

[92] J.R. Rice, A path independent integral and the approximate analysis of strain concentration by notches and cracks. J. Appl. Mech. 35, 379-386 (1968).

[93] Guenault, T. (1986). Thermodynamics and an introduction to Thermostatistics, -Callen, HB.

[94] Boussinesq J., Applications des potentiels a l'étude de l'équilibre et du mouvement des solides élastiques, Gauthier-Villars, Paris (1885)

[95] Hertz H. 1882, J. Reine Angew. Math. 92, 156

[96] Bradley, R. S. (1932). LXXIX. The cohesive force between solid surfaces and the surface energy of solids. The London, Edinburgh, and Dublin Philosophical Magazine and Journal of Science, 13(86), 853-862.

[97] Derjaguin, B. (1934). Untersuchungen ueber die reibung und adhaesion, IV: Theorie des anhaftens kleiner teilchen. Kolloid-Zeitschrift, 69, 155-164.

[98] Deraguin, B. V., Muller, V. M., Toporov, Y. P. (1975). Surface energy and the contact of elastic solids. J. Colloid. Interface Sci, 67, 314-326.

[99] Muller, V. M., Derjaguin, B. V., Toporov, Y. P. (1983). On two methods of calculation of the force of sticking of an elastic sphere to a rigid plane. Colloids and Surfaces, 7(3), 251-259.

[100] d'Alembert, J. L. R. (1743). Traité de dynamique. David l'aîné.

[101] Lagrange, J. L. (1853). Mécanique analytique (Vol. 1). Mallet-Bachelier.

[102] Carbone, G., Lorenz, B., Persson, B. N., Wohlers, A. (2009). Contact mechanics and rubber friction for randomly rough surfaces with anisotropic statistical properties. The European Physical Journal E, 29, 275-284.

[103] Menga, N., Afferrante, L., Carbone, G. (2016). Effect of thickness and boundary conditions on the behavior of viscoelastic layers in sliding contact with wavy profiles. Journal of the Mechanics and Physics of Solids, 95, 517-529.

[104] Christensen, R. M. (2013). Theory of viscoelasticity. Courier Corporation.

[105] Harrass, M., Friedrich, K., Almajid, A. A. (2010). Tribological behavior of selected engineering polymers under rolling contact. Tribology International, 43(3), 635-646.

[106] Persson, B. N. J. (2010). Rolling friction for hard cylinder and sphere on viscoelastic solid. The European Physical Journal E, 33, 327-333.

[107] Menga, N., Putignano, C., Carbone, G., Demelio, G. P. (2014). The sliding contact of a rigid wavy surface with a viscoelastic half-space. Proceedings of the Royal Society A: Mathematical, Physical and Engineering Sciences, 470(2169), 20140392.

[108] Putignano, C., Menga, N., Afferrante, L., Carbone, G. (2019). Viscoelasticity induces anisotropy in contacts of rough solids. Journal of the Mechanics and Physics of Solids, 129, 147-159.

[109] Afferrante, L., Putignano, C., Menga, N., Carbone, G. (2019). Friction in rough contacts of linear viscoelastic surfaces with anisotropic statistical properties. The European Physical Journal E, 42, 1-8.

[110] Fuller, K. N. G., Roberts, A. D. (1981). Rubber rolling on rough surfaces. Journal of Physics D: Applied Physics, 14(2), 221.

[111] Kendall, K. (1975). Rolling friction and adhesion between smooth solids. Wear, 33(2), 351-358.

[112] Carbone, G., Persson, B. N. J. (2005). Crack motion in viscoelastic solids: the role of the flash temperature. The European Physical Journal E, 17, 261-281.

[113] Baney, J. M., Hui, C. Y. (1999). Viscoelastic crack healing and adhesion. Journal of applied physics, 86(8), 4232-4241.

[114] Persson, B. N. (1998). On the theory of rubber friction. Surface science, 401(3), 445-454.

[115] Scaraggi, M., Persson, B. N. J. (2015). Friction and universal contact area law for randomly rough viscoelastic contacts. Journal of Physics: Condensed Matter, 27(10), 105102.

[116] Roberts, A. D. (1979). Looking at rubber adhesion. Rubber Chemistry and Technology, 52(1), 23-42.

[117] Tiwari, A., Dorogin, L., Tahir, M., Stöckelhuber, K. W., Heinrich, G., Espallargas, N., Persson, B. N. (2017). Rubber contact mechanics: adhesion, friction and leakage of seals. Soft Matter, 13(48), 9103-9121.

[118] Gawliński, M. (2007). Friction and wear of elastomer seals. Archives of civil and mechanical engineering, 7(4), 57-67.

[119] Shui, L., Jia, L., Li, H., Guo, J., Guo, Z., Liu, Y., ... Chen, X. (2020). Rapid and continuous regulating adhesion strength by mechanical micro-vibration. Nature communications, 11(1), 1583.

[120] Persson, B.N.J., 2000. Sliding Friction: Physical Principles and Applications, 2nd Edition. Springer, Berlin.

[121] Yoshizawa, H., Israelachvili, J. (1993). Fundamental mechanisms of interfacial friction. 2. Stick-slip friction of spherical and chain molecules. The Journal of Physical Chemistry, 97(43), 11300-11313.

[122] Yoshizawa, H., Chen, Y. L., Israelachvili, J. (1993). Fundamental mechanisms of interfacial friction. 1. Relation between adhesion and friction. The Journal of Physical Chemistry, 97(16), 4128-4140.

[123] Maeda, N., Chen, N., Tirrell, M., Israelachvili, J. N. (2002). Adhesion and friction mechanisms of polymer-on-polymer surfaces. Science, 297(5580), 379-382.

[124] Chaudhury, M. K. (1996). Interfacial interaction between low-energy surfaces. Materials Science and Engineering: R: Reports, 16(3), 97-159.

[125] Chernyak, Y. B., Leonov, A. I. (1986). On the theory of the adhesive friction of elastomers. Wear, 108(2), 105-138.

[126] McBride, A. (1999). Special functions, by George E. Andrews, Richard Askey and Ranjan Roy. Pp. 664.£ 60. 1999. ISBN 0 521 62321 9 (Cambridge University Press.). The Mathematical Gazette, 83(497), 355-357.

[127] Maximon, L. C. (2003). The dilogarithm function for complex argument. Proceedings of the Royal Society of London. Series A: Mathematical, Physical and Engineering Sciences, 459(2039), 2807-2819.

[128] Putignano, C., & Carbone, G. (2022). Indenting viscoelastic thin layers: A numerical assessment. Mechanics Research Communications, 126, 104011.

[129] de Gennes, P. G. (1996). Soft adhesives. Langmuir, 12(19), 4497-4500.

[130] Persson, B. N. J. (2017). Crack propagation in finite-sized viscoelastic solids with application to adhesion. Europhysics Letters, 119(1), 18002.

[131] Menga, N., Carbone, G., Dini, D. (2021). Exploring the effect of geometric coupling on friction and energy dissipation in rough contacts of elastic and viscoelastic coatings. Journal of the Mechanics and Physics of Solids, 148, 104273

[132] Persson, B. N. J. (2024). Influence of temperature and crack-tip speed on crack propagation in elastic solids. arXiv preprint arXiv:2409.06182.

[133] Slootman, J., Waltz, V., Yeh, C. J., Baumann, C., Göstl, R., Comtet, J., Creton, C. (2020). Quantifying rate-and temperature-dependent molecular damage in elastomer fracture. Physical Review X, 10(4), 041045.

[134] Charrault, E., Gauthier, C., Marie, P., & Schirrer, R. (2009). Experimental and theoretical analysis of a dynamic JKR contact. Langmuir, 25(10), 5847-5854.

[135] Jiang, L., Wu, M., Yu, Q., Shan, Y., & Zhang, Y. (2021). Investigations on the adhesive contact behaviors between a viscoelastic stamp and a transferred element in microtransfer printing. Coatings, 11(10), 1201.

[136] Das, D., & Chasiotis, I. (2021). Rate dependent adhesion of nanoscale polymer contacts. Journal of the Mechanics and Physics of Solids, 156, 104597.

[137] Davis, C. S., Lemoine, F., Darnige, T., Martina, D., Creton, C., & Lindner, A. (2014). Debonding mechanisms of soft materials at short contact times. Langmuir, 30(35), 10626-10636

[138] Luengo, G., Pan, J., Heuberger, M., & Israelachvili, J. N. (1998). Temperature and time effects on the "adhesion dynamics" of poly (butyl methacrylate)(PBMA) surfaces. Langmuir, 14(14), 3873-3881.

[139] Baek, D., Hemthavy, P., Saito, S., & Takahashi, K. (2017). Evaluation of energy dissipation involving adhesion hysteresis in spherical contact between a glass lens and a PDMS block. Applied Adhesion Science, 5, 1-11.

[140] Wahl, K. J., Asif, S. A. S., Greenwood, J. A., & Johnson, K. L. (2006). Oscillating adhesive contacts between micron-scale tips and compliant polymers. Journal of colloid and interface science, 296(1), 178-188.

[141] Ebenstein, D. M., & Wahl, K. J. (2006). A comparison of JKR-based methods to analyze quasi-static and dynamic indentation force curves. Journal of colloid and interface science, 298(2), 652-662.

[142] Lin, Y. Y., & Hui, C. Y. (2002). Mechanics of contact and adhesion between viscoelastic spheres: an analysis of hysteresis during loading and unloading. Journal of Polymer Science Part B: Polymer Physics, 40(9), 772-793.

[143] Chopin, J., Villey, R., Yarusso, D., Barthel, E., Creton, C., & Ciccotti, M. (2018). Nonlinear viscoelastic modeling of adhesive failure for polyacrylate pressure-sensitive adhesives. Macromolecules, 51(21), 8605-8610.

[144] Creton, C., Hooker, J., & Shull, K. R. (2001). Bulk and interfacial contributions to the debonding mechanisms of soft adhesives: Extension to large strains. Langmuir, 17(16), 4948-4954.

[145] Johnson, K. L., & Johnson, K. L. (1987). Contact mechanics. Cambridge university press.

[146] Lubarda, V. A. (2013). Circular loads on the surface of a half-space: displacement and stress discontinuities under the load. International Journal of Solids and Structures, 50(1), 1-14.

[147] Menga, N., & Carbone, G. (2019). The surface displacements of an elastic half-space subjected to uniform tangential tractions applied on a circular area. European Journal of Mechanics-A/Solids, 73, 137-143.

[148] Violano, G., & Afferrante, L. (2019). Adhesion of compliant spheres: An experimental investigation. Procedia Structural Integrity, 24, 251-258.

[149] Kendall, K. (1971). The adhesion and surface energy of elastic solids. Journal of Physics D: Applied Physics, 4(8), 1186.

[150] Akulichev, A. G., Tiwari, A., Dorogin, L., Echtermeyer, A. T., & Persson, B. N. J. (2018). Rubber adhesion below the glass transition temperature: Role of frozen-in elastic deformation. Europhysics Letters, 120(3), 36002.

[151] Persson, B. N. J. (2021). A simple model for viscoelastic crack propagation. The European Physical Journal E, 44, 1-10.

[152] Pérez-Ràfols, F., Van Dokkum, J. S., Nicola, L. (2023). On the interplay between roughness and viscoelasticity in adhesive hysteresis. Journal of the Mechanics and Physics of Solids, 170, 105079.

[153] Knauss, W. G. (1973). On the steady propagation of a crack in a viscoelastic sheet: Experiments and analysis. In Deformation and fracture of high polymers (pp. 501-541). Boston, MA: Springer US.

[154] Knauss, W. G. (2015). A review of fracture in viscoelastic materials. International Journal of Fracture, 196, 99-146.

[155] Greenwood, J. A. (2004). The theory of viscoelastic crack propagation and healing. Journal of Physics D: Applied Physics, 37(18), 2557.

[156] de Gennes, P. G. (1996). Soft adhesives. Langmuir, 12(19), 4497-4500.

[157] Persson, B. N. J., & Brener, E. A. (2005). Crack propagation in viscoelastic solids. Physical Review E—Statistical, Nonlinear, and Soft Matter Physics, 71(3), 036123.

[158] Persson, B. N. J. (2021). A simple model for viscoelastic crack propagation. The European Physical Journal E, 44, 1-10.

[159] Skrzeszewska, P. J., Sprakel, J., de Wolf, F. A., Fokkink, R., Cohen Stuart, M. A., & van der Gucht, J. (2010). Fracture and self-healing in a well-defined self-assembled polymer network. Macromolecules, 43(7), 3542-3548.

[160] Bonn, D., Kellay, H., Prochnow, M., Ben-Djemiaa, K., & Meunier, J. (1998). Delayed fracture of an inhomogeneous soft solid. Science, 280(5361), 265-267.

[161] Ravi-Chandar, K., & Knauss, W. G. (1984). An experimental investigation into dynamic fracture: I. Crack initiation and arrest. International Journal of Fracture, 25, 247-262.

[162] Sprakel, J., Lindström, S. B., Kodger, T. E., & Weitz, D. A. (2011). Stress enhancement in the delayed yielding of colloidal gels. Physical review letters, 106(24), 248303.

[163] Lindström, S. B., Kodger, T. E., Sprakel, J., & Weitz, D. A. (2012). Structures, stresses, and fluctuations in the delayed failure of colloidal gels. Soft Matter, 8(13), 3657-3664.

[164] Hui, C. Y., Zhu, B., Long, R. (2022). Steady state crack growth in viscoelastic solids: A comparative study. Journal of the Mechanics and Physics of Solids, 159, 104748.

Publications

Some contents of this thesis have been published in the following research articles, of which I am a co-author. Specifically, the first two items of the following list contain the general energy formulation and part of the results concerning steady-state sliding contact mechanics presented in Chapter 3. The third item contains the generalization of the energy formulation to unsteady conditions and part of the results presented in Chapter 4.

Journal papers:

- Carbone, G., Mandriota, C., & Menga, N. (2022). Theory of viscoelastic adhesion and friction. Extreme Mechanics Letters, 56, 101877. https://doi.org/10.1016/j.eml.2022.101877
- Mandriota, C., Menga, N., & Carbone, G. (2024). Adhesive contact mechanics of viscoelastic materials. International Journal of Solids and Structures, 290, 112685. https://doi.org/10.1016/j.ijsolstr.2024.112685
- Mandriota, C., Menga, N., & Carbone, G. (2024). Enhancement of adhesion strength in viscoelastic unsteady contacts. Journal of the Mechanics and Physics of Solids, 192, 105826. https://doi.org/10.1016/j.jmps.2024.105826

Conference papers:

- Mandriota, C., Carbone, G., & Menga, N. (2024, May). Modelling Viscoelastic Adhesion and Friction in Sliding Contact Mechanics. In International Tribology Symposium of IFToMM (pp. 406-415). Cham: Springer Nature Switzerland